Investigation of 1.55 µm GaInNAsSb/GaNAs Semiconductor Quantum Well Laser Structures

James Ferguson

PhD Thesis

School of Physics and Astronomy

Cardiff University

NOTICE OF SUBMISSION OF THESIS FORM:
POSTGRADUATE RESEARCH

CARDIFF
UNIVERSITY
PRIFYSGOL
CAERDYDD

DECLARATION

This work has not previously been accepted in substance for any degree and is not concurrently submitted in candidature for any degree.

Signed .... (candidate) Date 10/06/10

STATEMENT 1

This thesis is being submitted in partial fulfillment of the requirements for the degree of PhD .... (insert MCh, MD, MPhil, PhD etc, as appropriate)

Signed .... (candidate) Date 10/06/10

STATEMENT 2

This thesis is the result of my own independent work/investigation, except where otherwise stated.
Other sources are acknowledged by explicit references.

Signed .... (candidate) Date 10/06/10

STATEMENT 3

I hereby give consent for my thesis, if accepted, to be available for photocopying and for inter-library loan, and for the title and summary to be made available to outside organisations.

Signed .... (candidate) Date 10/06/10

STATEMENT 4: PREVIOUSLY APPROVED BAR ON ACCESS

I hereby give consent for my thesis, if accepted, to be available for photocopying and for inter-library loans **after expiry of a bar on access previously approved by the Graduate Development Committee.**

Signed .... (candidate) Date ....

Summary

A new GaAs based material system capable of emission at 1.55µm is a GaInNAsSb quantum well sandwiched between GaNAs barriers. This couples 1.55µm emission with the inherent ability of GaAs based devices to be made into Vertical cavity surface-emitting lasers (VCSELs), making it a very promising solution for cheap temperature stable laser material for optical fibre networks.

In this work the segmented contact method is used to measure the gain, loss and spontaneous emission (which is calibrated to give the radiative current density) of this material. These properties are compared for structures with: different doping levels, different nitrogen contents, different numbers of quantum wells; and different barrier widths.

The non-radiative current density is compared for structures with different well numbers and is used to show that the non-radiative recombination in a barrier is equal to that in one well. Further analysis using the simulation program "*Simwindows*" shows that this non-radiative current in the barrier is due to Shockley-Reed-Hall (defect) recombination.

It is shown that reducing the barrier size leads to an increase in non-radiative current due to reduced material quality. Leading to the conclusion that for progress to be made with GaInNAsSb active regions the barriers surrounding them need to be changed to GaAsP, or the material quality of GaNAs needs to be greatly improved.

The ultimate performance of GaInNAsSb as an active region is assessed by comparing its gain current characteristics with high performance 1.2-1.3µm InGaAs(N), and is shown to have the potential to require lower currents to achieve the same amount of gain, confirming that it is a material that demands further investigation and optimisation.

A method of comparing the sum of the fundamental properties of the matrix element, overlap integral and density of states, found experimentally, is proposed and used to establish the effects of nitrogen and antimony on these properties.

Acknowledgements

Firstly I would like to thank my supervisors Professor Peter Smowton and Professor Peter Blood. Without their help, guidance and support this thesis and the work within would not exist. I would also like to thank every member of the Optoelectronics group for the useful discussions and questions both answered and asked and for providing an enjoyable atmosphere in which to work.

I would like to thank the technical staff that have helped me; Steven Baker and Ian Robinson for supplying me with Nitrogen, Dr John Thomson and Karen Barnett for processing my samples and Rob Tucker for being able to fix any and all electrical equipment

I would like to thank my friends for making my time in Cardiff as fun and as memorable as it has been.

Finally I would like to thank my family for their endless support throughout my time as a student.

Acknowledgements II

I would like to thank the various publicans of Cardiff who have always been willing to provide cold beverages after a hard day/week/month/year in the lab and all the people that I have shared these times with.

I would like to thank Microsoft for creating the peerless program that is Word, I had no issues with it whatsoever and found it very easy to work with which is contrary to what some tried to make me believe. I would also like to thank them for creating the Xbox and the subsequent nights spent gaming and drinking with friends, which provided an excellent way to unwind.

Abstract

A new GaAs based material system capable of emission at 1.55μm is a quantum well of the quinary material GaInNAsSb sandwiched between GaNAs barriers. This material couples 1.55μm emission with the inherent ability of GaAs based devices to be made into Vertical cavity surface-emitting lasers (VCSELs), making it a very promising solution for a cheap temperature stable laser material for optical fibre networks.

In this work the segmented contact method is used to measure the gain, loss and spontaneous emission (which is then calibrated to give the radiative current density) of this material. These properties are compared for structures with: different levels of doping, different nitrogen contents, different numbers of quantum wells; and different barrier widths.

The non-radiative current density is compared for the structures with different well numbers and is used to show that the non-radiative recombination in a barrier is equal to that in one well. Further analysis using the simulation program "*Simwindows*" shows that this non-radiative current in the barrier is due to Shockley-Reed-Hall recombination (defect recombination).

Comparing the non-radiative current for the differently sized barriers and then applying further analysis with Simwindows shows that reducing the barrier size leads to an increase in non-radiative current due to reduced material quality. This then leads to the conclusion that in order for progress to be made with GaInNAsSb active regions the barriers surrounding them need to be changed to GaAsP, or the material quality of GaNAs needs to be greatly improved.

The ultimate performance of GaInNAsSb as an active region is then assessed by comparing the gain current characteristics of this with high performance 1.2-1.3μm InGaAs(N) lasers, and shown to have the potential to require lower currents to achieve the same amount of gain, for example to achieve a modal gain of 10cm^{-1} the GaInNAsSb would need 20mA compared to 28mA and 32mA for the 1.2-1.3μm InGaAs(N) and for a material gain of 1000cm^{-1} the GaInNAsSb would need 17.5mA compared to 42mA for InGaAs(N), confirming

that it is a material that demands further investigation and optimisation. In performing this comparison a method of comparing the sum of the fundamental properties of the matrix element, overlap integral and density of states, found experimentally, is proposed and then used to try to establish the effects of nitrogen and antimony on these properties.

1. Introduction

1.1 Introduction to Wavelength of Interest and Potential Materials

The ever expanding scope of what people are accessing through, and expect to be able to do on, the internet means that the bandwidth required is also increasing rapidly. These latest demands include streaming videos, downloading high definition films and an increase in online computer gaming. The current bottleneck in internet bandwidth comes from the "short haul" networks that connect individual homes and offices. This bottleneck can be removed by increasing the use of optical fibre networks over these short haul distances. Such a large scale undertaking will of course require low cost and reliable components.

The optical fibres that are used in these networks have the lowest attenuation at 1.55μm and the lowest dispersion at 1.3μm.

The devices that are currently used to achieve these wavelengths are InGaAsP on InP quantum well lasers. These devices exhibit a number of problems that make it desirable to find new sources at these wavelengths. These problems include the confinement of electrons in the conduction band; this confinement is low with a barrier height of typically 100meV (Silver and O'Reilly, 1995) which means that electrons are able to escape the confined structure (the quantum well) and recombine elsewhere in the structure. This effect will be become increasingly prominent at elevated temperatures meaning that InP based devices require cooling systems which adds to the overall laser package cost. However the main drawback for these InP based structures, when compared to the proposed GaAs based structures, lies in the manufacturing of vertical cavity surface emitting lasers (VCSELs). VCSELs are preferred over edge emitting lasers because they allow on-wafer testing and allow for more devices to be grown on a wafer due to having a smaller footprint; this reduces cost. VCSELs are easier to couple to optical fibres and tend to exhibit lower threshold currents due to the reduced mode volume. Essential to the operation of VCSELs is the ability to create Bragg mirrors. Finding material to make these mirrors on InP has proved very difficult. Many different methods have been tried to make commercially viable VCSELs on InP using metal mirrors (Soda et al, 1979), wafer bonded AlGaAs / GaAs mirrors (Jayaraman et al, 1998), di-electric mirrors (Uchiyama et al, 1997), AlGaAsSb / AlAsSb mirrors (Hall et al, 1999) and AlGaAs/GaAs combined with InAlGaAs/InAlAs mirrors (Yuen et al, 2000). More recently the use of high-contrast gratings to create InP VCSELs has been utilised (Chang-Hasnain, 2009) and devices have been shown emitting at 1.3µm (Hofmann, 2010) and predicted to emit at 1.55µm (Karagodsky, 2010). Although these structures do make working VCSEL devices they are still not commercially viable due to the complexity of growth and manufacturability as well as the inherent confinement problems and temperature sensitivity of the InP system.

The GaAs material system already has well established technology used to create Bragg mirrors from high contrast GaAs/AlGaAs layers, these are easy to grow with consistent quality (due to lattice matching). The AlAs can also be readily oxidised to provide confinement in the lateral direction. This means that finding a GaAs based material that emits at 1.3µm and even more importantly 1.55µm is essential.

There have been several different materials put forward to solve the problem such as InAs dots and GaAsSb/InGaAs type 2 quantum wells, which have so far struggled to go beyond 1.3µm. The devices used in this thesis are primarily GaInNAsSb/GaNAs quantum wells; a brief history behind the evolution of this initially complex looking mix of elements is discussed in the next section. Recent results of InAs dot edge emitting lasers operating at 1.3µm have been very promising (Tanaka, 2010), InAs dots have also been successfully utilised to create VCSELs emitting at 1.3µm although they suffer from self heating (Xu, 2010).

1.2 Motivation for the use of GaInNAsSb/GaNAs

The first step towards this material system came with the realisation that introducing a fraction of nitrogen into GaAs reduces the bandgap of the material (Weyers et al, 1992), then the subsequent discovery that introducing a small percent of nitrogen into InGaAs to form GaInNAs could be used as a gain medium (Kondow et al, 1997). The ability to use nitrogen in this way is due to the unusual behaviour between the lattice constant and the bandgap energy. A plot of bandgap energy vs lattice constant is shown in Figure 1 (Kondow et al, 1997)

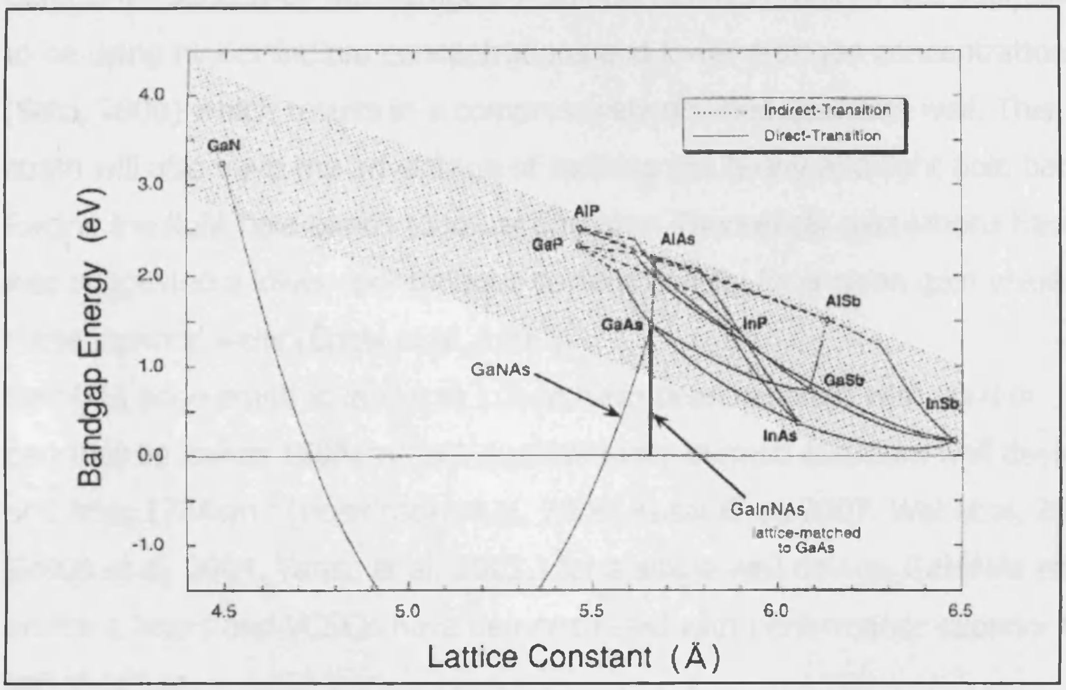

Figure 1. Bandgap energy vs lattice constant for some common III-IV semiconductor materials(Kondow, 1997)

Figure 1 shows the interesting feature of adding nitrogen, this being that both the bandgap and lattice constant decrease with increasing N, which is the opposite to the other materials shown. This means that by adding both In (which reduces the bandgap but increases lattice constant) and N (reducing both band gap and lattice constant) the bandgap can be lowered much further than was possible before, while keeping a relatively small or zero lattice mismatch to GaAs. The reason for this behaviour is that the nitrogen atoms introduce a localised state which interacts with the conduction band causing it to split into two highly parabolic sub-bands. This effect can be described by the band anticrossing model (Shan et al, 2001)

The conduction band offset of GaInNAs when grown on GaAs is larger than in InP based devices (Kondow et al, 1997. Tansu and Mawst, 2003) the electron effective mass is also bigger (Thranhardt et al, 2005) which leads to a better confinement of electrons.

Early GaAs lattice matched devices had high threshold current densities ≈ 700Acm^{-2} although they did display good temperature stability (Fehse et al, 2002, Kondow et al, 1997). The high current densities were attributed to defects introduced by the nitrogen. A solution to this problem was suggested to be using higher indium concentrations and lower nitrogen concentrations (Sato, 2000) which results in a compressively strained quantum well. This strain will also have the advantage of splitting the heavy and light hole bands, forcing the light hole bands to lower energies. Theoretical calculations have also suggested a lower spontaneous current density for a given gain value in these strained wells (Chow et al, 1999).

GaInNAs edge emitting lasers at 1.3μm have been reported with current densities as low as 150Acm^{-2} per quantum well in multi quantum well devices and from 178Acm^{-2} (Hopkinson et al, 2006. Kasai et al, 2007. Wei et al, 2005. Gollub et al, 2004, Tansu et al, 2002.) for a single well device. GaInNAs edge emitting lasers and VCSEls have demonstrated with performance superior to InP at 1.3μm.

However when trying to go to larger wavelengths than 1.3μm the GaInNAs material shows degradation, (Spruytte et al, 2000. Harris et al, 2004), which corresponds to an increase in threshold currents, for a 1000μm device the threshold current density increases from ≈ 600Acm^{-2} at 1.3μm to ≈4200Acm^{-2} at 1.52μm(Ulloa, 2005). The addition of antimony has been found to help this problem, both by acting as a surfactant which allows growth at higher temperatures reducing defects and also by incorporating into the material itself further helping to reduce the band gap (Yuen et al, 2005). Another material improvement made to help access 1.55μm is the use of GaNAs barriers either side of the quantum well. These are used to compensate for the large amount of strain in these wells (Pavelescu et al, 2002. Egorov et al, 2001). With these changes in place it has been possible to produce high performance edge emitting 1.55µm GaInNAsSb/GaNAs quantum well lasers with threshold currents ≈350Acm^{-2}(Bank et al, 2007. Gupta et al, 2006). Which are comparable with thresholds achieved with InGaAsP/ InP devices ≈ 360Acm^{-2} (Zegrya et al 2001).

1.3 The Relevance of this Thesis

Section 1.2 has detailed how the evolution of the GaInNAsSb/GaNAs lasers that are used in this work came to be. The main aim of my work contained within this thesis is to discover the source(s) of any non-radiative recombination that is/are present in these devices and to then suggest any improvements that can be made if any to increase performance. I will then compare the ultimate device performance of these 1.55µm devices to that of the 1.3µm GaInNAs mentioned above and to 1.2µm InGaAs, to discover the effects that the addition of both nitrogen and antimony have. The aim is to establishing if the ultimate performances of these devices warrant further investigation and improvements being made to this material system. I also propose a method for experimentally finding the sum of the matrix element, density of states and overlap integral, this is important as these quantities have a large effect on the gain and spontaneous current.

A list of presentations and publications arising from this work can be seen in the appendix found in chapter 9.

1.4 References

- Bank. S.R, Bae. H, Goddard. L.L, Harris. J.S, "Recent progress on 1.55µm Dilute-Nitride Lasers", IEEE Journal of Quantum Electronics, vol.43, no.9, pp773-785, 2007
- Chang-Hasnain. C.J, Zhou. Y, Huang. M.C.Y, Chase. C, "High-Contrast Grating VCSELs", IEEE Journal of Selected Topics In Quantum Electronics, 2009, 10. 1109. 2015195
- Chow. W.W, Jones. E.D, Modine. N.A, Allerman. A.A, Kurtz. S.R, "Laser gain and threshold properties in compressive-strained and lattice-matched GaInNAs/GaAs quantum wells". Vol.75, no.19, 2891, 1999
- Egorov. A.Y, Bernklau. D, Borchet. B, Illek. S, Livshits. D, Rucki. A, Schuster. M, Kaschner. A, Hoffmann. A, Dumitras. G, Amann. M.C, Riechert. H, "Growth of high quality InGaAsN heterostructures and their laser application". Journal of crystal growth, vol. 227-228, pp545-552, 2001
- Fehse. R, Tomic. S, Adams. A.R, Sweeney S.J, O'Reilly E.P, Riechert. H, "A Quantitative Study of Radiative, Auger, and Defect Related Recombination Processes in 1.3µm GaInNAs-Based Quantum-Well Lasers", IEEE Journal of Selected Topics in Quantum Electronics, vol. 8, no.4, 2002
- Gollub. D, Moses. S, Forchel. A, "Comparison of GaInNAs laser diodes based on two to five quantum wells", IEEE Journal of Quantum Electronics, vol. 40, no. 4, pp337-342, 2004
- Gupta. J.A, Barrios. P.J, Caballero. J.A, Poitras. D, Aers. G.C, Pakulski. G, Wu. X. "Gain and lifetime of GaInNAsSb narrow ridge waveguide laser diodes in continuous-wave operation at 1.56µm
- Hall. E, Almuneau. G, Kim. J.K, Sjolund. O, Kroemer. H, Coldren. L.A, "Electrically-pumped, single-epitaxial VCSELs at 1.55µm with Sb-based mirrors" Electronics letters, vol 36, no. 13, pp 1121-1123, 2000

- Harris J.S, Bank. S.R, Wistey. M.A, Yuen. H.B, "GaInNAs(Sb) long wavelength communications lasers", IEEE Proceedings of Optoelectronics, vol. 151, no.5, 2004
- Hofmann. W, Chase. C, Muller. M, Rao. Y, Grasse. C, Bohm. G, Amann. M.C, Chang-Hasnain. C. " Long Wavelength BTJ-VCSEL with High contrast Grating", CLEO/QELS 2010, CMO1
- Hopkinson. M, Jin. C.Y, Liu. H.Y, Navaretti. P, Airey. R, "1.34µm GaInNAs quantum well lasers with low room-temperature threshold current density", Electronics Letters, vol. 42, no. 16, pp. 923-924, 2006
- Jayaraman. V, Geske. J.C, MacDougal M.H, Peters. F.H, Lowes. T.D, Char. T.T, "Uniform threshold current, continuous-wave, singlemode 1300nm vertical cavity lasers from 0 to 70C" Electronics Letters, vol. 64, no. 14, pp1405-1407, 1998.
- Karagodsky. V, Pesala. B, Chase. C, Hofmann. W, Koyama. F, Chang-Hasnain. C.J, "Monolithically integrated multi-wavelength VCSEL arrays using high-contrast gratings", Optics Express, Vol.18, No.", 694
- Kasai. J, Kitatani. T, Adachi. K, Nakahara. K, Aoki. M "Growth of low-threshold GaInNAs/GaAs triple-quantum-well lasers", Journal of Crystal Growth, vol. 301-302, pp545-547, 2007, 14th International Conference on Molecular Beam Epitaxy, MBE XIV
- Kondow. M, Kitatani. T, Nakatsuka. S, Larson. M.C, Nakahara. K, Yazawa. Y, Okai. M, "GaInNAs: A novel material for long0wavelength semiconductor lasers", Journal of Selected Topics in Quantum Electronics, vol. 3, no.3, 1997
- Pavelescu. E.M, Jouhti. T, Pengm. C.S , Li. W, Konttinen. J, Dumitrescu. M, Laukkanen. P, Pessa. M, "Effects of insertion of strain-mediating layers on luminescence properties of 1.3µm GaInNAs/GaNAs/GaAs quantum-well structures". Journal of Crystal Growth, vol.241, no.1-2, pp.31-38, 2002
- Sato. S, "Low Threshold and High Characteristic Temperature 1.3 µm Range GaInNAs Lasers Grown by Metalorganic Chemical Vapor Deposition", Japanese Journal of Applied Physics, 39 (2000), 3403

- Shan. W, Walukiewicz. W, Yu. K.M, Ager. J.W, Haller. E.E, Geisz. J.F, Friedman. D.J, Olson. J.M, Kurtz. S.R, Xin. H.P, Tu. C.W, " Band Anticrossing in III-N-V Alloys", phys. stat. sol. (b) 223, 75 (2001)
- Silver. M, O'Reilly. E.P, "Optimumization of long wavelength InGaAsP strained quantum-well lasers", IEEE Journal of Quantum Electronics, 31, (1995) 1193
- Soda. H, Iga K.I, Kitahara. C, Suematsu. Y, "GaInAsP/InP Surface Emitting Injection Lasers" Japanese Journal of Applied Physics, vol. 18, no. 12, pp2329-2330, 1979
- Spruytte. S.G, Coldren. C.W, Marshall. A.F, Larson. M.C, Harris. J.S, "MBE growth of nitride-arsenide materials for long wavelength optoelectronics", Spring MRS meeting, vol. 5s1, p. W8.4, 2000
- Tanaka. Y, Ishida. M, Takada. K, Yamamoto. T, Song. H. Z, Nakata. Y, Yamaguchi. M, Nishi. K, Sugawara. M, Arakawa. Y, " 25Gbps Direct Modulation in 1.3µm InAs/GaAs High-Density Quantum Dot Lasers", CLEO/QELS 2010, CTuZ1
- Tansu. N, Kirsch. N.J, Mawst. L.J, "Low-threshold-current-density 1300nm dilute-nitride quantum well lasers", Applied Physics Letters, vol. 81, no. 14, pp2523-2525, 2002
- Tansu. N, Mawst. L.J, "The role of hole leakage in 1300-nm InGaAsN quantum-well lasers", Applied Physics Letters, vol 82, no.10, 2003
- Uchiyama. S, Yokouchi. N, Ninomiya. T, "Continuous-wave operation up to 36C of 1.3µm GaInAsP-InP vertical-cavity surface-emitting lasers" IEEE Photonics Technology Letters, vol9, no. 2, pp141-142, 1997
- Ulloa. J.M, Heirro. A, Montes. M, Damilano. B, Hughes. M, Barjon. J, Duboz. J.Y, Massies. J, " Impact of N on the lasing characteristics of GaInNAs/ GaAs quantum well lasers emitting from 1.29µm to 1.52µm", Applied Physics Letters, 87, 251109, 2005
- Wei. Y.Q, Sadeghi. M, Wang. S.M, Modh. P, Larsson. A, "High performance 1.28µm GaInNAs double quantum well lasers", Electronics Letters, vol. 41, no. 24, pp1328-1330, 2005

- Weyers. M, Sato. M, Ando. H, "Red shift of photoluminescence and absorption in dilute GaAsN Alloy Layers" Japanese Journal of Applied Physics, vol.31, pp 853-855, 1992
- Xu. D.W, Tong. C.Z, Yoon. S.F, Zhao. L.J, Ding. Y, Fan. W.J, "Self-heating effect in 1.3µm p-doped InAs/GaAs quantum dot vertical cavity surface emitting lasers", Journal of Applied Physics, 107, 063107, 2010
- Yuen. W, Li. G.S, Nabiev. R.F, Boucart. J, Kner. P, Stone. R.J, Zhang. D, Beaudoin. M, Zheng. T, He. C, Yu. K, Jansen. M, Worland. D.P, Chang-Hasnain. C.J, "High-performance 1.6µm single-epitaxy top-emitting VCSEL" Electronics Letters, vol 36, no. 13, pp1454-1123, 2000
- Yuen. H.B, Bank. S.R, Wistey. M.A, Harris. J.S, "Improved optical quality of GaNAsSb in the dilute Sb limt", Journal of Applied Physics, 97, 113510, 2005
- Thranhardt. A, Kuznetsova. I, Schlichenmaier. C, Koch. S.W, Shterengas. L, Belenky. G, Yeh. J.Y, Mawst. L.J, Tansu. N, Hader. J, Moloney. J.V, Chow. W.W, " Nitrogen incorporation effects on gain properties of GaInNAs lasers: Experiment and theory", Applied physics letters. 86, 201117, 2005
- Zegrya. G.G, Pikhtin. N.A, Skrynnikov. G.V, Slipchenko. S.O, Tarasov. I.S, "Threshold characteristics of λ = 1.55µm InGaAsP / InP Hetero lasers", Physics of semiconductor devices, vol 35, no. 8, pp1001-1008 2001

2. Semiconductor Laser Theory and Dilute Nitride Material Background.

2.1 Introduction

The aim of this chapter is to provide the background theory that will be needed to understand the work presented in this thesis and to predict the expected effects of including N and Sb on the gain, spontaneous current and non-radiative current.

2.2. Laser Diode Background

In this section I will briefly outline the conditions under which laser action occurs and will then describe the type of structures used in this work

2.2.1 Principle of Lasing

For light emission to be considered to be laser light it must retain the same wavelength, phase and polarisation of emission.

To create a laser a gain medium is sandwiched between two mirrors. Light travels back and forth along the cavity with a fraction of the light being emitted each time it reaches a mirror. The light that is not emitted is reflected back into the cavity, this keeps the emission coherent. If the gain (or amplification) is high enough in the cavity to match the losses present, the losses being the light that escapes each time the light reaches a mirror and internal scattering losses due to imperfections in the cavity, then lasing will occur, the gain that matches these losses is called the threshold gain, which can be described by Equation 1

$$G_{th} = \alpha_i + \frac{1}{L}\ln\left(\frac{1}{R}\right)$$

Equation 1

Here the α_i term refers to the internal scattering losses mentioned above and has units of cm^{-1}. The loss due to the transmission through the mirrors is calculated from the reflectivity of the mirrors, *R*, this is converted in units of reciprocal length as is shown in Equation 1, (both mirrors are assumed to be identical).

In the diode lasers that will be used in this thesis the gain medium is provided by a semiconductor material and the mirrors are provided by the semiconductor-air interface. In its natural state semiconductor material does not provide optical gain so it must be forced into a non-equilibrium state, this means forcing an excess of holes into low energy states and an excess of electrons into high energy states. The devices used in this thesis are oxide stripe lasers and achieve a non-equilibrium state by means of electrical injection. A schematic diagram of one of these structures is shown in Figure 2.

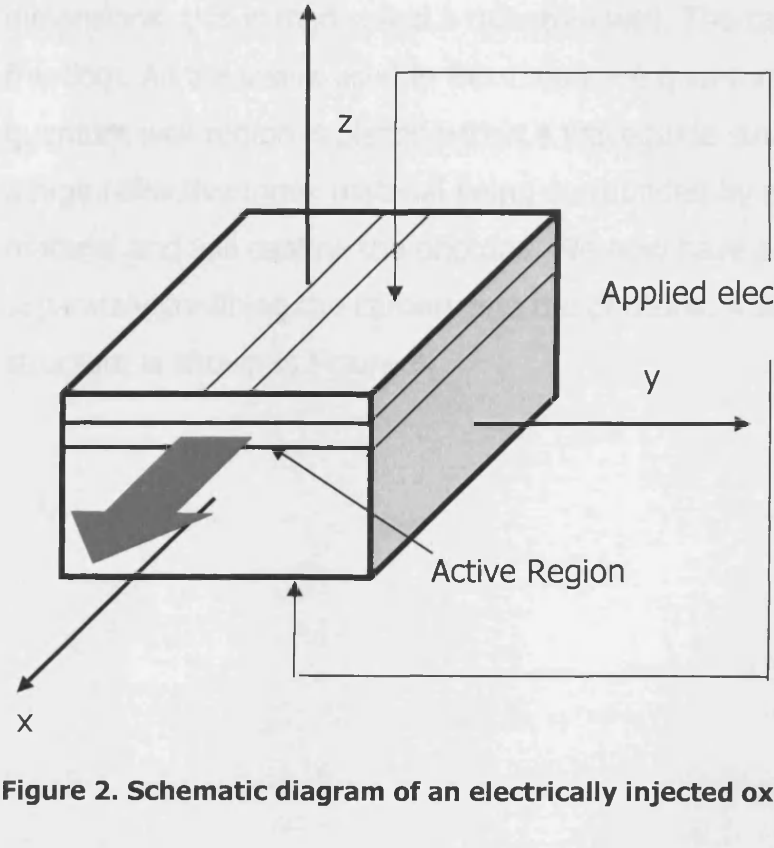

Figure 2. Schematic diagram of an electrically injected oxide stripe laser chip

In Figure 2 the top surface and the bottom surface have metal contacts on them, this allows current to be applied. A stripe can be seen in the top contact, this is the only part of the structure where carriers can pass from the top contact into the active region of the device and leads to confinement of the carriers in the *y* direction. The stripe is defined by a region of oxide before the metal contact is attached. The *z* direction is the direction that the growth of the structure has occurred, *x* is the direction that light is emitted. The active region of the laser where light is generated is marked on Figure 2; light is only generated below the oxide stripe.

2.2.2 Quantum Well Structure

Bulk lasers involve the sandwiching of an active region between n and p-doped semiconductor layers that have a larger band gap than the active region. Electrons are then injected from the n-doped side and holes from the p-doped. If this active region is reduced in thickness to around 10nm or less the effect of quantum confinement is utilised. The carriers are then confined in the direction of the growth as this is far smaller than the other two dimensions, this is then called a quantum well. The carriers have 2 degrees of freedom. All the lasers used in this thesis are quantum well (QW) lasers. This quantum well region is placed within a waveguide structure which consists of a high refractive index material being surrounded by a lower refractive index material and will confine the photons. We now have a structure that is separately confining the carriers and the photons. A schematic of this structure is shown in Figure 3

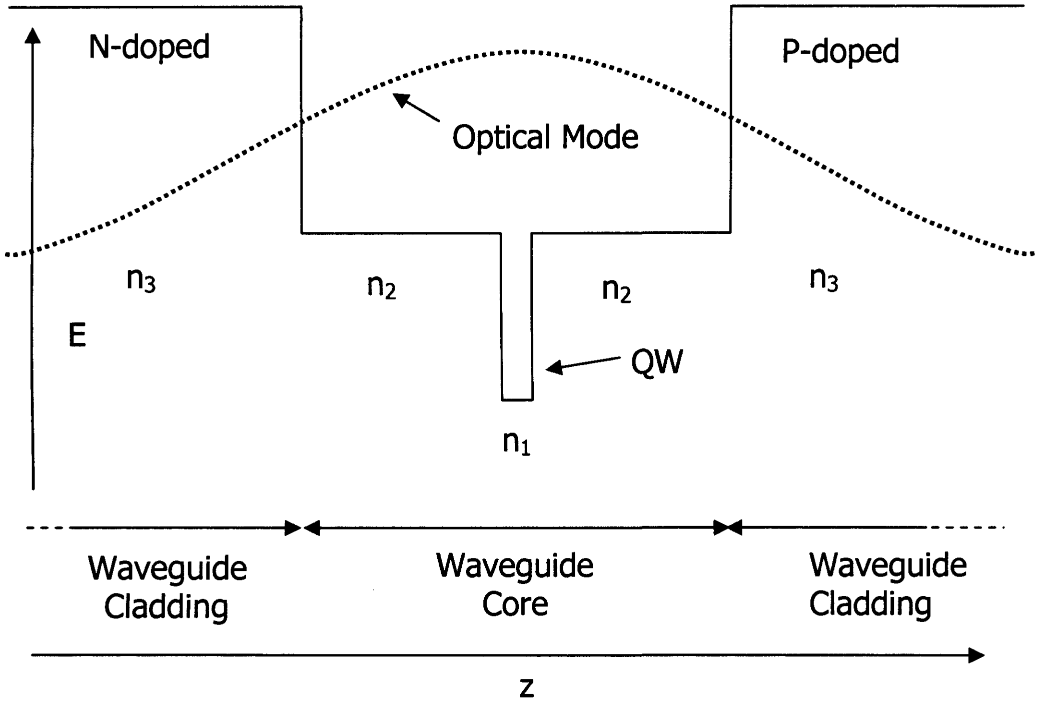

Figure 3. Schematic diagram of the band gap in a QW laser. The dashed line shows the optical mode. The cladding and waveguide core are marked. The refractive indices of the waveguide are marked too ($n_2>n_3$). The *z* axis shows the direction of growth. The waveguide core is the region marked active region in figure 2.

QW devices have several advantages over bulk devices, which include changes to the density of states, the ability to fine tune the wavelength of emission by adjusting the size of the well, the ability to use strain within the active region to further tune the wavelength emission and polarisation of the emission. Details of quantum well theory are discussed in the next section.

2.3 Quantum well theory

2.3.1 Aims of section

The aim of this section is to detail the quantum well theory that will be used in some of the extended analysis in this work. It is also used to provide the background on the origin of the more complex equations used later in this thesis. The derivations in this entire section follow the approach that can be found in (Coldren and Corzine, 1995).

2.3.2 Energy Bands and effective mass

The periodicity of the semiconductor lattice leads to the creation of energy bands instead of the discrete energy levels that are seen in an individual atom. The highest occupied energy level of the atoms splits to form the valence band, the lowest unoccupied energy band then splits to form the conduction band. The separation between these two bands is referred to as the energy gap (E_g). The lowest transition energy however is larger than this, this is due to the effect of the confinement by the quantum well. A typical band structure showing the valence and conduction band can be seen in the energy (*E*) vs. wave vector (*k*) plot in Figure 4.

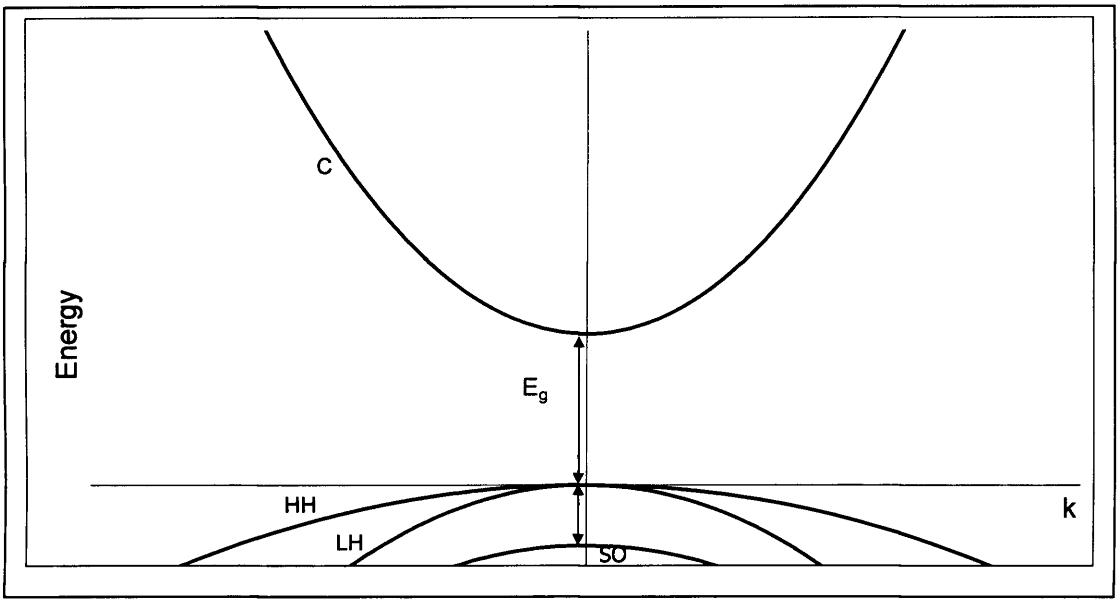

Figure 4. Semiconductor band structure, depicted in k space, for the conduction band (C), heavy hole (HH), light hole (LH) and split off band (SO) are indicated. k is the wave vector.

Figure 4 shows that the conduction band is made up of only one band whereas the valence band is made up of three bands. At 0K the valence band will be full of electrons and the conduction band will empty. At higher temperatures or under external excitation, some electrons from the valence band will have enough energy to cross the energy gap and go into the conduction band leaving a hole behind them. The electrons and the holes can then recombine and light is generated. Recombination can only happen between electrons and holes that have the same k vector.

For low values of k it is possible to approximate the energy band structure to a parabola, the effective mass can then be described by Equation 2.

$$m^* = \frac{\hbar^2}{\frac{d^2E}{dk^2}}$$

Equation 2

This shows that the effective mass is effectively a measure of the curvature of the E-k band.

If strain is incorporated into a structure this affects the position of the bands, particularly the valence bands. Strain is introduced by using materials that have different lattice parameters, if a material with a smaller lattice constant is grown on top of one that has a larger lattice constant the smaller lattice constant material will be under tensile strain. The wells that are used in this thesis are under compressive strain, under compressive strain the LH band will shift to a lower energy than the HH band: the SO also shifts to a lower energy when compared to the HH band. The hydrostatic strain causes both the LH and HH band to shift to a lower energy, the shear strain then causes the HH band to move to a value above this new energy and the LH band to below this energy. This splitting of the bands has implications for the polarisation of light that is emitted, this is because in a quantum well the C-HH transition only emits TE polarised light, the C-LH transition produces TM emission 2/3 of the time (these fractions are true at k=0). These polarisations are with respect to the quantum well plane and are indicated in Figure 5.

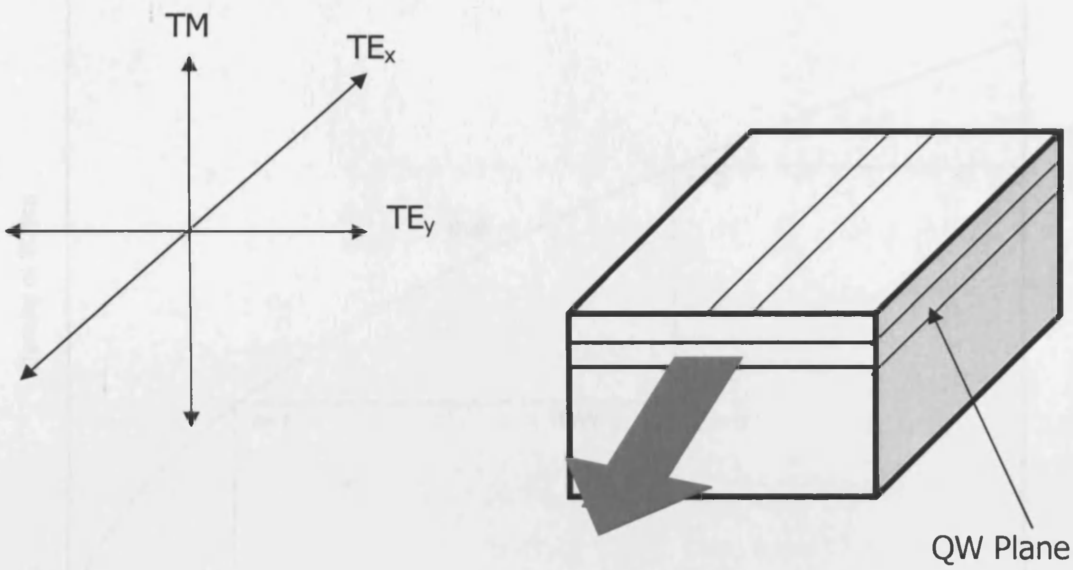

Figure 5. Show a device with the quantum well region marked. Shown for reference are the polarisations. This orientation with respect to the quantum well plane is consistent throughout this thesis

2.3.3 Density of states

This discussion of density of states follows the method set out in (Hook and Hall, 1999). Because in a quantum well there is confinement in one dimension the density of states will be different than in a bulk material. This difference is shown in Figure 6.

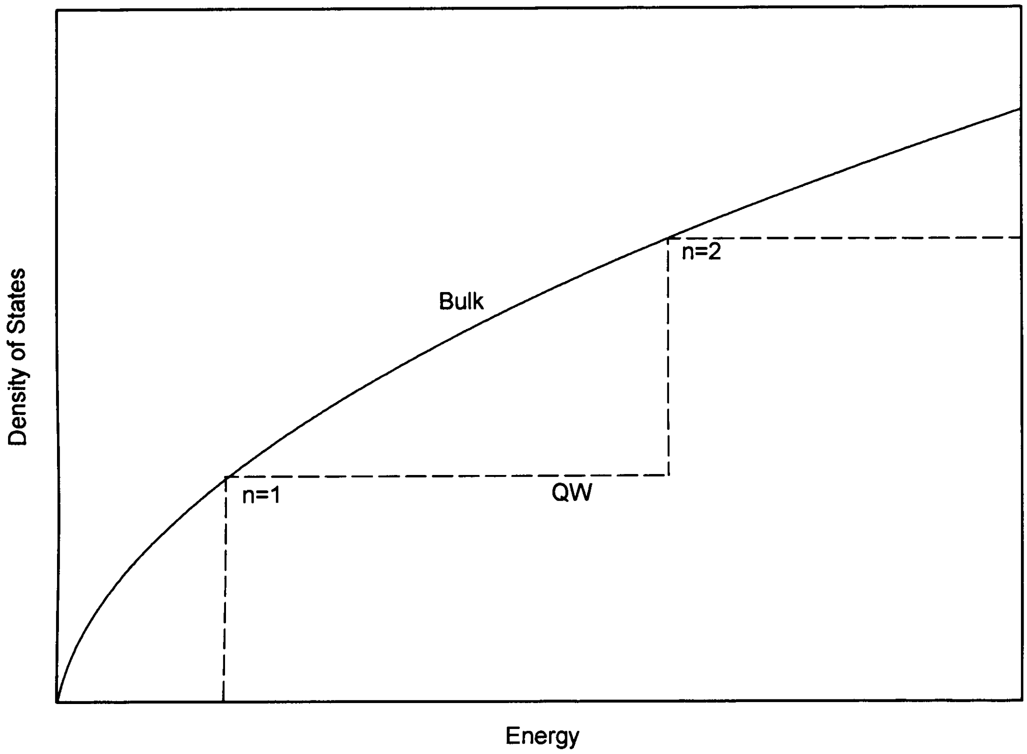

Figure 6. Density of states as a function of energy for a bulk material and a quantum well, the form of the bulk density of states is a parabola.

Looking at Figure 6 one of the benefits of a quantum well system can be seen, that is for a given energy of emission the QW system posses a lower density of states.

It is important to know the form that the density of states function (*ρ(E)*) will take. Because a QW has confinement in one direction the carriers are confined to sub-bands (the n=1 and n=2 sub-bands are shown in Figure 6), each sub-band has a fixed value of k_z, however the carriers in the sub-band are free to move in the x, y plane (in the k_x and k_y directions), producing a continuum of states associated with each sub-band. Because of this it is most convenient to express the density of states per unit area instead of per unit volume.

The area of each state in k space is $(2\pi/L)^2$. The total number of states in an interval between k and k+dk in one quadrant of the 2D space is then

$$g(k)dk = \frac{2\pi k dk}{(2\pi / L)^2} = \frac{L^2 k dk}{2\pi}$$

Equation 3

Dividing this by the area of the sample will give the density of states

$$\rho(k) = \frac{k}{2\pi} dk$$

Equation 4

This is the density of states in k space. It is however preferable to know the density of states per unit energy interval, *ρ(E)*. This is related to the density of states per unit *k* by

$$\rho(E)dE = 2\rho(k)dk$$

Equation 5

The two is included because of the two possible spin states for the electron. If we assume parabolic bands the E-K curve can then be described by

$$E = \frac{\hbar^2 k^2}{2m^*}$$

Equation 6

Where m^* is the effective mass. Using Equation 4, Equation 5 and Equation 6 *ρ(E)* can be described by

$$\rho(E) = \frac{m^*}{\pi \hbar^2}$$

Equation 7

Looking at Equation 7 we can see that $\rho(E)$ is proportional to m^*, this is likely to be different for the valence bands and the conduction band so $\rho(E)$ will also be different.

2.3.4 Occupation of States

In the previous section the density of states was worked out. This can be used to describe how many of these available states will be occupied, ($n(E)$). To work this out the density of states at a particular energy is multiplied by the probability that the state at that energy will be occupied.

If the carriers in the system are in thermal equilibrium then the probability of occupation is described by a Fermi function shown in Equation 8

$$f(E) = \frac{1}{1 + \exp\left(\frac{E - E_f}{kT}\right)}$$

Equation 8

When carriers are being continuously injected separate Fermi functions are needed to describe the electrons in the conduction band and the holes in the valence band, these are controlled by separate Fermi levels in the conduction band and in the valence band. These separate Fermi functions are labelled $f_c(E)$ and $f_v(E)$.

2.3.5 Matrix elements and transition rates

The discussion in this section follows that taken in (Coldren and Corzine, 1995 and Blood, 2000). There are three possible transitions between the valence and conduction band that involve the absorption or generation of a photon. The first of these is absorption; an electron is excited from the valence band into the conduction band by a photon of energy equal to that transition. The next is spontaneous emission; an electron in the conduction band relaxes into an available valence band state emitting a photon which can be emitted in any direction. The final transition is stimulated emission; here the electric field of a photon (with energy $h\nu_1$) perturbs an electron in the conduction band

which causes that photon to relax back into the valence band (which is hv_1 lower in energy) emitting a photon. This emitted photon has the same energy and phase and is travelling in the same direction as the original photon.
The transitions between states are governed by Fermi's golden rule which gives the transition rate per unit area and is described by Equation 9 and refers to an electron being excited from an initial discrete state to a continuum as indicated by Figure 7

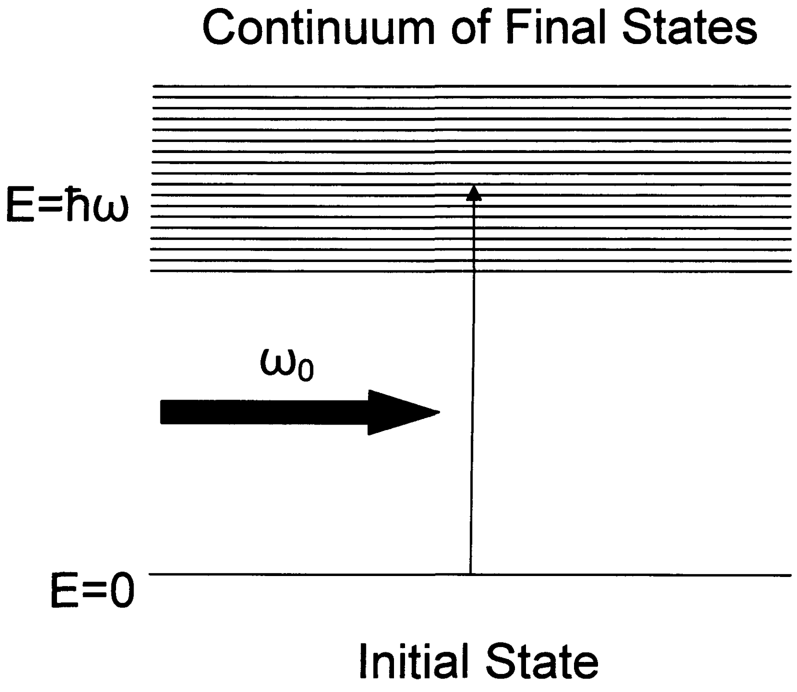

Figure 7. Electron excitation. Showing the initial discrete state and final continuum of states.

$$R(\hbar\omega) = \frac{2\pi}{\hbar}\left|H'_{12}\right|^2 \rho(\hbar\omega)$$

Equation 9

$\left|H'_{12}\right|^2$ is the matrix element, the subscript 1 and 2 denote the initial and final states the initial state here is defined as being at E=0, the matrix element determines the strength of interaction between two states where $\left|H'_{12}\right|^2$ is described by Equation 10

$$\left|H'_{12}\right|^2 = \left(\frac{e}{2m_0}\right)^2 \left|M\right|^2 \left\{\int_V F_2^*(r)A(r)F_1(r)d^3r\right\}^2$$

Equation 10

where *A(r)* is the vector potential. $\left|M\right|^2$ is referred to as the momentum matrix element, due to the microscopic potential of the atomic lattice of the material in the well, *F(r)* are the envelope functions and for a QW in the *xy* plane can described by Equation 11. The function *F(r)* in the *x* and *y* directions are plane wave solutions to Schrödinger's equations.

$$F(r) = F(z)\frac{1}{\sqrt{A}}e^{-ik_{xy}r_{xy}}$$

Equation 11

where *r* is the position vector and *k* describes the plane wave states in the x, y plane. The xy part of the integral in the {} parenthesis in Equation 10 is only non-zero when the transition is between plane wave solutions that have the same value of *k*. This is known as the k selection rule.

By substituting Equation 11 and Equation 10 into Equation 9 the transition rate can now be written as

$$R(\hbar\omega) = \frac{2\pi}{\hbar}\left(\frac{e}{2m_0}\right)^2 \left|M\right|^2 \left\{\int F_2^*(z)A(z)F_1(z)dz\right\}^2 \rho_2(\hbar\omega)$$

Equation 12

The *F(z)* terms are the envelope functions across the well. Equation 12 is for a transition from a single occupied state represented by the suffix 1 to a continuum of unoccupied states represented by the suffix 2. This however is not what is actually happening, instead the transition is between the valence band and the conduction band. This means that both the initial and final states are part of a continuum, so the density of states function that is used Equation 12 must now become the reduced density of states (ρ_{red}), which takes into account the continuum of states. It is also consistent with k selection rules.

$$\frac{1}{\rho_{red}} = \frac{1}{\rho_c} + \frac{1}{\rho_v}$$

Equation 13

where ρ_c and ρ_v are the density of states of the conduction and valence bands respectively. Equation 12 currently assumes that the initial state is full and that the final state is empty. To take account of situations when this is not the case the probability of occupation of the states must be included.

This means that the equation describing a downwards transition from the conduction band to the valence band is given by Equation 14

$$R_{down}(\hbar\omega) = \frac{2\pi}{\hbar}\left(\frac{e}{2m_0}\right)^2 |M|^2 \left\{\int F_2^*(z)A(z)F_1(z)dz\right\}^2 \rho_{red} f_c(1-f_v)$$

Equation 14

f_c and f_v represent the probability of a state being occupied by an electron. Equation 14 is easily modified to represent the upward transition, by swapping the f_c and the f_v terms with each other. The net downward transition rate is then given by Equation 15

$$R_{net}(\hbar\omega) = \frac{2\pi}{\hbar}\left(\frac{e}{2m_0}\right)^2 |M|^2 \left\{\int F_2^*(z)A(z)F_1(z)dz\right\}^2 \rho_{red}(f_c - f_v)$$

Equation 15

2.3.6 Modal Gain

Figure 8 (Blood, 2000) serves as a reference for the geometry of the system that is discussed here.

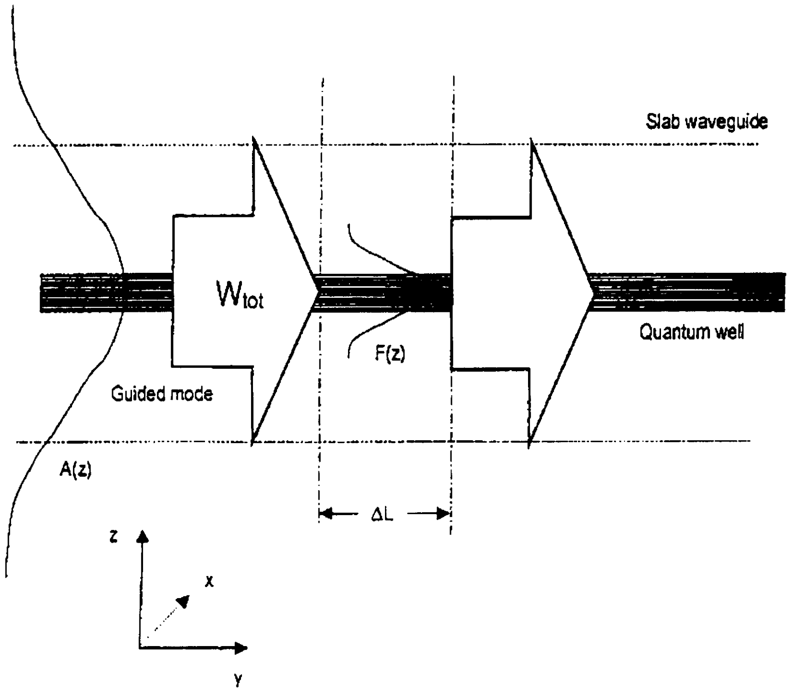

Figure 8. Schematic diagram of an optical mode propagating along a quantum well in a slab waveguide. (Blood, 2000)

Since R_{net} is uniform over the *x*, *y* plane, for a beam of width *w* in the *x* direction the rate of increase of W_{tot} over a distance ΔL in the *y* direction is

$$\frac{dW_{tot}}{dt} = (\hbar\omega)R_{net}w\Delta L$$

Equation 16

W_{tot} is the total energy density in the mode. For a harmonically varying field the local energy density is given by

$$W(r) = \frac{1}{2}nn_g\varepsilon_0\omega^2|A(r)|^2$$

Equation 17

where *A(r)* is the vector potential which is related to the electric field strength (ε) for time-harmonic fields by $|\varepsilon|^2 = \omega^2|A(r)|^2$. The total energy in the mode over the distance ΔL is

$$W_{tot} = \frac{1}{2}nn_g\varepsilon_0\omega^2\left(\int A^2(z)dz\right)w.\Delta L$$

Equation 18

The fractional increase in the total energy density in the mode is defined as the gain. In terms of time this is given by

$$G_t = \frac{1}{W_{tot}}\frac{dW_{tot}}{dt}$$

Equation 19

where *G* is the gain. By substituting in the group velocity of the mode Equation 19 becomes

$$G = \frac{n_g}{c}\frac{1}{W_{tot}}\frac{dW_{tot}}{dt}$$

Equation 20

Substituting Equation 16, Equation 18 and Equation 15 into Equation 20 gives

$$G(\hbar\omega) = \frac{4\pi\hbar}{nc\varepsilon_0(\hbar\omega)}\left(\frac{e}{2m_0}\right)^2 |M|^2 \left\{\int F_v^*(z)A(z)F_c(z)dz\right\}^2 \rho_r(h\nu)(f_c - f_v)\frac{1}{\int A^2(z)dz}$$

Equation 21

The quantity *A(z)* within the {} parenthesis can be considered to be almost uniform over the width of the well and so can be treated as having a constant value in the well and termed A_{well}, it can then be removed from the integration. Defining an optical confinement factor as

$$\Gamma = \frac{A_{well}^2 L_z}{\int A^2(z)dz}$$

Equation 22

means that Equation 21 can now be expressed as

$$G(\hbar\omega) = \left[\frac{4\pi\hbar}{nc\varepsilon_0(\hbar\omega)}\left(\frac{e}{2m_0}\right)^2 |M|^2 \left\{\int F_v^*(z)F_c(z)dz\right\}^2 \rho_r(h\nu)(f_c - f_v)\frac{1}{L_z}\right]\Gamma$$

Equation 23

This defines the gain.

2.3.7 Spontaneous Emission

The spontaneous recombination rate per unit area into a single mode can be derived by inserting the appropriate Fermi factors and by inserting a value for the vector potential equivalent to a single photon, as is described in (Coldren and Corzine, 1995) into Equation 12. The vector potential for a single photon is given by

$$|A|^2 = \frac{2(\hbar\omega)}{n^2\varepsilon_0\omega^2 V_{\mathrm{mode}}}$$

Equation 24

where *V_{mode}* is the volume of the mode and *n* is the refractive index

To calculate the spontaneous emission rate into all modes the rate for a single mode is multiplied by the total number of available modes. The mode density per unit volume in one polarisation is given by

$$\rho_{opt}(\hbar\omega) = \frac{1}{3\pi^2}\frac{n^2 n_g}{(\hbar c)^3}(\hbar\omega)^2$$

Equation 25

This can be multiplied by three to give the mode density in all three polarisations. The spontaneous recombination rate per unit area is defined as

$$R_{spon}(h\nu) = \frac{16\pi n}{\varepsilon_0 c^3 h^2}(h\nu)\left(\frac{e}{2m_0}\right)^2 |\overline{M}|^2 \left\{\int F_v^*(z)F_c(z)dz\right\}^2 \rho_{red}(h\nu) f_c(1-f_v)$$

Equation 26

where $|\overline{M}|^2$ is the matrix element averaged over all polarisations and directions. The refractive index *n* is taken to be the average refractive index experienced by all modes.

2.3.8 Population Inversion Factor

Converting Equation 26 so it is defined in terms of $(\hbar\omega)$ instead of $(h\nu)$ and then converting to give the spontaneous recombination rate per unit energy interval per unit area in the *(x, y)* plane in the polarisation *p* gives

$$I^{p}_{spon}(\hbar\omega) = \frac{1}{3}\frac{4n}{\varepsilon_0 c^3 \pi\hbar^2}(\hbar\omega)\left(\frac{e}{2m_0}\right)^2 \left|M^p\right|^2 \left\{\int F_v^*(z)F_c(z)dz\right\}^2 \rho_{red}(\hbar\omega) f_c(1-f_v)$$

Equation 27

where $\left|M^p\right|^2$ is the momentum matrix element for transitions of polarisation *p*. The extra 1/3 term has appeared to convert the total optical mode density into the mode density for one polarisation.

The ratio of modal gain given by Equation 23 to the spontaneous emission given above in Equation 27 is

$$\frac{G^p(h\nu)}{I^p_{spon}(h\nu)} = \frac{3\pi^2\hbar^3c^2}{n^2(\hbar\omega)^2}\left(\frac{f_1-f_2}{f_1(1-f_2)}\right)\left(\frac{\Gamma}{L_z}\right)$$

Equation 28

where $\left(\frac{f_1-f_2}{f_1(1-f_2)}\right)$ is defined as being the population inversion factor P_f.

2.4 Background to GaInNAsSb

The motivation for emission at the 1.55μm wavelength and a brief overview of the material development history were covered in chapter 1. The purpose of this section is to provide some background information on what is to be expected when including nitrogen and antimony with InGaAs and how it will affect the fundamental properties of a laser device.

2.4.1 Material Quality

The inclusion of nitrogen into InGaAs has been shown to lead to the formation of non radiative sites (Ni et al, 2007, Sarzala and Nakwaski, 2007), which means that the non-radiative current in samples with a higher nitrogen content would be expected to be larger.

All the GaInNAsSb samples used in this thesis are grown using molecular beam epitaxy (MBE). Only three of these elements require careful control of their flux for accurate emission wavelength control. This means that growth conditions are repeatable and many samples of the same quality and composition can be grown. The nitrogen flux is kept constant so the gallium and indium fluxes (and ratio of them) will control the nitrogen content. The arsenic flux is high so that the antimony concentration is governed by the antimony flux, meaning that control of the ratios of all the elements is controlled by the indium, gallium and antimony fluxes. This does have the affect that the nitrogen content in the barriers (where there is no indium) is up to 40% higher than in the well. (Bank et al, 2007 and private communication H. Bae). This means that any defects introduced by nitrogen will be of higher density in the barrier than in the well.

2.4.2 Gain and Spontaneous Current

Chapter 6 of this thesis will deal extensively with gain-spontaneous current relationships. Here I introduce some of the effects that changing the nitrogen content will have on these quantities and what effect the inclusion of nitrogen will have, the idea of this section is primarily to serve as a reference for comments made in chapter 6.

As well as introducing defects to the material the inclusion of nitrogen will also cause the electrons to become more localised around the N atoms (Nin et al, 2003) which will lead to a lower saturated gain value as the overlap integral between the electron and hole wave function will be reduced. This will also reduce the spontaneous emission.

Adding nitrogen increases the effective mass of the electrons (Thranhardt et al, 2005), it has a similar but far smaller effect on the mass of heavy holes. The inclusion of antimony will very slightly increase the electron mass and again slightly reduces the heavy hole mass. This means that on moving to materials that contain larger amounts of nitrogen the density of states for the electrons will increase and as a consequence of this the reduced density of states will also increase. Looking at Equation 21 for the modal gain and Equation 27 for the spontaneous emission it can be seen that an increase in the reduced density of states will increase both the gain and the spontaneous emission.

The addition of Nitrogen reduces the band gap of the material, adding antimony has the same effect. Again looking at the equations for modal gain and spontaneous emission it can be seen that a reduction in the *(hv)* term will increase the modal gain but will decrease the spontaneous emission.

This change in band gap and effective mass will also affect the Matrix element that appears in both the equation for spontaneous emission and modal gain. The matrix element can be described by Equation 29 (Coldren and Corzine, 1995)

$$|M|^2 = \left(\frac{m_0}{m^*} - 1\right)\frac{(E_g + \Delta)}{2\left(E_g + \frac{2}{3}\Delta\right)} m_0 E_g$$

Equation 29

where m^* is the effective conduction band mass, E_g is the energy gap (between the conduction and valence band) and Δ is the separation between the light hole and split of band. If Δ is sufficiently small in comparison to E_g, the the above equation can be written as

$$|M|^2 = \left(\frac{m_0}{m^*} - 1\right)\frac{1}{2} m_0 E_g$$

Equation 30

The matrix element squared is directly proportional to the ratio of fundamental material band gap (E_g) to the conduction band effective mass. This means that the reduction in band gap that the nitrogen causes will reduce the matrix element, reducing both the spontaneous emission and the gain.

2.4.3 Band Anticrossing

To describe the effect the inclusion nitrogen has on the conduction band and therefore the band gap of III-V semiconductors it is necessary to use the band anticrossing model for a more detailed description of this see (Shan et al, 2001). Other approaches have been tried such as the phenomenological Quantum Dielectric Theory and microscopic band structure calculations, however these could not easily be compared with experiments due to difficulties with the treatment of the random distribution in the alloys. More recently the local density approximation has been tried.

The nitrogen atom introduces a localised energy state with energy level E_N. This state is usually located near to the conduction band edge. The interaction of the conduction band edge with this localised nitrogen state results in a characteristic anticrossing giving rise to a splitting of the conduction band into two highly nonparabolic subbands which are labelled $E_-(k)$ and $E_+(k)$. With the $E_-(k)$ band being at a lower energy than the original conduction band, hence the reduction in band gap.

2.5 References

- Bank. S.R, Bae. H, Goddard. L.L, Harris. J.S, "Recent progress on 1.55μm Dilute-Nitride Lasers", IEEE Journal of Quantum Electronics, vol.43, no.9, pp773-785, 2007
- Blood. P "On the dimensionality of optical absorption, gain, and recombination in quantum-confined structures". IEEE Journal of Quantum Electronics, vol.36, no.3, 2000
- Coldren. L.A and Corzine. S.W, Diode Lasers and Photonics Integrated Circuits, Wiley Series in Microwave and Optical engineering, Vol 1, Kai Chang, 1995
- Hook. J.R, Hall. H.E. Solid State Physics, second edition. The Manchester Physics Series, Wiley. 1999
- Ni. H.Q, Niu. Z.C, Fang. Z.D, Huang. S.S, Zhang. S.Y, Wu. D.H, Shun. Z, Han. Q, Wu. R.H, "Optimization of GaInNAs(Sb)/GaAs quantum wells at 1.3–1:55 μm grown by molecular beam epitaxy". Journal of crystal growth, 301-302, pp125-128, 2007.
- Nin. Z.C, Ni. H.Q, Xu. H.X, Zhang. W, Zu. Y.Q, Wu. R.H, "Electronic properties of GaAs/GaInNAsSb superlattices". Phys Rev B, 68, 235326, 2003.
- Sarzala. R.P, Nakwaski. W, "GaInNAsSb/GaNAs quantum-well VCSELs: Modelling and physical analysis in the 1.50-1.55μm wavelength range". Journal of applied physics, vol. 101, 7, pp073103, 2007
- Shan. W, Walukiewicz. W, Yu. K.M, Ager. J.W, Haller. E.E, Geisz. J.F, Friedman. D.J, Olson. J.M, Kurtz. S.R, Xin. H.P, Tu. C.W, " Band Anticrossing in III-N-V Alloys", phys. stat. sol. (b) 223, 75 (2001)
- Thranhardt. A, Kuznetsova. I, Schlichenmaier. C, Koch. S.W, Shterengas. L, Belenky. G, Yeh. J.Y, Mawst. L.J, Tansu. N, Hader. J, Moloney. J.V, Chow. W.W, " Nitrogen incorporation effects on gain properties of GaInNAs lasers: Experiment and theory", Applied physics letters. 86, 201117, 2005

3. Measurement Technique

3.1 Introduction.

In this chapter I will detail the experimental technique that will be used throughout this thesis. I will discuss the preliminary device checks, the measurement technique, the equations used and show examples of results. I will also show how these initial results can be used to produce plots of more complex quantities.

3.2 Brief Overview of Technique

The technique used throughout this thesis is called the segmented contact method (SCM) (Thomson et al, 1999 and Blood et al, 2003). The SCM is a single pass experiment and involves collecting amplified spontaneous emission (spontaneous emission that has been amplified by passing through a gain medium) as a function of electrically pumped device length.

The amplified spontaneous emission (ASE) collected from this measurement is used to produce modal gain and absorption data in real units as a function of photon energy. These can then be used to produce spontaneous emission rate spectra (Blood et al ,2003), which will be discussed later in this chapter. The SCM is used because of the advantages it has over other techniques (Thomson et al, 1999) such as the ability to obtain the loss in real units and to perform the measurements at carrier densities above threshold.

3.3 Device Details

The devices that are used are fabricated in-house in Cardiff University by technical staff. They are fabricated into 50µm wide oxide stripe lasers and the top electrical contact is split up into 300µm long electrically isolated sections. A diagram of a SC device is shown in Figure 9.

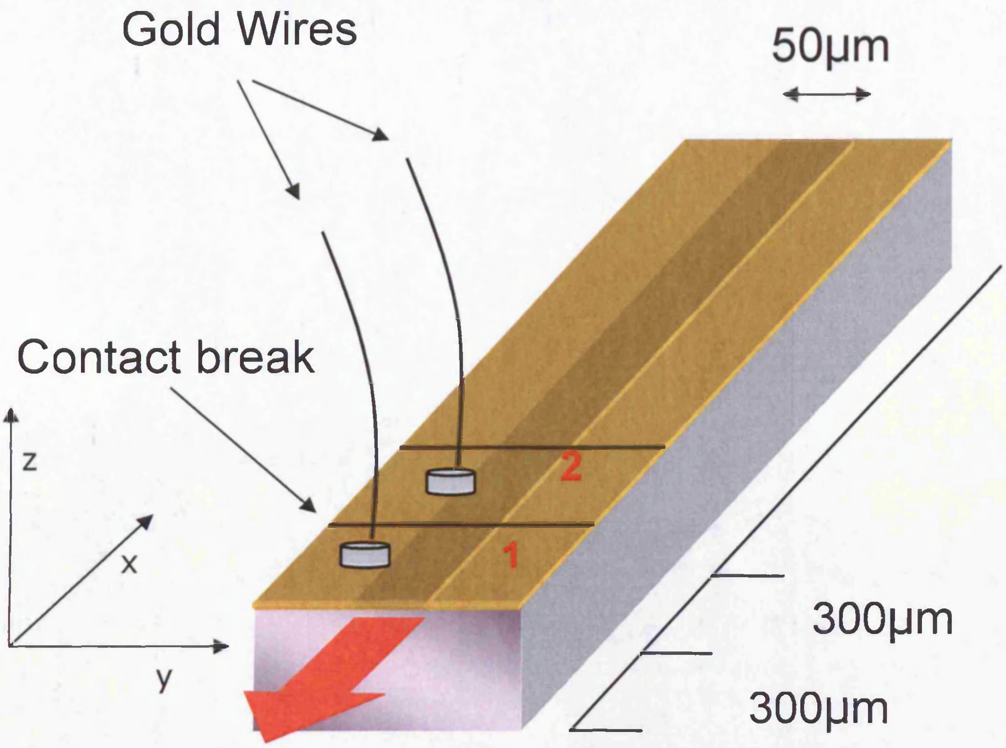

Figure 9. Diagram of a SC device. Marked on it is the contact break used to isolate sections, the wires are used to electrically pump the sections. The red arrow indicates where light is emitted.

The front two sections shown in Figure 9 are used to vary the length of the device that is being pumped; just section one, just section two or both section one and two together can be pumped. The long back section is not pumped, this acts as an absorbing region and prevents any round trip.

3.4 Segmented Contact Method Theory and Technique

The SCM requires the ASE emitted from the edge of an electrically pumped diode to be collected as a function of pump length. Electrical current is applied to the top contact injecting carriers into the active region, some of these carriers will then spontaneously recombine, some of the photons produced in this manner will be coupled into the optical mode (coupled into the waveguide) in the active region, these photons will then be amplified as they pass through the pumped region of the diode by the process of stimulated emission turning the spontaneous emission into amplified spontaneous emission.

To define the modal gain and absorption, firstly the spontaneous emission rate for light of a given polarisation per unit energy interval per unit area in the plane of the device must be considered and this is labelled I_{spon}. Throughout this analysis, the x direction is considered to be the propagation direction of the light, the z direction is the growth direction and this is normal to the quantum well plane and the y direction is in the plane of the quantum well, as is indicated in Figure 9.

The emission rate at the end of the waveguide, which originates from the spontaneous emission produced in a region Δx which is a distance x from the end of the waveguide is

$$I(x) = \beta I_{spon} e^{(G-\alpha_i)x} \Delta x$$

Equation 31

where G is the modal gain, α_i is the internal waveguide loss and β is the fraction of the spontaneous emission that is coupled into the waveguide.

If I_{spon} is uniform over the entire length of current injection then the total ASE from a stripe of length L is

$$I(L) = \int_0^L \beta I_{spon} e^{(G-\alpha_i)x} dx = \beta I_{spon}\left(\frac{e^{(G-\alpha_i)L} - 1}{G-\alpha_i}\right)$$

Equation 32

We can now describe the measured ASE in three situations: *I(1)* when just the front section (section 1) of the device is being pumped which is defined in Equation 33; the measured ASE when both the front two sections (sections 1+2) are being pumped is *I(1+2)* as given in Equation 34; the measured ASE when just the 2nd section (section 2) is being pumped which is defined as *I(2)* in Equation 35. As shown in Figure 9 the front two sections are of identical length, the lengths of these sections will be referred to here as being *L* therefore the length of two sections being pumped together is *2L*.

$$I(1) = (\beta I_{spon})\left(\frac{e^{(G-\alpha_i)L} - 1}{G-\alpha_i}\right)$$

Equation 33

$$I(1+2) = (\beta I_{spon})\left(\frac{e^{(G-\alpha_i)2L} - 1}{G-\alpha_i}\right)$$

Equation 34

$$I(2) = (\beta I_{spon})\left(\frac{e^{(G-\alpha_i)L} - 1}{G-\alpha_i}\right)e^{(-A-\alpha_i)L}$$

Equation 35

In Equation 35 *A* is the modal absorption in the un-pumped front section. Examples of typical ASE can be seen in Figure 10.

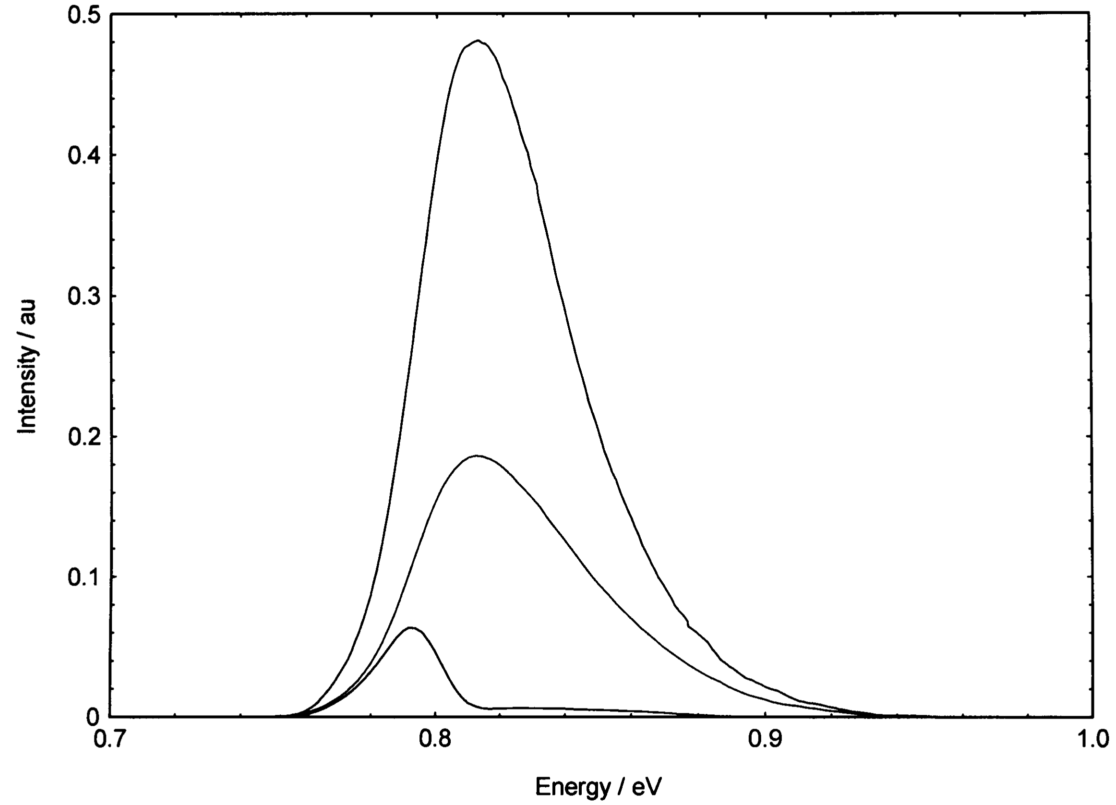

Figure 10. Example ASE showing intensity measured from the facet of a device. Blue is when both sections 1 and 2 are being pumped, red is when just section 1 (the front section) is being pumped and black is when just section 2 (the back section) is being pumped.

Having now defined the ASE at the edge of the device when different lengths are being pumped / not pumped, it is now possible to determine the modal gain and the modal absorption.

To get the net modal gain Equation 34 is divided by Equation 33 which gives Equation 36

$$G-\alpha_i=\frac{1}{L}\ln\left(\frac{I(1+2)}{I(1)}\right)$$

Equation 36, the equation for modal gain

Similarly to obtain the equation for net modal absorption Equation 33 is divided by Equation 35 which gives Equation 37

$$(A+\alpha_i)=\frac{1}{L}\ln\left(\frac{I(1)}{I(2)}\right)$$

Equation 37, the equation for modal absorption

To use Equation 36 and Equation 37 the following conditions must be met: the lengths of the two sections must be the same, the light that is measured must be dominated by light that has been coupled into the waveguide (light from large far-field angles is spatially filtered out); and no round trip gain can take place.

Examples of the modal gain and absorption obtained from ASE using the above equations can be seen in Figure 11

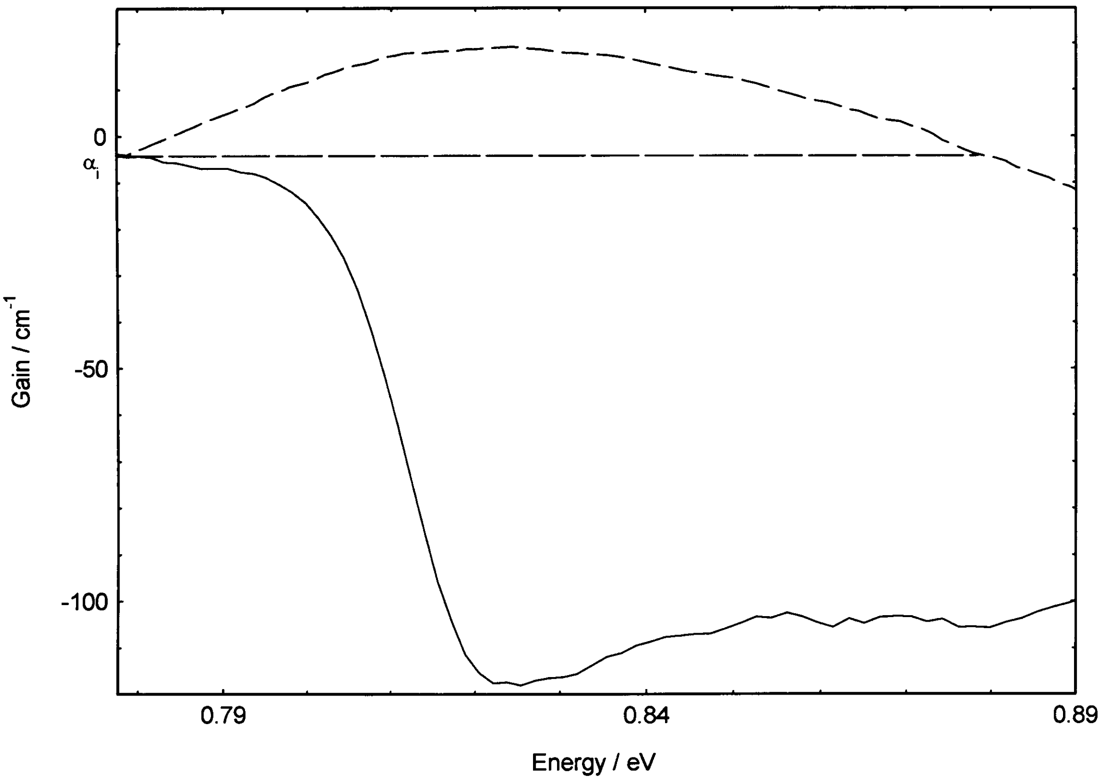

Figure 11, example of the modal gain (blue) and absorption (red) spectrum as a function of photon energy.

The internal optical loss (α_i) is found from the low energy region where the gain and absorption spectra meet, in this region there is no gain or absorption so the loss of intensity here is down to scattering losses (internal optical loss).

This value of α_i can then be added to each of the spectra turning them into modal gain and absorption.

The SCM can also be used to find the unamplified spontaneous emission by substituting Equation 36 into Equation 33 which will include a β term, and collection geometry must also be considered now. When working out the gain and the loss the light collection efficiencies cancel with each other as it is the same for *I(1)*, *I(2)* and *I(1+2)* however, when working out the spontaneous emission they do not cancel. So now the relationship between the measured ASE *I(L)* which is in arbitrary units and the actual ASE $I_{act}(L)$ which has units $s^{-1}cm^{-1}eV^{-1}$ needs to be taken into account. These are related by Equation 38

$$I(L) = C(1-R)I_{act}(L)$$

Equation 38

where *R* is the reflectivity of the air semiconductor interface and *C* is an extraction factor which takes into account the collection geometry of the measurement system.

Re-arranging Equation 33 for βI_{spon} and substituting in Equation 36 and Equation 38 gives

$$\beta I_{spon} = \frac{1}{C(1-R)} \times \left[\frac{I(1)^2}{I(1+2)-2I(1)} \times \frac{1}{L} \ln\left(\frac{I(1+2)}{I(1)} - 1 \right) \right] = \frac{1}{C(1-R)} I_{spon}^{meas}$$

Equation 39

The term on the right hand side of Equation 39 in the square bracket is the measured spontaneous emission or I_{spon}^{meas}. It is therefore possible to plot I_{spon}^{meas} as a function of photon energy as everything contained within it is known from the ASE measurements. An example plot of this un-amplified spontaneous emission is shown in Figure 12

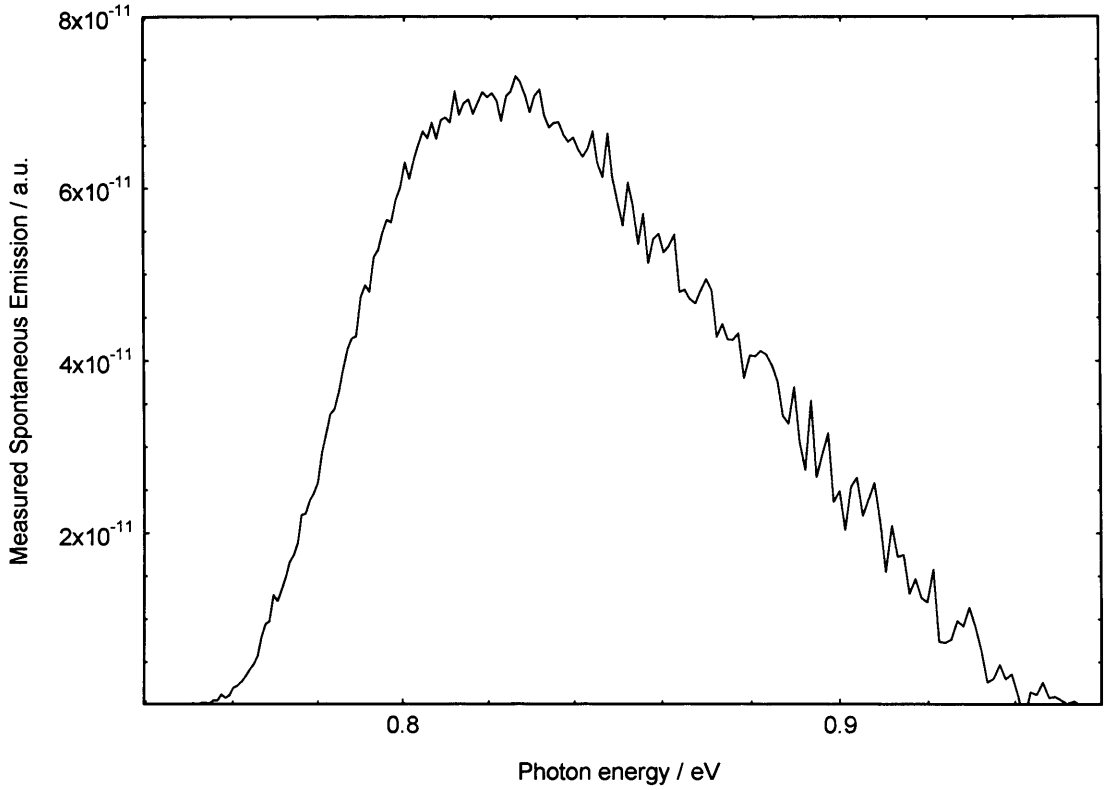

Figure 12. Un-amplified spontaneous emission (in arbitrary units) as a function of photon energy.

Using the SCM it is possible to calibrate this un-amplified spontaneous emission to get it in real units. This is done using the population inversion factor, the equation for which was given in chapter 2 but is repeated here in Equation 40

$$P_f(hv) = \frac{f_1 - f_2}{f_1(1-f_2)} = \frac{G^p(hv)}{I_{spon}(hv)} \times \frac{n^2(hv)^2}{3\pi^2\hbar^3c^2} \times \omega_{\text{mod}}$$

Equation 40

In Equation 40 there is an I_{spon} term, to turn this into I_{spon}^{meas} an overall calibration factor C′ is used and from Equation 39 this is defined as Equation 41

$$C' = \beta C(1-R)$$

Equation 41

Equation 40 now becomes Equation 42

$$P_f(h\nu) = C'\frac{G^p(h\nu)}{I_{spon}^{meas}(h\nu)} \times \frac{n^2(h\nu)^2}{3\pi^2\hbar^3c^2} \times \omega_{\text{mod}}$$

Equation 42

This now only has measured quantities in it, an example of a P_f as a function of photon energy can be seen in Figure 13

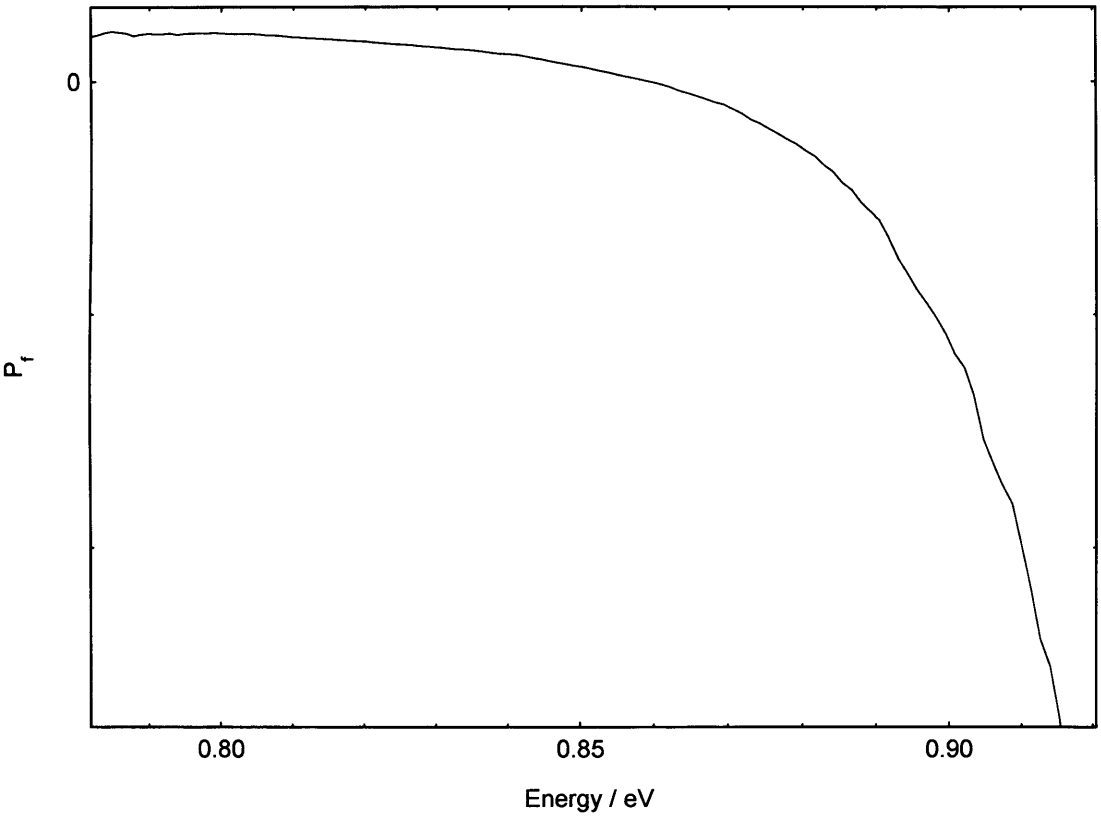

Figure 13. Population inversion factor (P_f) as a function of photon energy

Equation 40 shows that when either $f_1 = 1$ or when $f_2 = 0$ then $P_f = 1$. So a region on the plot of experimentally obtained P_f where saturation has occurred is found and the value of experimental P_f at this region is recorded, This value equals $\frac{P_f}{C'}$, and knowing that $P_f = 1$, C′ can be found. Using this calibration factor the un-amplified spontaneous emission can be converted into real units. This is done by multiplying the measured spontaneous emission by $\frac{1}{C'}$ as is suggested by Equation 39 and Equation 41. This spontaneous emission has now been calibrated by one polarisation mode (because in chapter 2 the mode density in only one polarisation is used when defining spontaneous emission, so the ASE is always measured after passing through a polariser). Integrating this calibrated spontaneous emission and multiplying by the electronic charge e will give the radiative current for that mode. The contribution from the second TE mode to the total radiative current is assumed to be the same as the measured mode. The contribution from the TM mode to the total radiative current is found experimentally by repeating the procedure described above with a polariser set to TM (instead of TE as was the case before) and then finding the appropriate calibration factor.

Once the radiative current is known it can be subtracted from the applied current to give the non-radiative current.

Having described the theory behind the segmented contact technique I will now detail the device requirements and experimental set up needed in order to successfully perform the experiment.

3.5 Device Checks

Before using a device with the SCM some preliminary checks are made on the devices.

The first check is a visual inspection of the facets before attaching the wires. It is important that the facet at the front of the device (the section marked 1 in Figure 9) is mirror like and that no imperfections can be seen, any imperfections could scatter the light.

Having visually checked the facets and attached the wires to the device the next check made is to look at the current voltage (IV) characteristics. It is important that the two sections (marked 1 and 2 in Figure 9) have identical IVs. Any difference between them could indicate the presence of extra current paths within the device or a difference in resistance which implies that the two sections are not identical. As well as the IVs being the same the shape is looked at to make sure that there are no unexpected features, such as sudden jumps or plateau regions. The IV measurements, as with all the measurements performed in this thesis (including the SCM itself), are performed pulsed, with a pulse width of 500ns and a repetition rate of 5kHz, this gives a duty cycle of 0.25%. The measurements are performed pulsed so as to remove the risk of internal heating. No differences in peak gain or IV characteristics were observed between this duty cycle and lower ones. An example set of IVs taken on structures used later in this thesis are shown in Figure 14.

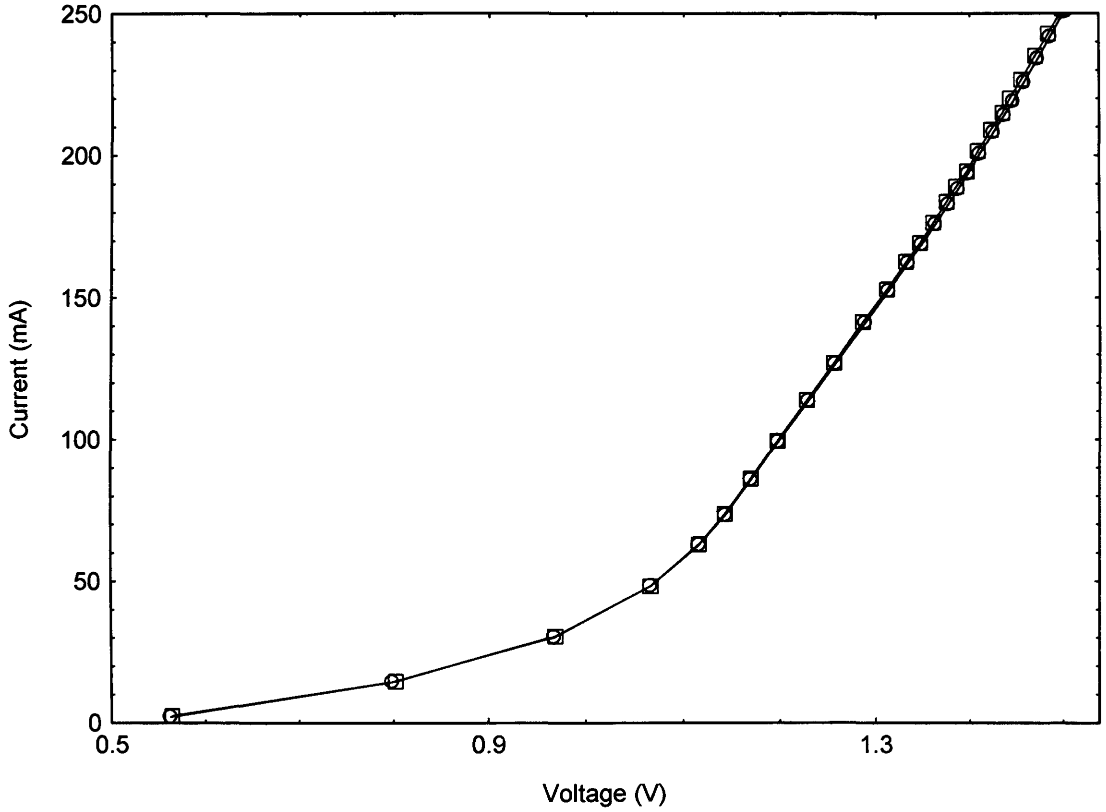

Figure 14. Example of IV traces for section one (blue line) and section two (red line).

For a given voltage a difference in current between sections of up to 5% is acceptable as it does not affect the results of the SCM, I tested devices to establish this.

It is also important to check that the isolation between sections is sufficiently high; if it is very low, then the current will "spread" from one section to the other; if it is very high, it could imply that the etching of the contact break has gone too deep, which could affect the optical mode. Typical inter-contact resistances are between 100Ω-500Ω.

The final device check before being used in the SCM is to look at the near field emission. The near field measurement is performed pulsed with a duty cycle of 0.25%. The near field emission is looked at when just section one is being driven, then when just section two is being driven and finally when both sections are being driven. The shape, width and position of the near fields should be the same in all three cases; if this is the case then the emission can be compared when the three different combinations of pumping are being used, (all three are needed for the SCM). The near fields are also used to make sure that no signs of filamentation are present, this would make the near field emission appear non-uniform.

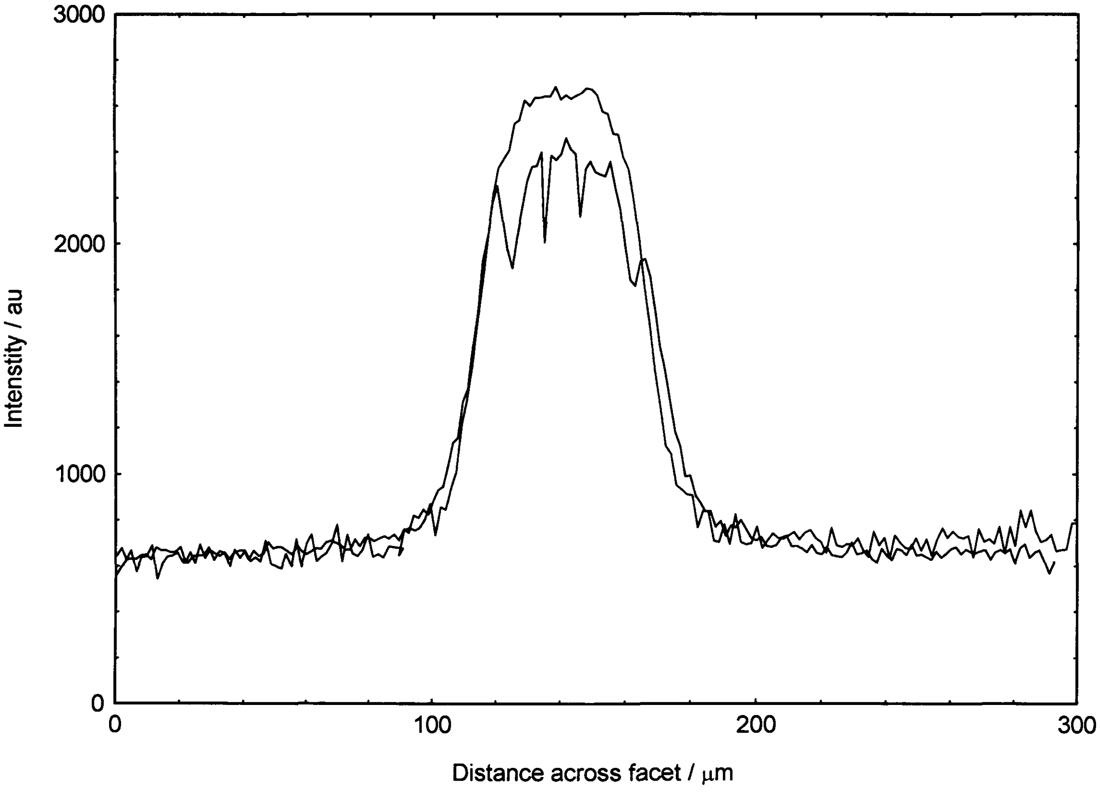

Figure 15. Shows the measured intensity of two near fields as a function of distance across the facet. The blue line shows a uniform (good) near field emission, the black line shows a non-uniform (bad) near field emission.

As well being used to inspect the quality of the near field emission, the near fields are also used to quantify the current spreading below the oxide stripe, this is taken as the full width half maximum (FWHM) of the profile. The current spreading in the "good" near field in Figure 15 is 54µm, this means that current has spread out by 4µm below the stripe.

Once all these checks have been satisfied the device can be used in the SCM.

3.4 Segmented Contact Method Experimental Set Up

Almost all the measurements presented in this thesis have been taken on a test kit that was initially set up by Dr Craig Walker and Dr Ian Sandall, and subsequent improvements to the code the kit uses have been made by me.

A diagram of the experimental set up can be seen in Figure 16.

The segmented contact device as shown in Figure 9 is put into a cryostat, which means that the measurement can be performed at a constant temperature and also allows this temperature to be varied. The cryostat used on this setup is a Joule Thomson cryostat which works by expanding nitrogen gas and can be used to obtain temperatures in the range 80K-400K.

The SCM requires ASE to be measured when either both the front sections are being driven or when just one of them is being driven. This means that the kit must be able to independently supply a pulsed current to each section; this is achieved by having a separate pulse generator (current source) for each section. The pulse generators are computer controlled, meaning that the kit can measure the ASE over a wide range of currents autonomously.

For the SCM the ASE also needs to be measured as a function of wavelength (or photon energy) and to allow this to be done the light passes through a monochromator and is then detected by a photomultiplier tube (PMT) which is connected to a boxcar which takes the pulsed signal and converts it to an averaged voltage which is then recorded by a computer. The monochromator is also connected to the computer which then steps through a wavelength range (step size and range can be varied) and the emission at each wavelength is recorded (the computer "waits" at each wavelength before taking a reading for approximately 1 second). Before the light reaches the monochromator it passes through a lens which focuses the light onto the monochromator entrance slit, it also passes through a polariser which allows either TE or TM emission to be measured (TE and TM are defined with respect to the device, this convention is true for the entire thesis as shown in figure 5 in chapter 2).

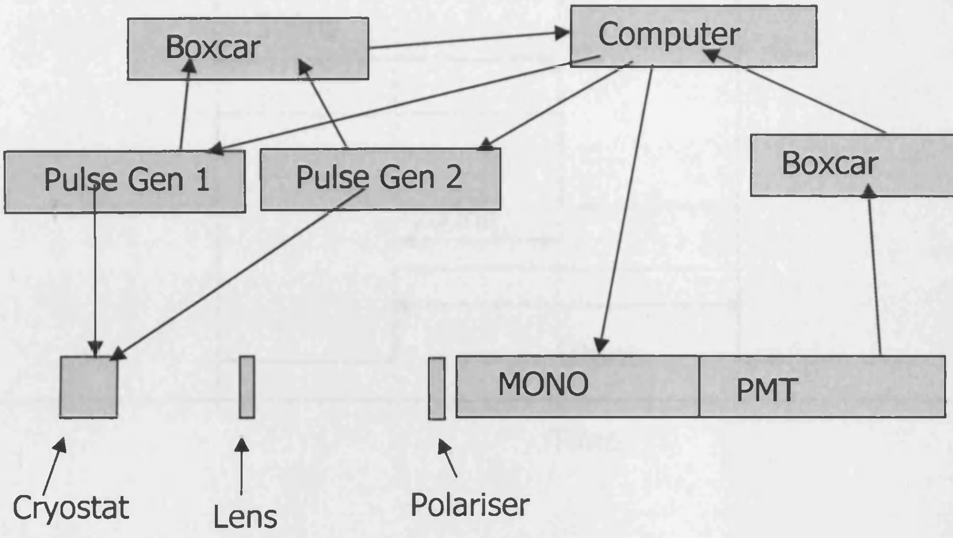

Figure 16. Schematic diagram of experimental set up: Lines indicate a connection between apparatus, direction of arrows indicates the direction of information/control.

The current pulses that drive the two sections are arranged so that they overlap for a period, this means that during a single pulse period all three of the pumping combinations occur (section 1 alone, section 2 alone and 1+2 together), as is shown in Figure 17. The position of the boxcar "gates" (where the boxcar reads the value of the light output) defines if a gain or loss measurement is taken. The light boxcar on the kit has three gates, one of these is always placed before the pulses to record the zero light level, another is always placed so as to record the emission from just the front section (the region marked 2 on Figure 17). The final gate is either in the region marked 1+2, which means a gain measurement is taken, or placed in the region marked 1 which means a loss measurement is taken. The positioning of this gate is done manually before the start of each measurement or set of measurements. To record an entire gain or loss measurement typically takes between 20-40min, depending on accuracy and wavelength range.

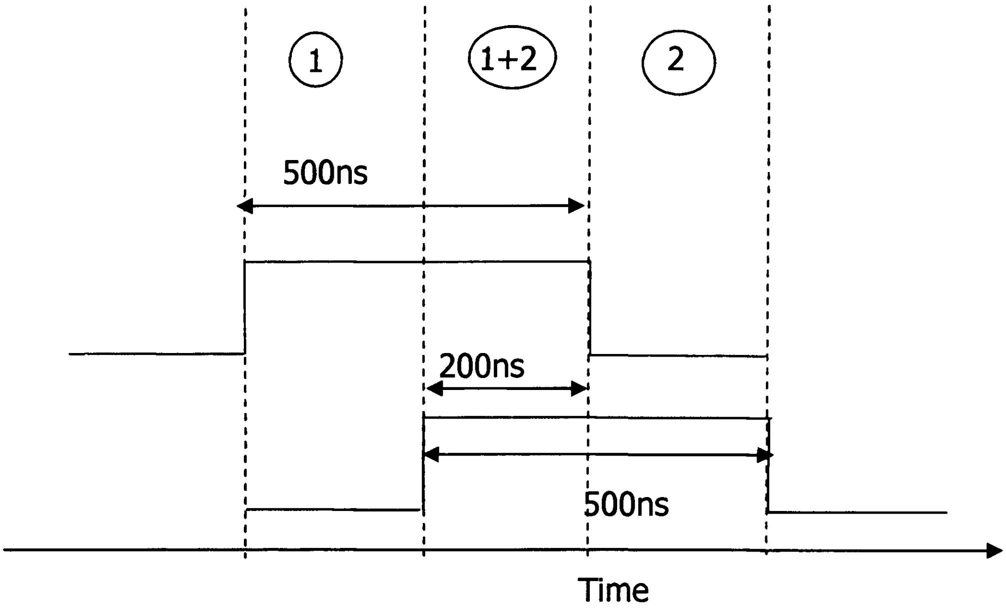

Figure 17. Pulse set up for SCM measurement. The red line is the current going to the back section the blue to the front section

3.6 Summary

In this chapter I have outlined how by using the SCM, it is possible to measure the modal gain and loss in real units, and to determine the radiative current density and the non-radiative current density experimentally. This can be done over a range of different currents to produce gain vs current and gain vs radiative current graphs. All this can be found just using the ASE collected from two sections of equal length, electrically isolated from one another. This method and analysis is used to find all of the experimental data presented in this thesis unless otherwise stated.

3.7 References

- Blood. P, Lewis. G.M, Smowton. P.M, Summers. H, Thomson. J, Lutti. J, "Characterization of semiconductor laser gain media by the segmented contact method", IEEE Journal of Selected Topics in Quantum Electronics, vol.9, No.5, 2003
- Thomson. J.D, Summers. H.D, Hulyer. P.J, Smowton. P.M, Blood. P. "Determination of single-pass optical gain and internal loss using a multisection device", Applied Physics Letters, vol.75, no.17, 1999

4. Experimental Investigation of Differently Modulation Doped GaInNAsSb/GaNAs Lasers

4.1 Introduction

In this chapter I will describe measurements taken on GaInNAsSb/GaNAs samples emitting at 1.55μm. I will also describe some extended analysis that I performed on some supplied data. The purpose of these experiments is to try to find the source of non-radiative recombination in this material system. This is important because lasers based on this material system have recently been developed with relatively low room temperature thresholds (Gupta et al, 2006 and Bank et al, 2007) however a number of mechanisms may still be limiting performance. It is important to improve the performance of this material if it is to be a realistic competitor to the current InP devices.

4.2 Details of Material

The material used in this chapter was grown by the Gupta group in the National Research Council Institute for Microstructural Sciences in Ottawa, Canada. The samples were grown using molecular beam epitaxy (MBE) and contain two 7nm wide GaInNAsSb quantum wells within 7.5nm GaNAs barriers separated by 5nm of GaAs (to allow doping to be placed between the wells) . Three different types of samples were used; they are all nominally identical except for the inclusion of modulation doping in two of them, one with n doping, one with p doping and one un-doped. The dopants were contained within GaAs layers that surrounded each well. See Figure 18 for a schematic diagram. The doping level in the GaAs is $8.35 \times 10^{17} cm^{-3}$, which assuming all the dopants reach the well corresponds to a density in the well of $2.5 \times 10^{11} cm^{-2}$. The double quantum well active region was grown at the low temperature of 420°C, the long growth of the top cladding layer at 600°C provides in-situ annealing of the active region, no ex-situ annealing was required. Details of growth of similar samples is reported in (Gupta 2007).

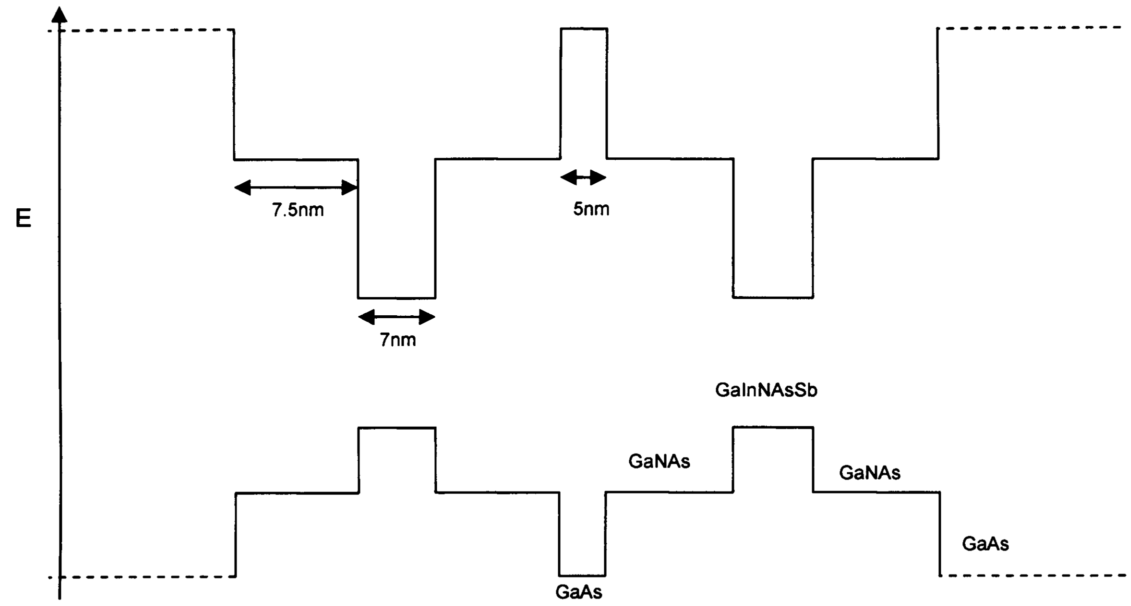

Figure 18. A schematic energy diagram of the structures used. The modulation doping is contained within the central 3nm of the 5nm of GaAs between the wells and in 1.5nm of GaAs located 1nm away from the GaNAs.

The purpose of including the modulation doping is to shift the Fermi level positions as shown in Figure 19. In other material systems the inclusion of p-doping has been shown to be beneficial to the laser performance (Sandall et al, 2006. Smowton et al, 2007)

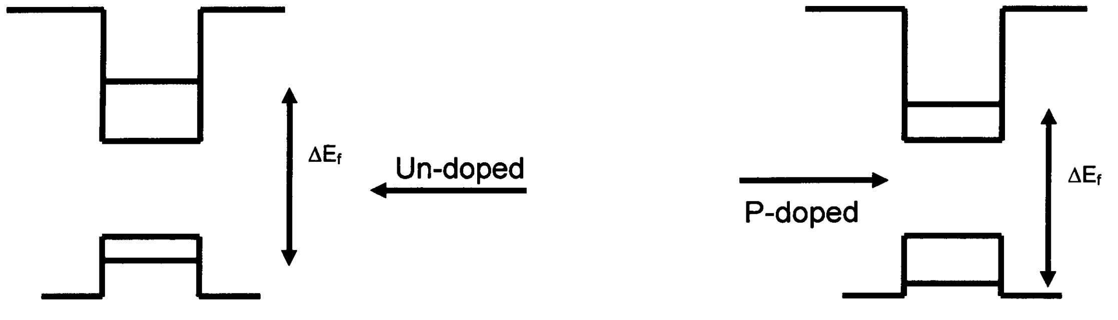

Figure 19. The expected effect of including p doping

Shifting the relative positions of the Fermi-levels should change the balance of contributions from the carrier loss processes making them easier to identify. Another effect that the inclusion of doping might have is to effect the carrier transport. This is because the dopants will introduce a charge to the GaAs region which will shift the band offset of the GaAs region with respect to the well and barriers. Introducing p doping will increase the conduction band offset and reduce the valence band offset.

4.3 Extended analysis of supplied data

As well as being sent pieces of wafers of material by the Gupta group, they sent some threshold current results that had been performed on shallow etched ridge lasers that had been fabricated from another part of the wafer. These are shown in Figure 20. Shallow etched ridges are etched down to or slightly above the active region.

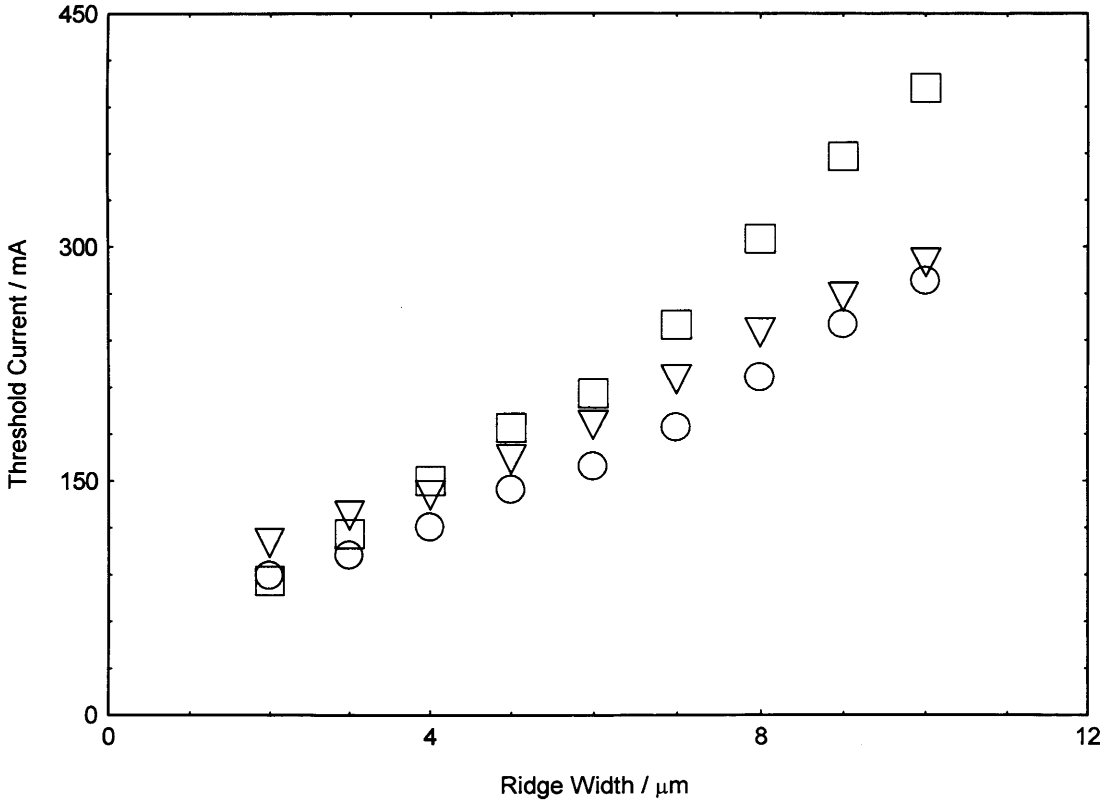

Figure 20. Threshold current as a function of ridge width for GaInNAsSb/GaNAs samples. Red are p-doped samples, blue are n-doped and black un-doped. (provided by the Gupta group)

The lasers used to produce Figure 20 were of lengths 1189μm for the un-doped material, 1203μm for the n-doped and 1204μm for the p-doped, and to remove the effect of the lengths and widths being different it is necessary to turn the currents into current densities. Figure 21 shows the current densities as a function of ridge width, the error bars shown are due to the uncertainty in the ridge widths (discussed later) which are used to calculate the threshold current densities.

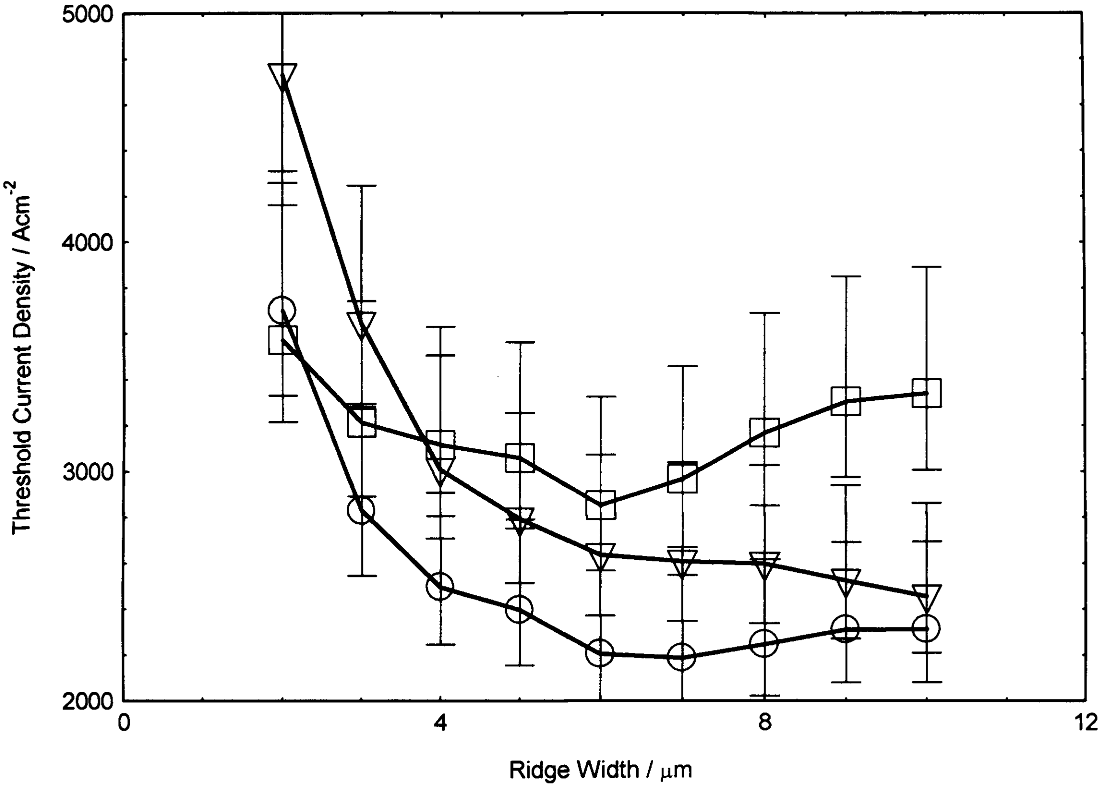

Figure 21. Current density as a function of ridge width for GaInNAsSb/GaNAs samples. Red points are p-doped samples, blue are n-doped and black are un-doped.

Figure 21 shows that in all three of the material types there is an increase in current density when moving towards smaller ridge widths, in the case of the p-doped sample there is also evidence of an increase when moving towards larger ridge widths with a minimum in the curve at around 6µm. The observed increase in threshold with decreasing ridge width is consistent with what would be expected (Naidu, 2010). From (Naidu, 2010) this increase will be due to one or more of the following:

- lateral leakage of carriers from the ridge to the surrounding material which would become fractionally more prominent at smaller ridge widths,

- an increase in the internal optical loss due to scattering on the side walls, meaning that more gain is needed to overcome the internal losses at reduced ridge widths,
- a deteriorating gain lateral mode overlap because the optical mode starts to expand beyond the gain medium.

Using Figure 20 it is possible to estimate the contribution that leakage (current spreading out from below the ridge) will make to the threshold currents of the devices. If we assume that the current is the same for each ridge width then by fitting a straight line to the data and then extrapolating back to a zero ridge width the intercept will be the leakage component. This current can then be removed and a graph of current density minus leakage as a function of width can be produced.

The data shown in Figure 20 do not appear to follow a simple linear dependence; instead they can be represented by two straight line regions with a change from one gradient to another at a ridge width of approximately 6-7µm for all three of the structures. Thus the leakage current was taken from lines fitted to the first 5 data points of each data set. The fitted lines used to find the leakage current are shown in Figure 22, lines fitted to the larger ridge widths are also shown.

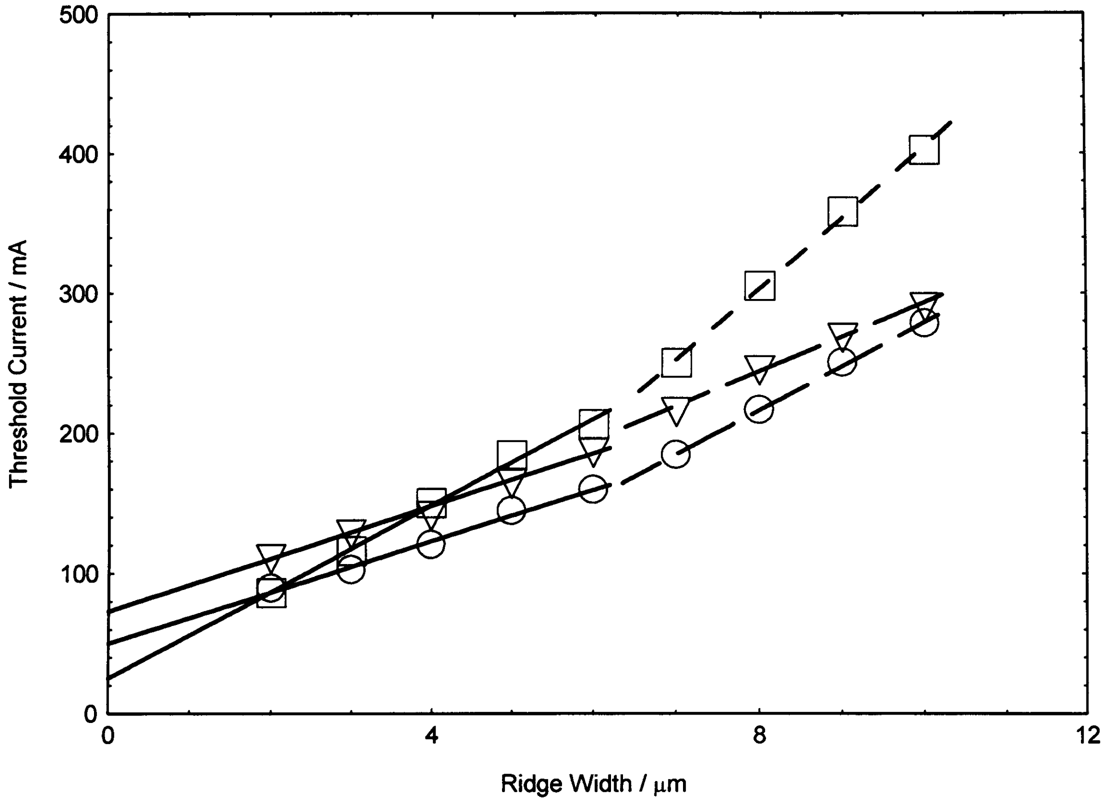

Figure 22. Threshold current as a function of ridge width for GaInNAsSb/GaNAs samples. Red are p-doped samples, blue are n-doped and black un-doped. Solid lines were used to find leakage current, dashed lines are fitted the higher ridge width data.

The leakage currents found from Figure 22 are shown in Table 1

Sample	Leakage Current / mA
P-doped	25
N-doped	50
Un-doped	75

Table 1. The leakage current in each of the three differently doped GaInNAsSb/GaNAs samples.

Table 1 shows that the p-doped sample has a far smaller contribution due to leakage in comparison to either the n or un-doped samples and that the un-doped samples have the highest contribution. The inclusion of doping is not expected to have affected the leakage current.

The depth that the ridges are etched to will have an effect on the leakage current, the deeper the ridge the lower the leakage current you would expect. The ridge depths were found by looking at SEM pictures: Figure 23 (un-doped), Figure 24 (n-doped) and Figure 25 (p-doped), (taken from private communication with Gupta group). All three of the ridges in these figures are nominally 2µm wide. In Figure 25 the etching has gone down to the level of the quantum wells in the trench region (the region immediately to the left of the ridge). The red lines represent where I measured the widths of the ridges.

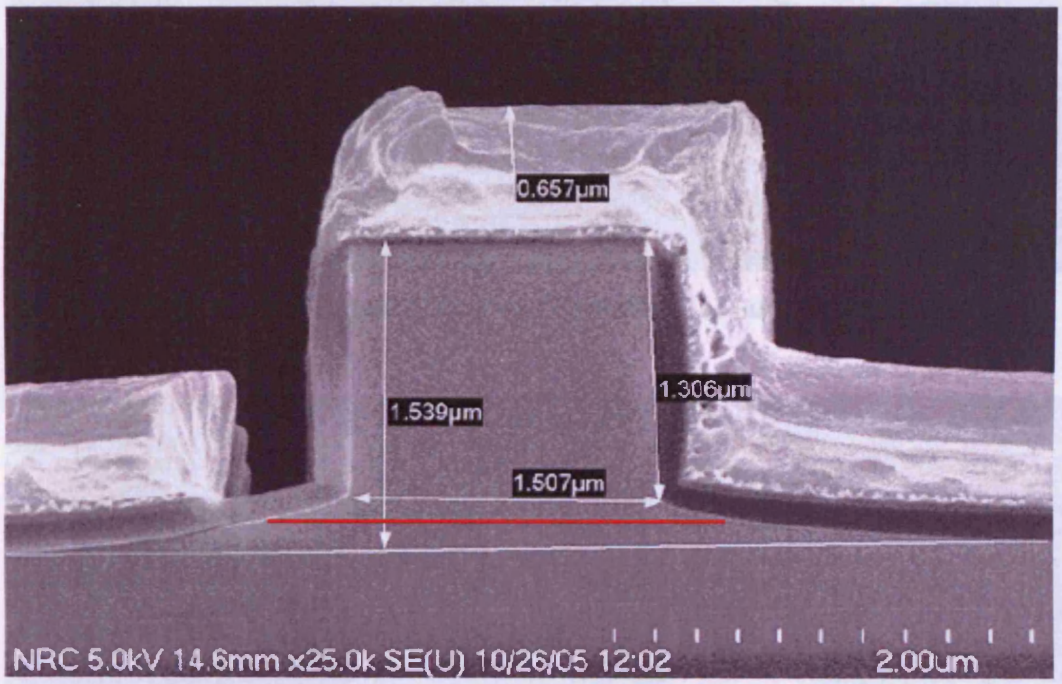

Figure 23. SEM picture of an un-doped ridge laser. (provided by Gupta group)

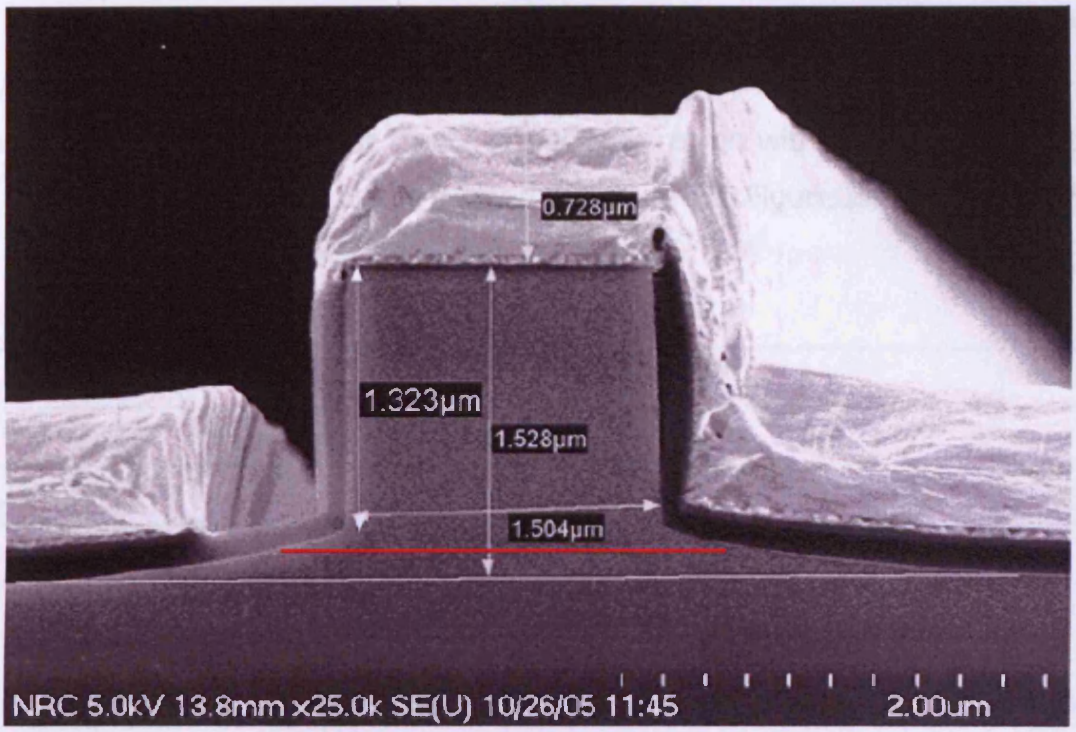

Figure 24. SEM of an n-doped ridge laser (provided by Gupta group)

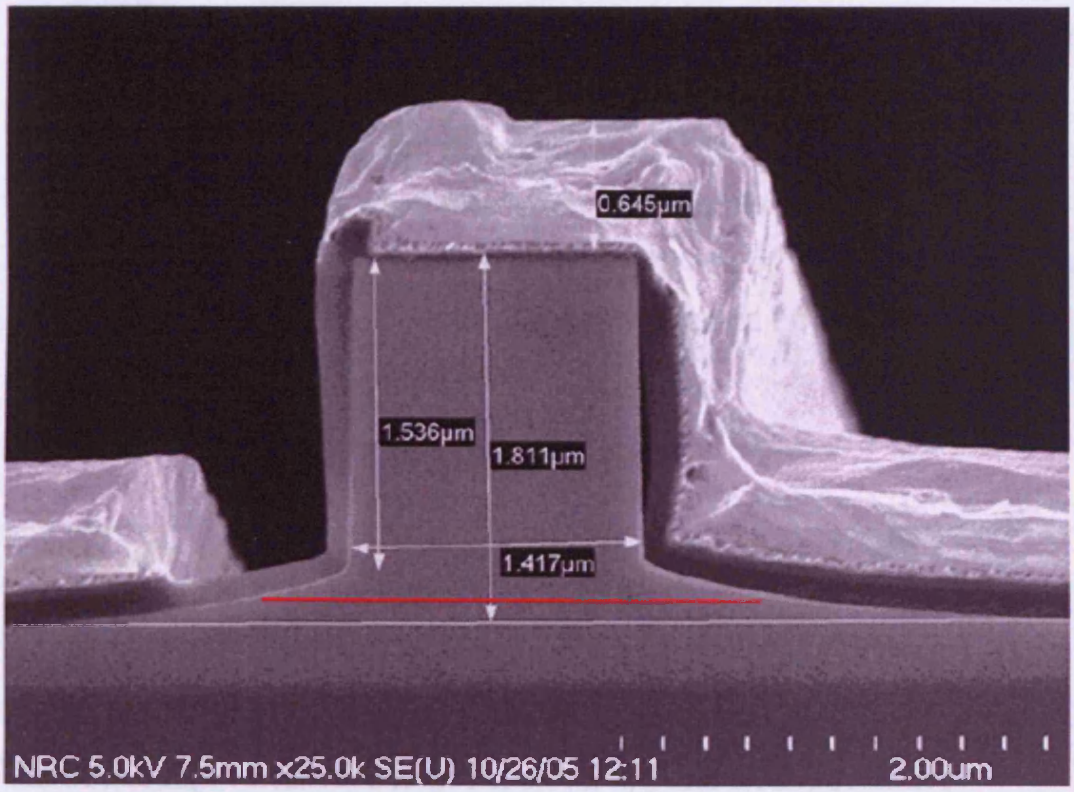

Figure 25. SEM of a p-doped ridge laser. (Provided by Gupta group)

Figure 23, Figure 24 and Figure 25 show that there is variation in the width of the ridges, I have taken the width from how wide the material is at the depth of the bottom of the trench region (the region without a contact on it to the left of the ridge) this is marked on Figure 23, Figure 24 and Figure 25 by a red line. The widths are shown in Table 2

Sample	Width / μm
Un-doped	2.20
N-doped	2.16
P-doped	2.39

Table 2. The widths of the three differently doped GaInNAsSb/GaNAs ridges.

This variation in ridge width from the expected 2μm is taken account of with the inclusion of error bars in Figure 22 and Figure 26. The reason for not simply adjusting the ridge widths to the actual measured widths from the SEM images is firstly because the variation in ridge width may not be exactly the same for all ridges with nominally the same ridge width and also SEM data was only supplied for the 2μm ridges.

Table 3 shows the ridge depths as taken from the above SEM images, the depths are taken from the distance between the top of the ridge and the top of the trench region. These depths are clearly marked on the figures. Also shown is the leakage data from Table 1.

Sample	Leakage Current / mA	Ridge Depth / μm
P-doped	25	1.536
N-doped	50	1.323
Un-doped	75	1.306

Table 3.Leakage current and ridge depths for n, p and un-doped devices

Table 3 shows that there is a clear trend between ridge depth and leakage current as would be expected. The inclusion of doping in the active region should have no effect on the leakage current.

Figure 26 shows the threshold current density once the leakage current from Table 3 has been removed. The error bars are due to the variation in ridge width from the expected ridge.

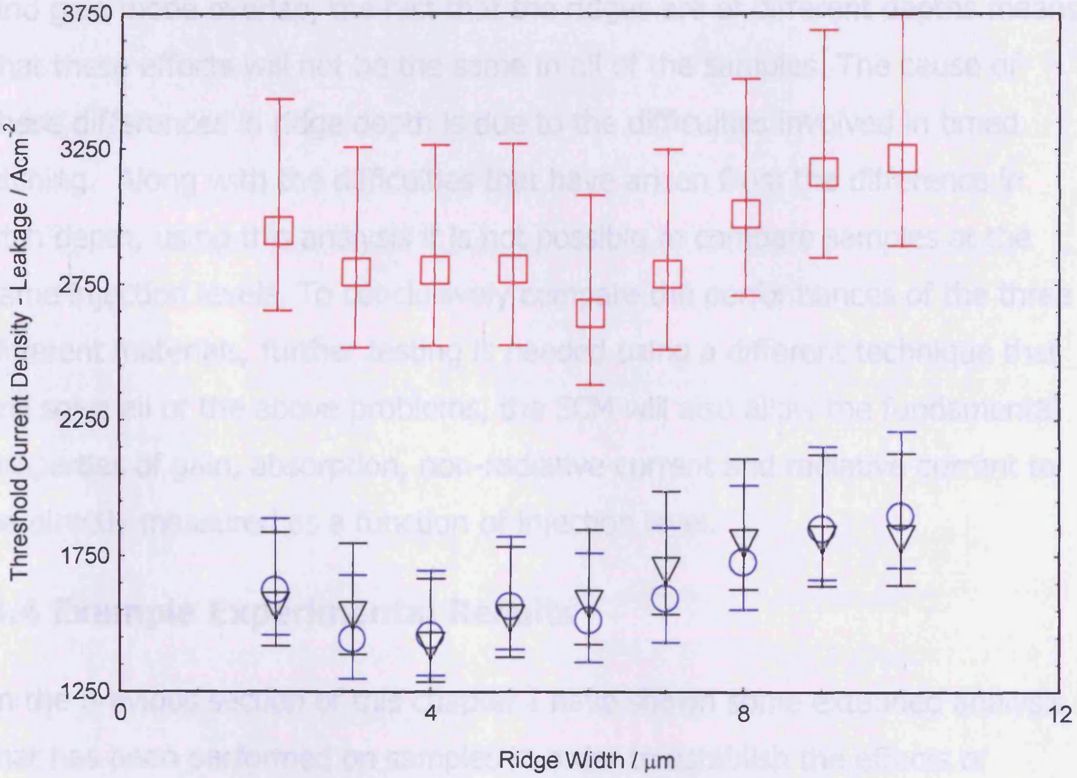

Figure 26. Shows the current density minus leakage current for GaInNAsSb/GaNAs samples. Red points are p-doped samples, blue are n-doped and black are un-doped.

Figure 26 shows that once the effect of leakage has been removed, the p-doped samples require a higher current density to achieve lasing in comparison to the n and un-doped samples. Still present in the data is an upturn in the threshold when going to smaller ridge widths although this is now far less pronounced than was the case in Figure 21, particularly in the case of the n and un-doped samples. What is still clear is a rise in threshold with ridges larger than 6-7μm, this is not expected as the effects mentioned earlier in this chapter should all be reduced with increasing ridge width. Although given how the leakage current was found and removed it was clear that this trend at larger ridge widths would remain.

By analysing this data it has been possible to show that the p-doped material requires larger threshold currents in comparison to both the un and n-doped samples which are comparable to each other. Having removed the effect of leakage there is still the problem of changing α_i (the internal waveguide loss) and gain mode overlap, the fact that the ridges are of different depths means that these effects will not be the same in all of the samples. The cause of these differences in ridge depth is due to the difficulties involved in timed etching. Along with the difficulties that have arisen from the difference in etch depth, using this analysis it is not possible to compare samples at the same injection levels. To conclusively compare the performances of the three different materials, further testing is needed using a different technique that will solve all of the above problems, the SCM will also allow the fundamental properties of gain, absorption, non-radiative current and radiative current to be directly measured as a function of injection level.

4.4 Example Experimental Results

In the previous section of this chapter I have shown some extended analysis that has been performed on samples in order to establish the effects of differently doping the GaInNAsSb material. I have also however highlighted the limitations of this approach. In the rest of this chapter I will describe measurements that I made on some segmented contact devices (fabricated in-house in Cardiff by technical staff) using the segmented contact method as has been described in detail in Chapter 3. The material used to fabricate these devices is the same as was described in 4.2.

Figure 27 shows the 300K TE gain spectra for the un-doped sample, it also shows an absorption spectrum.

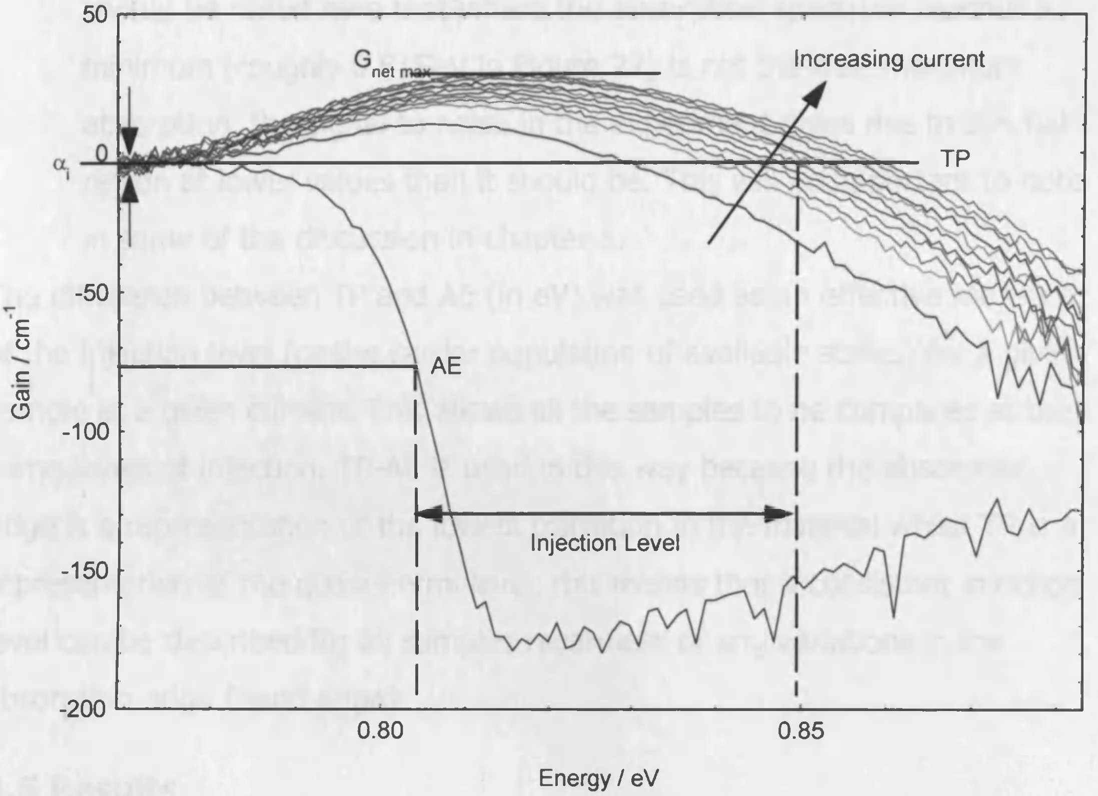

Figure 27. Modal gain curves and an absorption curve as a function of energy for the un-doped sample at 300K

Shown on Figure 27 are a number of quantities that will be used in the analysis later in this chapter and extensively in subsequent chapters;

- $G_{net\ max}$ is the maximum net modal gain achieved for a given current
- α_i is the internal optical loss, it is taken at the point where the gain and absorption curves meet and flatten on the low energy side.
- TP is the transparency point measured in eV, this corresponds to the quasi-Fermi level separation if the system is in thermal equilibrium and so can be described by Fermi statistics. This is the point on the gain graph on the higher energy side where gain equals the internal optical losses
- AE refers to the absorption edge, this is used to give a measure of the effective band gap of the material (lowest transition), this was taken at a value of -75cm^{-1} on the absorption curve, after α_i had been added, (i.e. -75cm^{-1} – α_i). This value was chosen as it was the half height of the absorption spectrum of the sample with the smallest half height. It

should be noted here that where the absorption spectrum reaches a minimum (roughly 0.815eV in Figure 27) is not the true maximum absorption, the signal to noise in the experiment gives rise to this flat region at lower values than it should be. This will be important to note in some of the discussion in chapter 5.

The difference between TP and AE (in eV) was used as an effective measure of the injection level (or the carrier population of available states) for a given sample at a given current. This allows all the samples to be compared at the same levels of injection. TP-AE is used in this way because the absorption edge is a representation of the lowest transition in the material whilst TP is a representation of the quasi-Fermi level, this means that a consistent injection level can be described for all samples regardless of any variations in the absorption edge (band edge).

4.5 Results

All the data shown is taken at 300K and with a polariser in place set to TE. No TM gain is observed when the polariser in place is set to TM. Before comparing the non-radiative currents from the three different samples it is important to make sure that the samples are the same, other than the presence of doping. The first check to make was to see if, for a given injection level, the samples were producing the same amount of gain. Gain as a function of TP-AE is shown in Figure 28.

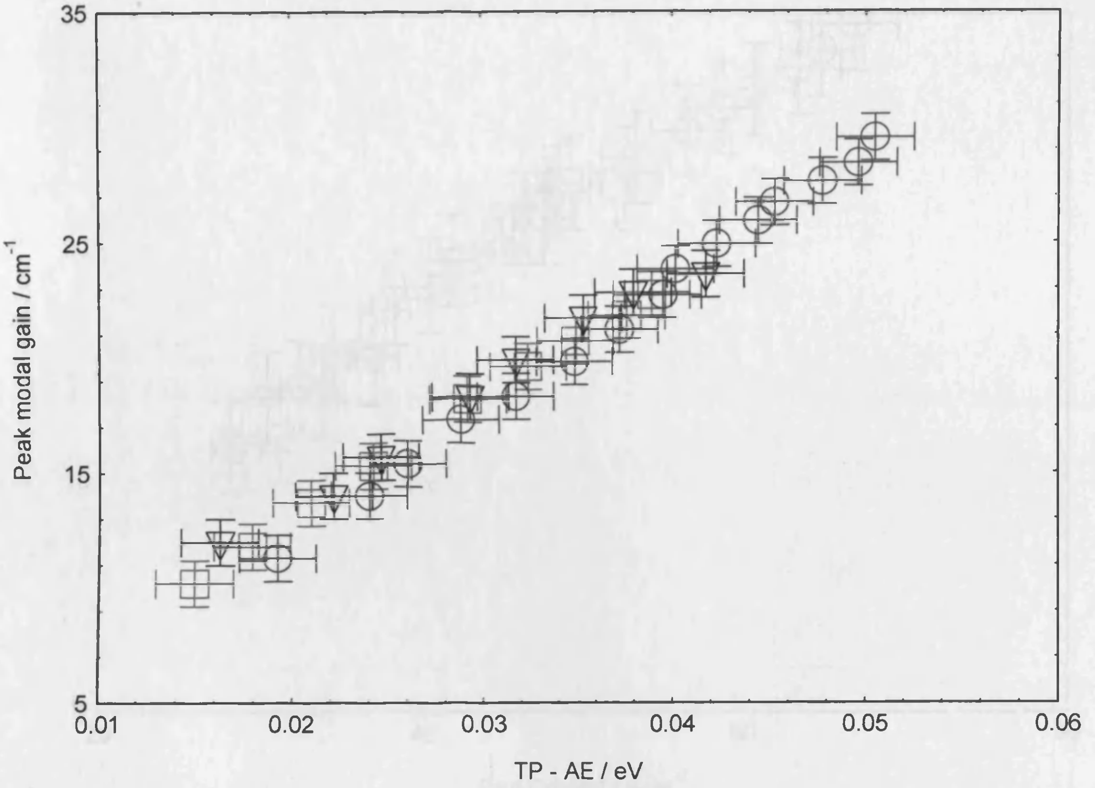

Figure 28. Modal Gain as a function of transparency point minus absorption edge for the GaInNAsSb/GaNAs samples. Red points are p-doped, blue are n-doped and black are un-doped.

Figure 28 shows that which would be expected for wells that are of made from the same material; the gain achieved from a given TP-AE is the same. Another check that was made was that the relationship between gain and radiative current was the same for all the samples. Figure 29 shows the peak modal gain as a function of radiative current. The radiative current is found by integrating the calibrated spontaneous emission, as described in chapter 3. Therefore we can plot the peak modal gain as a function of radiative current – as presented in Figure 29

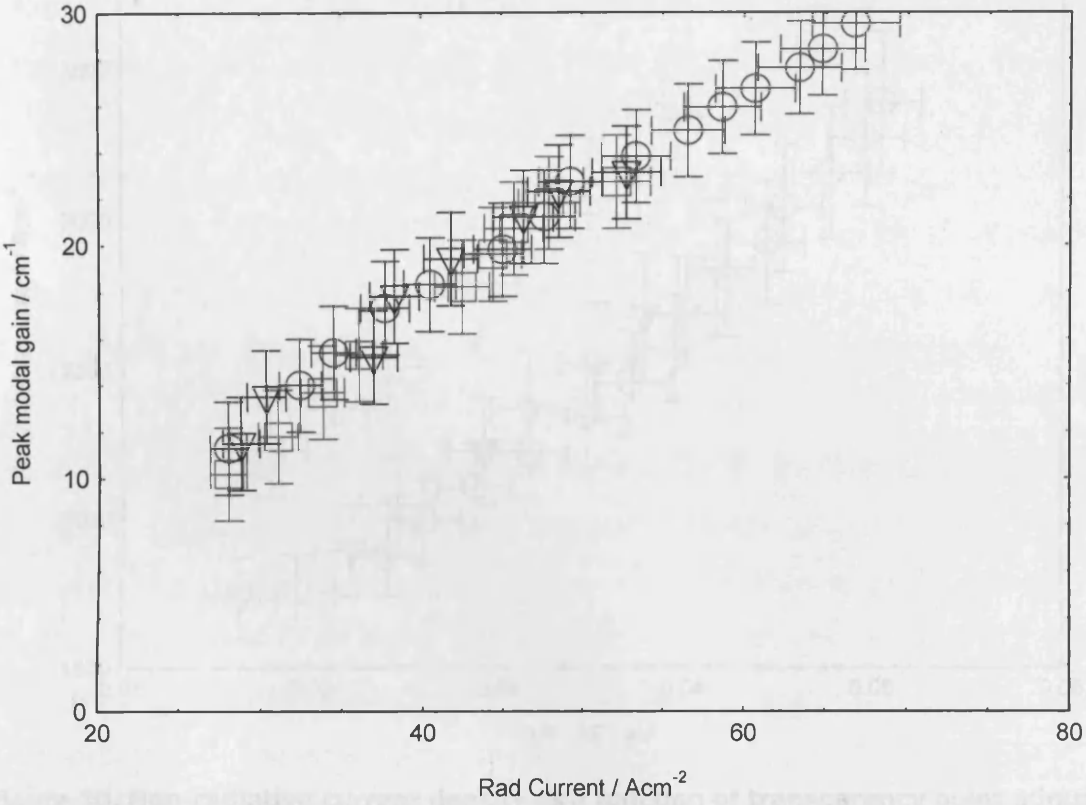

Figure 29. Peak modal gain as a function of radiative current for the GaInNAsSb/GaNAs samples. Red points are the p-doped, blue are the n-doped and black are the un-doped samples.

Figure 29 shows that at a fixed value of peak modal gain all the samples are producing the same amount of radiative current.

In Figure 30 the non-radiative current density is plotted as a function of transparency point minus absorption edge. The non-radiative current density is obtained by removing the radiative current density from the total applied current, as was discussed in chapter 3.

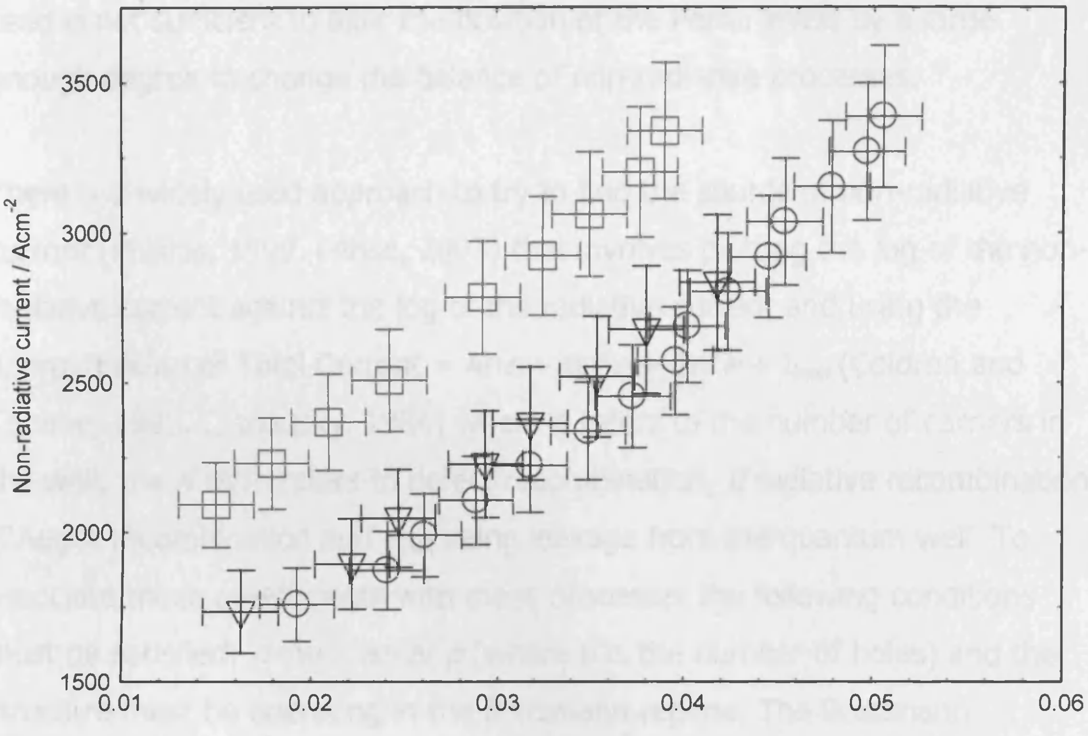

Figure 30. Non-radiative current density as a function of transparency point minus absorption edge. Red points are p-doped, blue are n-doped and black are un-doped.

Figure 30 shows that the non-radiative current density is higher for a given TP-AE in the p-doped sample, whilst the un-doped and n-doped non-radiative current densities do not show a significant difference. This shows that for a given level of pumping there is a faster non-radiative recombination rate in the p-doped sample. The rate of change with increasing TP-AE is similar for all three samples, this implies that the main non-radiative process is not Auger recombination as this would increase differently in the n and p doped samples. This is because the two main Auger processes either involve one hole and two electrons (n^2p) or two holes and one electron (np^2), if it were the first case then the rate of increase would be quicker for the p-doped (less electrons to start with) sample and vice-versa. It also is not purely a hole limited recombination process that is being increased, as in this case the n-doped sample should be better than the un-doped. Instead the observed difference is put down to the presence of extra defects that the p-doping has introduced. It is however possible that the amount of dopants that have been used is not sufficient to alter the position of the Fermi levels by a large enough degree to change the balance of non-radiative processes.

There is a widely used approach to try to find the source of non-radiative current (Phillips, 1999. Fehse, 2003) that involves plotting the log of the non-radiative current against the log of the radiative current and using the approximation of Total Current = $Ane + Bn^2e + Cn^3e + I_{leak}$ (Coldren and Corzine, 1995. Olshansky, 1984) where n refers to the number of carriers in the well, the A term refers to defect recombination, B radiative recombination, C Auger recombination and I_{leak} being leakage from the quantum well. To associate these co-efficients with these processes the following conditions must be satisfied: n must equal p (where p is the number of holes) and the structure must be operating in the Boltzmann regime. The Boltzmann approximation breaks down gradually so this technique can still be utilised at higher injection levels to gain an indication of the nature of the recombination processes. Removing the radiative current from the total current gives the non-radiative current. Plotting log non-radiative current means that the Bn^2 term is removed. Straight lines are then fitted to the data and, by inspection of the gradient assumptions can be made about the source of the non-radiative current. If the gradient is 0.5 then the recombination is due to Shockley-Reed-Hall (SRH) recombination, if it is 1.5 then it is due to Auger recombination. Any leakage from the well to the barrier region will have the effect of increasing the gradient. The leakage will increase the gradient because the population in the barrier will go up exponentially (with respect to increasing injection level) in comparison to the population of the well, this will lead to a higher order term in the gradient. A plot of this for all 3 samples is shown in Figure 31.

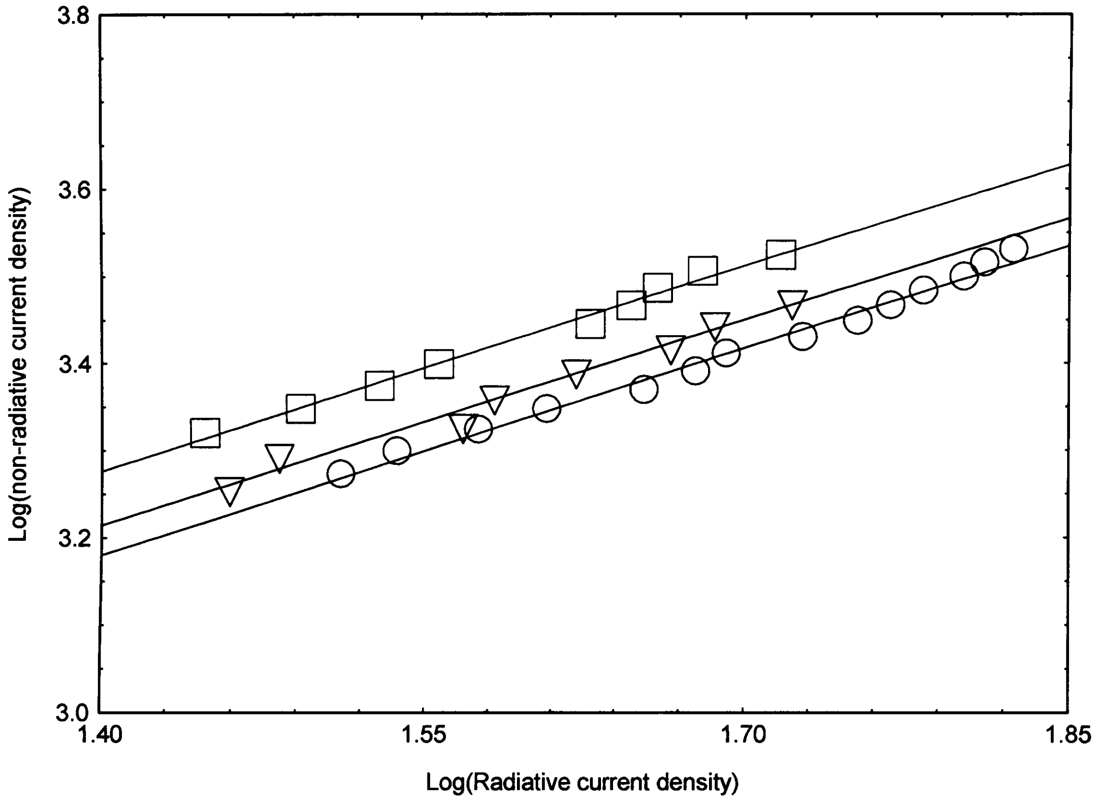

Figure 31. Log(non-radiative current density) vs log(radiative current density) for GaInNAsSb/GaNAs samples. Red points are p-doped, blue n-doped and black un-doped. Red line gradient is 0.781, black is 0.782 and blue is 0.787

Figure 31 shows that the gradients for lines fitted to all 3 of the samples are the same within error, being 0.781±0.13 for the p-doped sample, 0.782±0.13 for the un-doped and 0.787±0.13 for the n-doped. These values show that the non-radiative recombination is not due entirely to SRH in the well because the values are larger than 0.5, it also however shows that Auger recombination is not the only process as they are smaller than 1.5.
Because the p-doped samples have the same gradient it means that the higher non-radiative currents that have been observed in that sample cannot be purely due to increased defect recombination in the well; if that were the case the gradient of the red line in Figure 31 would be closer to 0.5 than the other two lines. The fact that all three lines have the same gradients also implies that Auger recombination is not a dominant process as we would then expect the gradients to be different for the differently doped/ un-doped samples. Having ruled out Auger processes being dominant the only way that

the total recombination in the p-doped sample can increase without the gradient in Figure 31 changing is for the SRH recombination in the well to increase and also recombination in the barrier to increase.

The inclusion of doping however can effect the form of the equation used for the total current used here, this applies if the background doping is larger than the carrier densities. For example if the background p doping is larger than the hole carrier density then p become p_0. The equation for total current then becomes: Total Current = $Ane + Bnp_0e + Cn^2p_0e + I_{leak}$. In this case the SRH recombination would cause the gradient of the plot shown in Figure 31 to go close to one and the Auger recombination would cause it to go to 2. This however isn't the case in our work as the estimated carrier densities are at least a power of 10 larger than the doping.

4.6 Conclusions

In this chapter I have shown that the inclusion of n-doping into GaInNAsSb does not have any significant effect either positively or negatively on the amount of non-radiative current at a given TP-AE over an un-doped device, this has been backed up with analysis I applied to laser measurements taken on shallow etched ridges. The inclusion of p-doping however has increased the non-radiative current for a given TP-AE. This observed increase in non-radiative current has been attributed to extra defects that the p-doping has introduced in both the well and the barriers, and leads to the conclusion that there is non-radiative recombination in the barriers. I have shown that Auger recombination does not appear to be a dominant non-radiative process in these wells.

4.7 References

- Bank. S.R, Bae. H, Goddard. L.L, Yuen. H.B, Wistey. M.A, Kudrawiec. R, Harris. J.S, "Recent Progress on 1.55 µm Dilute-Nitride Lasers" IEEE Journal of Quantum Electronics, 43, 9, (2007)
- Coldren. L.A and Corzine. S.W, Diode Lasers and Photonics Integrated Circuits, Wiley Series in Microwave and Optical engineering, Vol 1, Kai Chang, 1995
- Fehse. R, Adams. A.R, Sweeney. S.J, Tomic. S, Riechert. H, Ramakrishnan. A, "Carrier recombination process in MOVPE and MBE grown 1.3 µm GaInNAs edge emitting lasers" Solid State Electronics 47 (2003) 501-506
- Gupta. A, Barrios. P.J, Pakulski. G,, Aers. G.C , Caballero. J.A, Poitras. D, Wu. X, "Properties of GaInNAsSb narrow ridge waveguide laser diodes in continuous-wave operation at 1.55µm". Proceedings of SPIE – volume 6485 Novel In-Plane Semiconductor Lasers VI, Carmen Mermelstein, David P. Bour, Editors, 64850S (2007)
- Naidu. D, Smowton. P.M, Summers. H.D, "The Measured Dependence Of The Lateral Ambipolar Diffusion Length On Carrier Injection Level In S-K Quantum Dot Devices", Submitted to Journal of Applied Physics
- Olshansky. R, Su. C.B, Manning. J, Powazinik. W, "Measurement of Radiative and Nonradiative Recombination Rates in InGaAsP and AlGaAs Light Sources", IEEE Journal of Quantum Electronics, vol. QE-20, No. 8, August 1984, pp838-854
- Phillips. A.F, Sweeney. S.J, Adams. A.R, Thijs. P.J.A, " The Temperature Dependence of 1.3- and 1.5-µm Compressively Strained InGaAs(P) MQW Semiconductor Lasers" IEEE Journal of Selected Topics in Quantum Electronics, vol. 5, No.3, May/June 1999, pp401-412
- Sandall. I.C, Smowton. P.M, Walker. C.L, Badcock. T, Mowbray. D.J, Liu. H.Y and Hopkinson. M. Appl. Phys. Lett. 88, 111113 (2006)

- Smowton. P.M, Sandall. I.C, Liu. H.Y and Hopkinson. M. J. Appl. Phys. 101, 013107 (2007)

5. Experimental investigation of non-radiative processes in GaInNAsSb/GaNAs Lasers

5.1 Introduction

In the previous chapter I described an approach to trying to find the source of non-radiative recombination in GaInNAsSb/GaNAs lasers by the incorporation of modulation doping, this approach however was only partially successful; this may have been due to the fact that the levels of doping used were not sufficiently large. In this chapter I will give details of experiments I performed on some GaInNAsSb/GaNAs lasers emitting at 1.56μm, where instead of varying the doping level as was done in chapter 4, three different variables were changed; firstly the Nitrogen content is varied, then the number of wells and finally the size of the barriers (GaNAs). The purpose of these experiments is to find out how much of the non-radiative current is due to recombination in the barrier material and how much is due to recombination in the well, with the ultimate aim being to show if and by how much the non-radiative current could be reduced using a different design or combination of materials and so optimise the material.

5.2 Details of Material

The material used in this chapter was grown by the Harris group in Stanford University. The samples were grown using molecular beam epitaxy (MBE) and contain 7 nm wide GaInNAsSb quantum wells within GaNAs barriers which are then all situated in GaAs. After growth, the lasers were annealed at 680°C for 10 minutes in a rapid thermal annealer furnace using a GaAs proximity cap to minimize arsenic desorption. Details of growth of similar samples can be found in (Bank et al, 2007).

In total six different types of sample were studied, these consisted of three with Nitrogen content in the well of 3.0% and three with 3.3%. These sets of three were then made up of: a single well with 10nm barriers, a single well with 20nm barriers and a three well with 20nm barriers between each well and between the GaNAs and GaAs, as represented in Figure 32. A table listing the different structures is shown in Table 4

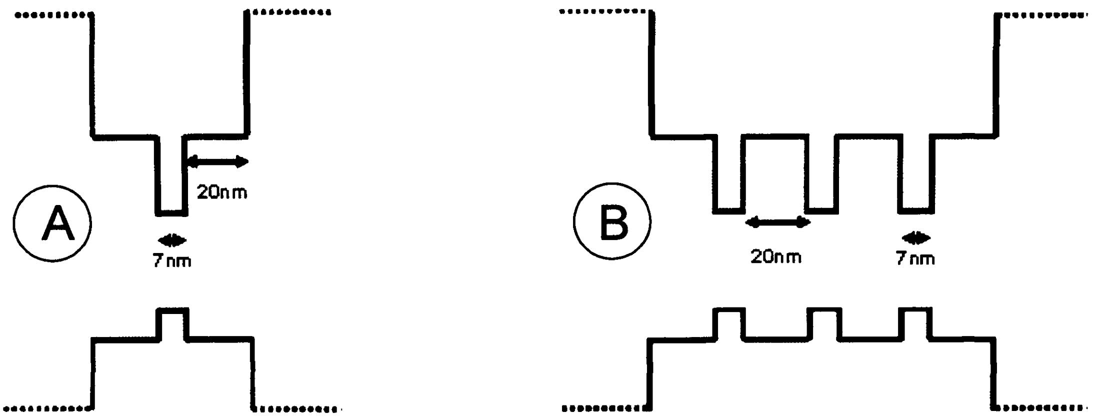

Figure 32. A schematic diagram of a single well with 20nm barriers structure (labelled A) and a three well structure (labelled B).

Nitrogen Content / %	Number of quantum wells	Barrier thickness / nm
3.0	1	10
3.0	1	20
3.0	3	20
3.3	1	10
3.3	1	20
3.3	3	20

Table 4. List of GaInNAsSb/ GaNAs samples provided by the Harris group.

The single well 20nm barriers and three well structures contain nominally identical well and barrier composition and thickness for a given nitrogen content. It is therefore possible to use a simple analysis to extract the contribution to the non-radiative current that both the barriers and the well(s) make; this is done by comparing the total non-radiative current, found by subtracting the radiative current (found by integrating the spontaneous emission) from the total current, of the one and three well samples containing the same nitrogen content at the same injection level. We represent the non-radiative current density in one well by W and in one barrier by B, the non-radiative current in the one well sample is $J_{nr}(1) = (1W+2B)$ and in the three well sample it is $J_{nr}(3) = (3W + 4B)$. Then using some simple algebra the non-radiative current in one barrier is described by Equation 43.

$$B = \frac{3*(J_{nr}(1)) - (J_{nr}(3))}{2}$$

Equation 43

This value is then multiplied by the number of barriers and subtracted from the total non-radiative current leaving just the contribution made by the well(s). I can then asses the relative importance of the barriers on the total non-radiative recombination and hence their impact on the overall efficiency of the devices. This approach assumes that there is no leakage of carriers from the well(s) to the cladding region and that all the wells and barriers are identical. Any recombination at an interface between the well and the barrier is considered to be recombination in the well and would scale with well number.

The two single well samples will be compared to each other, the thinner barrier will mean that at a given quasi-Fermi level there are assumed to be less carriers in the barrier (same assumed carrier density but thinner barrier) and therefore there will be less total recombination per unit area in them if they are identical other than the width (so same carrier lifetimes). To make sure that material quality degradation due to changes in the growth conditions did not lead to false conclusions, the order in which the samples were grown was selected so that any effect would not be the same in the 3.0% nitrogen sample set and the 3.3% nitrogen sample set.

5.3 Band Structure

Figure 33 (Bank, 2007) shows a schematic of the band gap of the component materials in the structure of the samples used in this work (Ref, Private communication with H. Bae). Figure 33 was obtained using contactless electro reflectance (CER) technique. The CER technique directly measures the energies of transitions and then uses theoretical calculations to find fundamental parameters such as the band offsets, this is described in detail in (Kudrawiec, 2007).

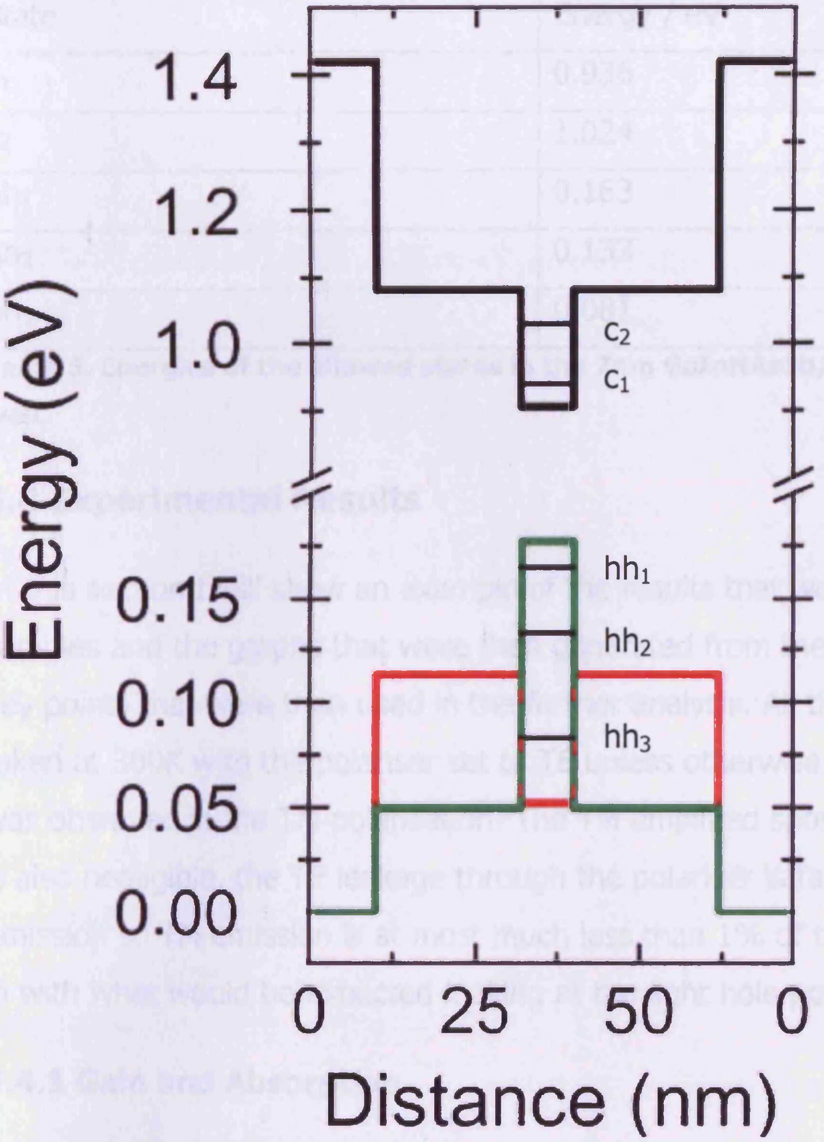

Figure 33. Band Diagram obtained from CER and theoretical calculations, Red lines are light holes Green lines are heavy holes. Note the smaller scale on the y-axis for the valence band. (Bank 2007). Marked on are the heavy hole (hh) confined states and the conduction band states (c)

The results indicate that the band offset is bigger for the conduction band compared to the valence band, 171meV compared to 54meV. It also shows that the light holes are not confined within the well. Figure 33 suggests that there will be negligible leakage into the cladding layers due to the large band offsets between well and cladding; 0.52 eV in the conduction band and

0.18eV in the valence band. A table showing the energies of the different allowed confined states is shown in Table 5.

State	Energy / eV
c_1	0.936
c_2	1.024
hh_1	0.163
hh_2	0.133
hh_3	0.081

Table 5. Energies of the allowed states in the 7nm GaInNAsSb/GaNAs quantum well.

5.4 Experimental Results

In this section I will show an example of the results that were taken on all the samples and the graphs that were then generated from them, outlining the key points that were then used in the further analysis. All the data shown are taken at 300K with the polariser set to TE unless otherwise stated. No gain was observed in the TM polarisation. The TM amplified spontaneous emission is also negligible, the TE leakage through the polariser is far larger than TM emission so TM emission is at most much less than 1% of the total. This fits in with what would be expected looking at the light hole position in Figure 33.

5.4.1 Gain and Absorption

Figure 34 shows an example net modal gain spectrum (Blue dashed line) and absorption spectrum (Red solid line) for the 3.0% nitrogen thin barrier sample. The gain and absorption spectra are similar for all the samples.

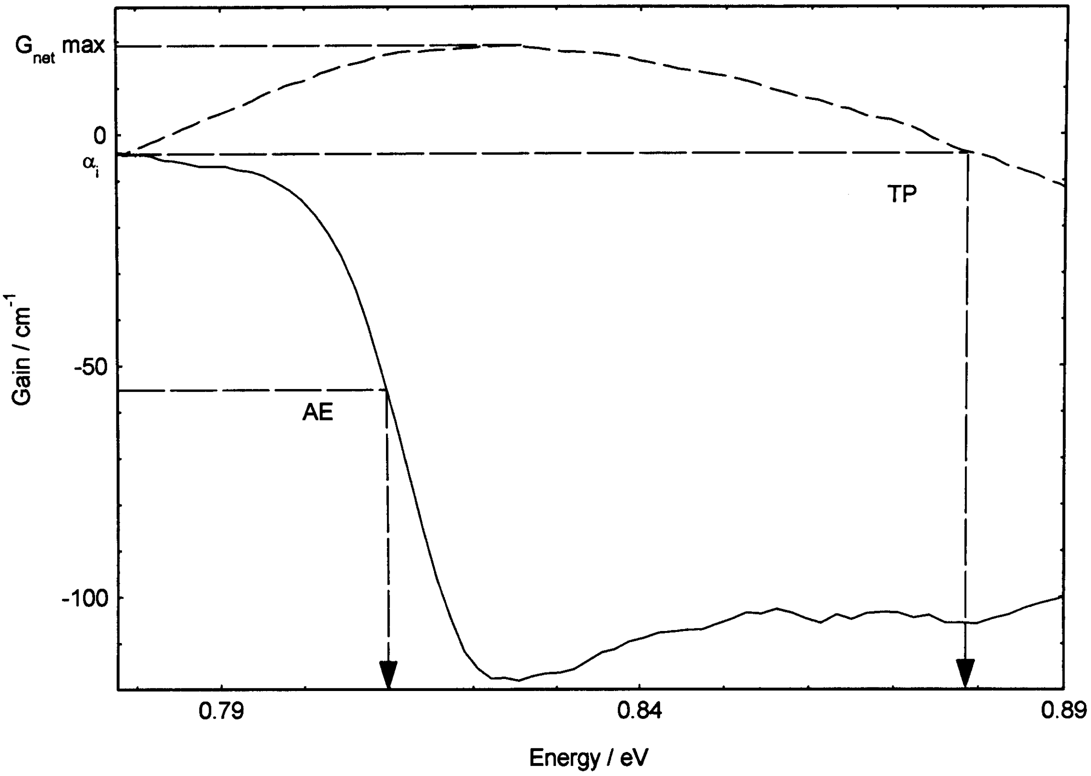

Figure 34. A graph showing the net modal gain against energy for the 3.0% nitrogen 10nm barrier sample.

Marked on Figure 34 are the TP, AE, α_i and G_{max} whose meanings were explained in chapter 4. However the way AE is defined here is slightly different as here it was taken at a value of $-50cm^{-1}$ on the absorption curve, after α_i had been added, (i.e. $-50cm^{-1} - \alpha_i$), for the one well samples and at $-150cm^{-1}$ for the 3 well samples as the modal absorption and modal gain of the three well structure is expected to be three times that of the single well structure, due to the differences in total optical confinement factor. The validity of this assumption is confirmed when looking at the peak modal gain as a function of radiative current density and is discussed in 5.4.4.

What appear to be features in the absorption spectrum at roughly 0.85eV and 0.88eV and the feature seen between 0.82eV and 0.83eV are the results of noise and are not real. No corresponding features are seen in the gain spectrum or are seen in the spontaneous emission as shown in Figure 36. The absorption spectra are measured at different currents and these features do not appear the same each time; the region of the spectra before it flattens off at high energy is constantly reproduced, as is the α_i region.

5.4.2 Calibrated spontaneous emission rate spectra

As detailed in chapter 3, in order to calibrate the spontaneous emission spectra the flat region of the population inversion factor (P_f), where all the spectra saturate independent of current must be found. P_f spectra for the 3.0% 10nm barrier can be seen in Figure 35

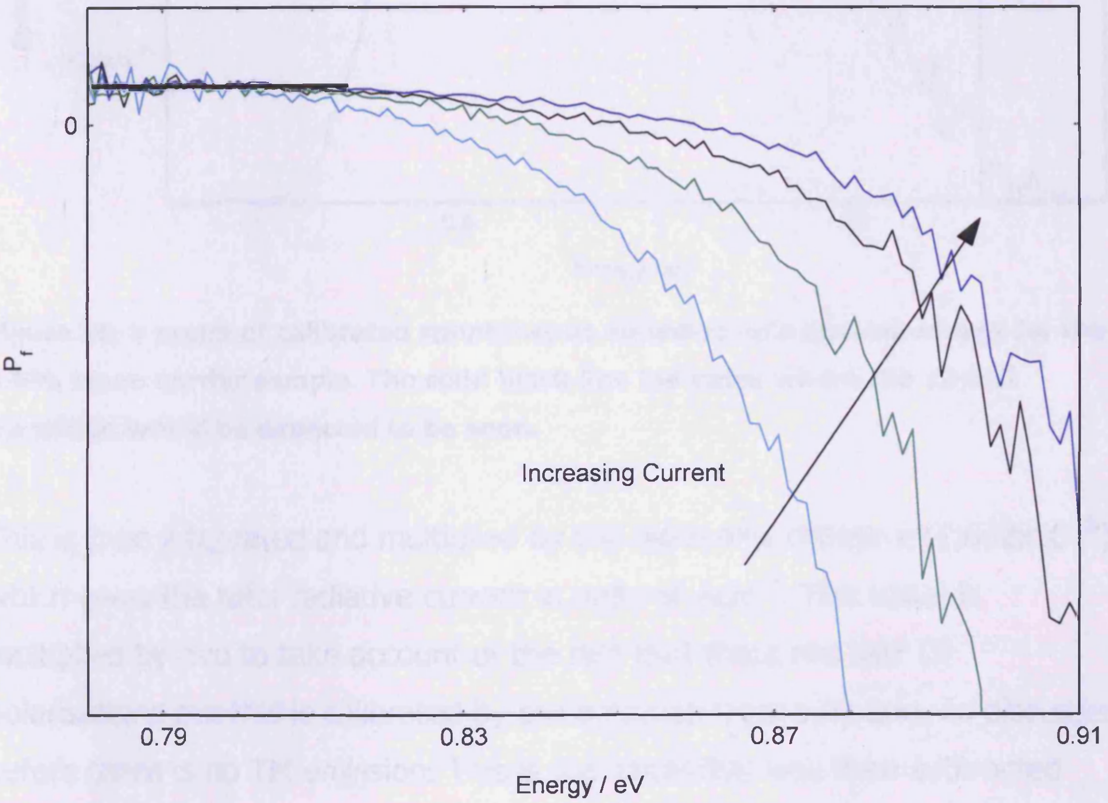

Figure 35. Population inversion factor for the 3.0%N 10nm barrier sample. The flat region where the P_f spectra saturate is indicated by the horizontal black line.

Figure 36 shows a spontaneous emission rate spectrum obtained using the calibration factor from the P_f, as described in chapter 3.

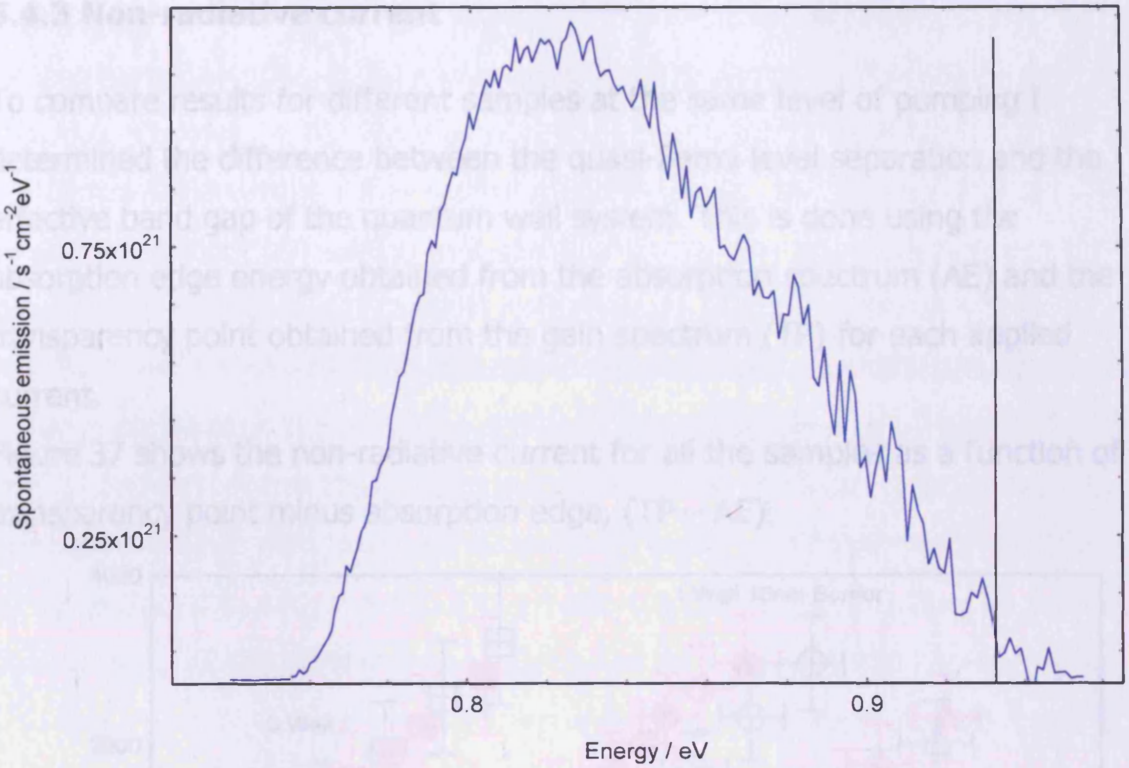

Figure 36. a graph of calibrated spontaneous emission rate against energy for the 3.0% 10nm barrier sample. The solid black line indicates where the c2-hh2 transition would be expected to be seen.

This is then integrated and multiplied by the electronic charge *e* (1.602×10^{-19}) which gives the total radiative current in units of Acm^{-2}. This value is multiplied by two to take account of the fact that there are two TE polarisations but this is calibrated by the emission from only one. As discussed before there is no TM emission. This is the value that was then subtracted from the total applied current to give the non-radiative current.

Figure 36 does not show any evidence of there being any recombination from a second state, this is also true when the spontaneous emission was looked at over the full range of currents and temperatures for all the samples used in this chapter. This is supported by the expected separation of the c1-hh1 and c2-hh2 transitions which can be observed from the data of Table 5, to be 118meV, the position where this second transition would occur is shown on Figure 36.

5.4.3 Non-radiative current

To compare results for different samples at the same level of pumping I determined the difference between the quasi-Fermi level separation and the effective band gap of the quantum well system. This is done using the absorption edge energy obtained from the absorption spectrum (AE) and the transparency point obtained from the gain spectrum (TP) for each applied current.

Figure 37 shows the non-radiative current for all the samples as a function of transparency point minus absorption edge, (TP – AE).

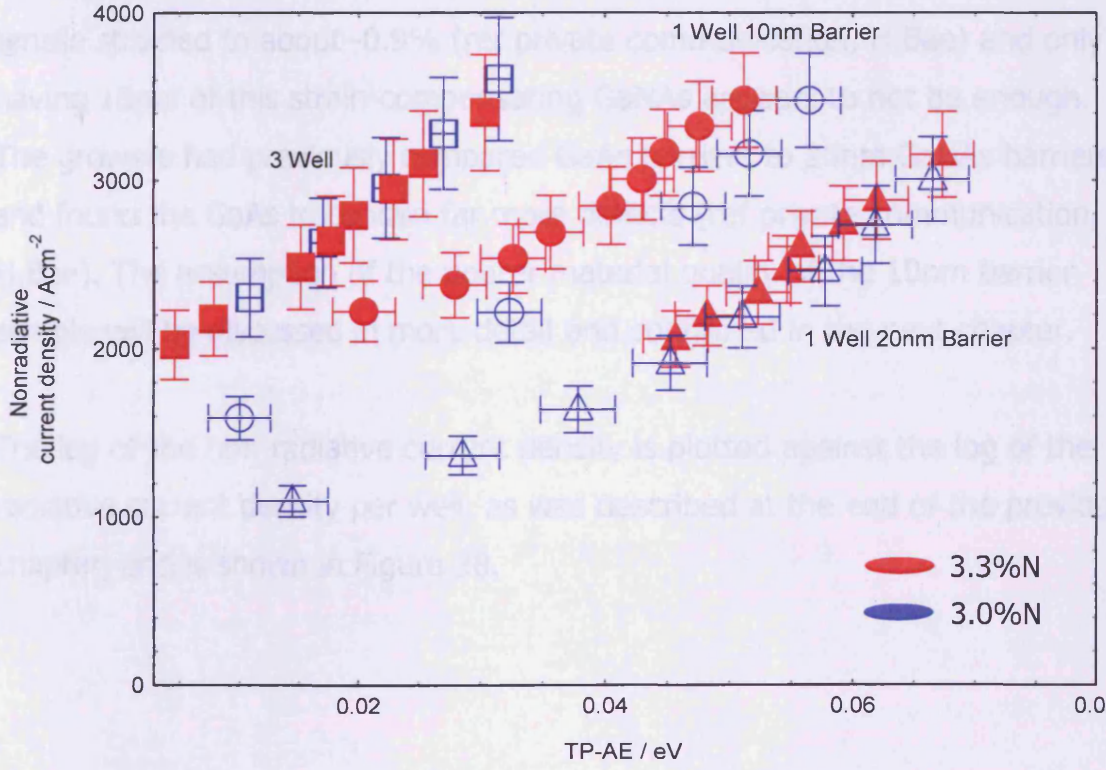

Figure 37. Non-radiative current against TP – AE for GaInNAsSb/GaNAs. The blue points are 3.0% N, the red 3.3% N. The squares are the three well samples, circles are the 10nm barriers single wells and the triangles are the 20nm barrier single wells

Figure 37 shows that the results fall into three groups, based on well number/barrier size. The three well samples have the largest non-radiative current for a given TP-AE, this is to be expected as there are 3 wells as opposed to one, and four barriers compared to two. The surprising result is that the thinner barrier sample has a higher non-radiative current than the thicker barrier sample. If the material was of the same quality (same non-radiative lifetimes) in the two samples then the opposite would be true (assuming that there is some barrier recombination), this implies that by having the thinner barrier the material quality has been degraded, which is investigated further and discussed in chapter 6. This is consistent with this structure design having higher threshold currents for lasers and having 4x lower photoluminescence (ref private communication, H. Bae). This will be due to there being insufficient strain compensation introducing extra defects. The GaInNAsSb is compressively strained to about +2.5% whilst the GaNAs is tensile strained to about -0.9% (ref private communication, H.Bae) and only having 10nm of this strain-compensating GaNAs appears to not be enough. The growers had previously compared GaAs barriers to 20nm GaNAs barriers and found the GaAs to contain far more defects (ref private communication, H.Bae). The assumption of the poorer material quality of the 10nm barrier sample will be discussed in more detail and confirmed in the next chapter.

The log of the non-radiative current density is plotted against the log of the radiative current density per well, as was described at the end of the previous chapter, and is shown in Figure 38.

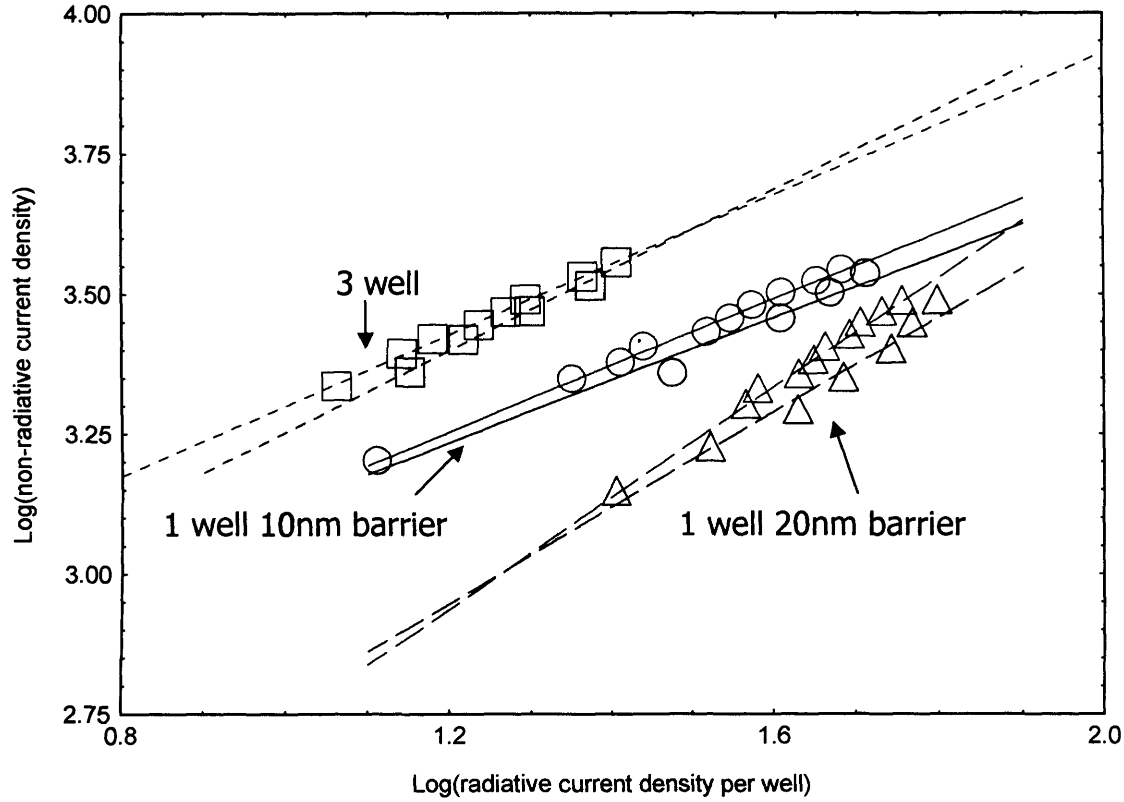

Figure 38, log(non-radiative current) vs log(radiative current) for GaInNAsSb/GaNAs samples. The blue points are 3.0% N, the red 3.3% N. The squares are the three well samples, circles are the 10nm barriers single wells and the triangles are the 20nm barrier single wells

The gradients of lines in Figure 38 can be seen in Table 6

Sample	Gradient
10nm barrier 3.0%N	0.56 ± 0.10
10nm barrier 3.3%N	0.60 ± 0.11
20nm barrier 3.0%N	0.85 ± 0.15
20nm barrier 3.3%N	0.99 ± 0.18
3 Well 20nm barrier 3.0%N	0.72 ± 0.13
3 Well 20nm barrier 3.3%N	0.63 ± 0.11

Table 6. Gradients from the log(non-radiative) vs log(radiative) plot for the GaInNAsSb/GaNAs samples

Looking at Table 6 we can see that the gradient of the line for the thin well samples is close to 0.5, this implies that SRH recombination in the well makes up a large part of the total non-radiative recombination in the well. At first glance it seems strange that the gradients of the 20nm barrier single well and the three well samples should be so different as the material quality is assumed to be the same in these samples, however this is due to two reasons: Firstly the effect of leakage to the barriers will be greater in the one well sample as the barrier to well ratio is 2:1 compared to 4:3; this is because the number of carriers in the barriers compared to the number of carriers in the well(s) increases faster with increasing quasi-Fermi level separation for the single well sample which will increase the gradient. Secondly the three well samples are not being driven as hard, as can be seen from the lower radiative current and from looking at the values of TP-AE shown in Figure 37; this affects the value of the gradient as the harder a sample is being driven the more carriers will leak to the barriers thus increasing the gradient. Any Auger recombination will also increase. This effect of the different levels of pumping as well as the differences between the 10nm barrier material quality compared to the other two designs will be discussed in more detail in chapter 6.

For the rest of this chapter only the thicker barrier single well samples and the three well samples will be used, because they are assumed to be of comparable material quality. This is confirmed by work presented in chapter 6.

Figure 37 also shows that the addition of more nitrogen has not increased the total non-radiative current in the cases of the three well samples and the 20nm single well samples.

5.4.4 Gain comparison

Figure 39 shows the peak modal gain per well against the radiative current density per well, obtained by measuring the gain spectra over a range of different external applied currents (using the SCM) and recording the peak modal gain and radiative current densities (found using the approach shown in section 5 previously) associated with each applied current. To get the three well sample values the total modal gain and radiative current density was divided by three, which assumes that the optical confinement factor per well is the same in the one and three well structures.

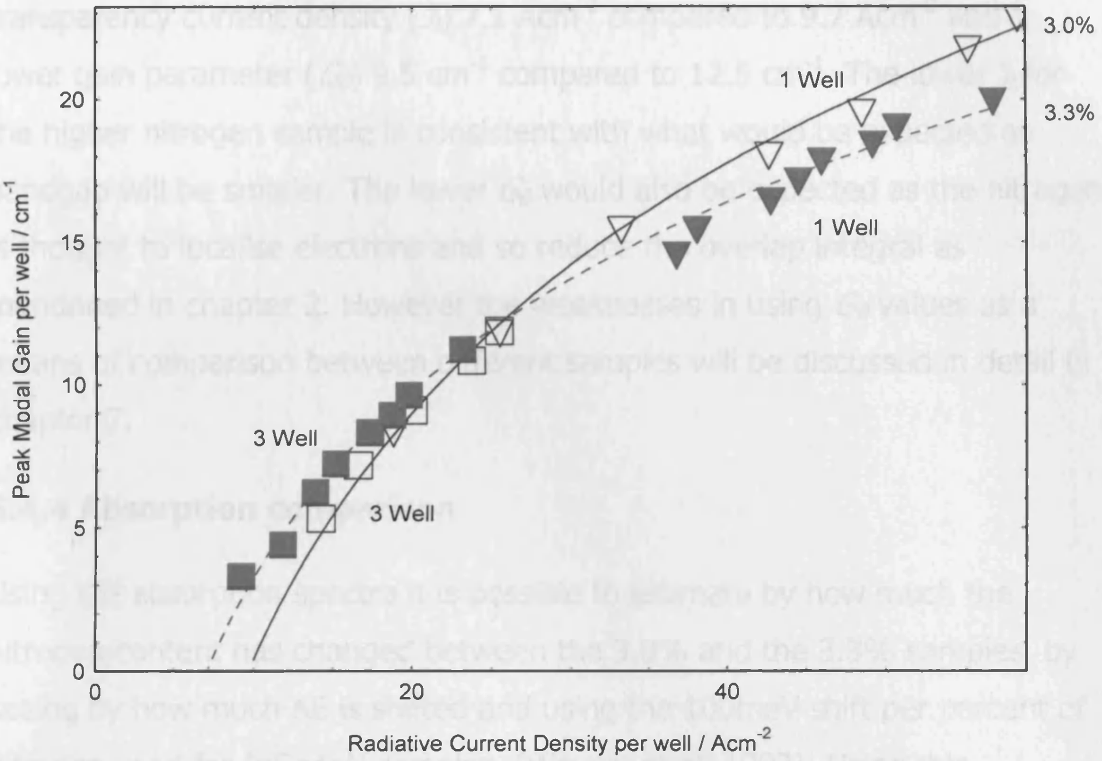

Figure 39. Modal gain per well against radiative current density per well. Blue points are 3.0% N, red 3.3%N. Triangles one well samples, squares three well samples.

The lines in Figure 39 are the result of a fit to the data using the equation $G=G_0 \ln(J/J_t)$ (Coldren and Corzine, 1995). G_0 is the tangential gain parameter and is the point on the gain current curve where the tangent to the curve passes through the origin of the graph, (where $\frac{dG}{dJ}=\frac{G}{J}$). J_t is the transparency current, it is the value of current at which the gain is equal to 0cm^{-1}. The same values of G_0 and J_t can be used to describe the samples containing the same amount of nitrogen but different number of wells. The fit quality when combining the data for the same nitrogen containing samples into one data set as has been done in Figure 39 is as good as when the fit is applied to the one and three well samples individually. This is consistent with each well in the three well samples and the well in the one well samples being equally populated and the optical confinement factor being the same for each well, as was assumed in the treatment of the absorption edge in section 5.4.1 Gain and Absorption. The higher nitrogen content results in a slightly lower transparency current density (*J_t*) 7.1 Acm^{-2} compared to 9.7 Acm^{-2} and a lower gain parameter (*G_0*) 9.5 cm^{-1} compared to 12.5 cm^{-1}. The lower J_t for the higher nitrogen sample is consistent with what would be expected as bandgap will be smaller. The lower *G_0* would also be expected as the nitrogen is thought to localise electrons and so reduce the overlap integral as mentioned in chapter 2. However the weaknesses in using *G_0* values as a means of comparison between different samples will be discussed in detail in chapter 7.

5.4.4 Absorption comparison

Using the absorption spectra it is possible to estimate by how much the nitrogen content has changed between the 3.0% and the 3.3% samples, by seeing by how much AE is shifted and using the 100meV shift per percent of nitrogen used for InGaAsN samples, (Weyers et al, 1992). Using this technique a difference of 17meV for the one well structures and 12 meV for the three well structures is found, indicating that the difference in nitrogen content may not be as large as the intended 0.3%. However it may be the case that for the GaInNAsSb material the 100meV per percent of nitrogen is not correct.

The shape of the absorption spectra can also be used to compare the levels of inhomogeneous broadening in the samples. To do this α_i was added to all the absorption spectra to change the scale to modal gain from net modal gain. The spectra were then shifted on the x axis to all have the same effective AE. The three well absorption spectra were then divided by three to take account of the difference in total optical confinement, so that the spectra can be compared at the same point on the curve. The reason that the maximum absorption is not the same for the one well and three well divided by three is assumed to be because the signal to noise in the measurement does not allow the true maximum absorption value to be found and this has a larger influence on the three well sample results. The modified absorption data are plotted in Figure 40

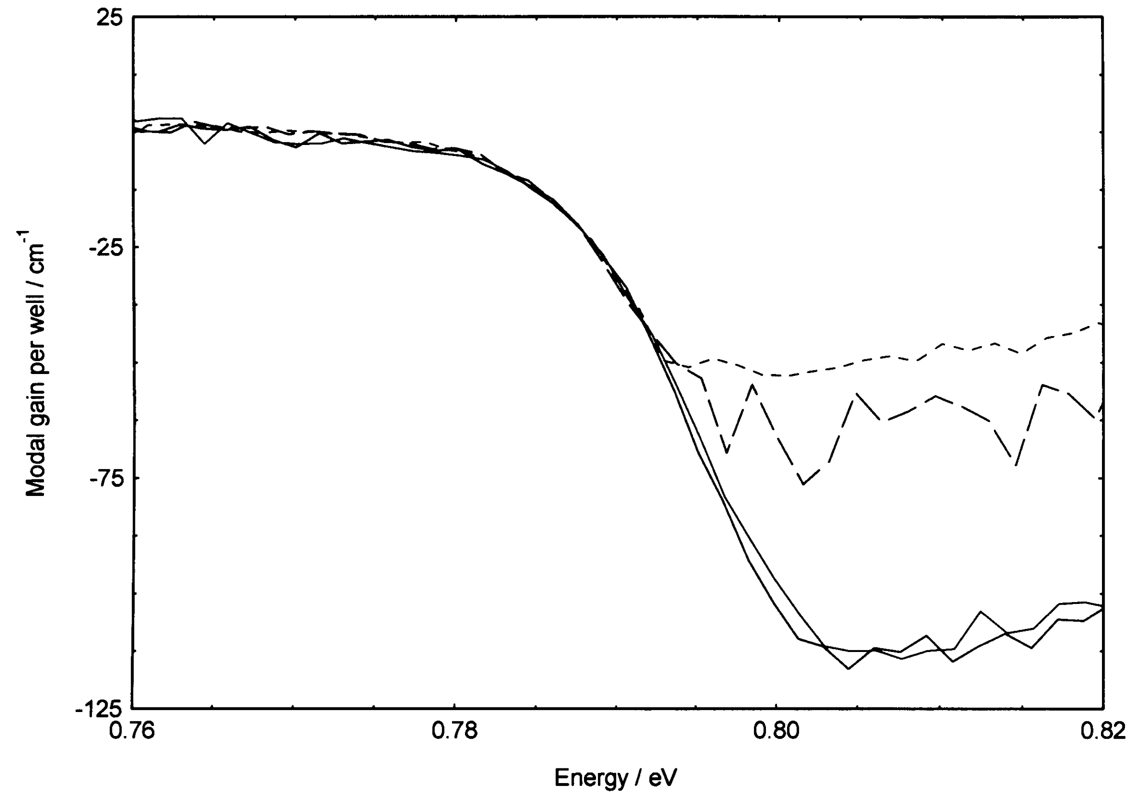

Figure 40. Comparison of modified absorption spectra for the GaInNAsSb samples. Blue for the 3%N, red for 3.3%N. Dashed lines are the three well samples divided by three, solid lines are the one well samples.

The similarity in the shape of the absorption spectra specifically near the absorption edge suggests that the inhomogeneous broadening is the same in all the samples. As was mentioned in chapter 4 it is important to note where the absorption spectra appear to reach their maximum absorption is not the true maximum. Due to signal to noise issues in the experiment, the true absorption curves of the 3 well samples would continue to follow the 1 well sample curves before reaching the same maximum absorption.

5.5 Finding the non-radiative current due to one barrier and one well

The results of Figure 39 indicate that the barriers and the wells are the same in all four of the samples and from Figure 33 that there is negligible leakage into the cladding layers due to the large band offsets between well and cladding GaAs (0.52eV in the conduction band and 0.18eV in the valence band). This means that Equation 43 can be used as all the non-radiative current will be in either the barriers or the well(s) which is the assumption that is made when using the equation.

Values of B and W can be found for any value of TP-AE where there is non-radiative current density data for both the one well samples and the three well samples.

5.5.1 Example of working out a value for B and W

At a value of TP-AE of 0.025 eV the non-radiative current density of a three well sample is 3123 Acm^{-2} and of single well is 1339 Acm^{-2}. Using Equation 43;

$2B = (3*1339) - 3123 = 894$ Acm^{-2}

So $B = 447$ Acm^{-2}. Using the single well value to find out W;

$1339 - (2*447) = 445$ Acm^{-2} $= W$.

This example shows that at this value of (TP – AE) the contribution that one barrier makes to the non-radiative current density is roughly the same as the contribution that one well makes.

5.5.2 B and W as a function of TP-AE

Figure 41 shows values of non-radiative current density for a well and a barrier of a range of values of TP-AE.

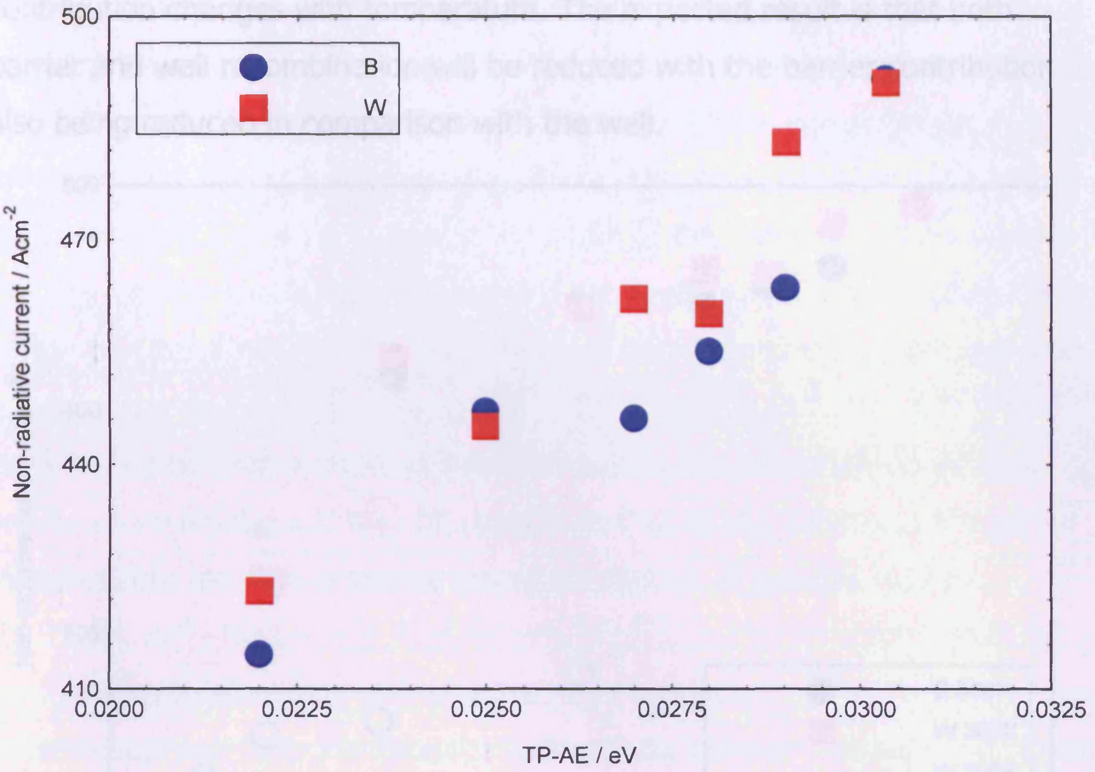

Figure 41. Shows values of non-radiative current density for a well (W) and a barrier (B) as a function of TP-AE

It shows that the values of *B* and *W*, over the range of TP-AE that it is possible to extract values, are roughly equal. This is a surprising result because the carrier density will be higher in the well compared to the barrier. The reason for them being equal despite this is twofold; the barriers are nearly 3 times as wide as the well; the way the samples are grown means that the nitrogen content in the barrier is roughly 40% higher meaning that there will be far more defects introduced by nitrogen in the barrier (as mentioned in chapter 2). Thus the barriers make a significant contribution to the non-radiative current density; in a single well device they account for two thirds of the total; and for the three well device they account for four sevenths of the total.

5.5.3 Finding *B* and *W* at 200K

The same experiments that have been described previously in this chapter at 300K were also performed at 200K. This was done to see how the barrier contribution changes with temperature. The expected result is that both barrier and well recombination will be reduced with the barrier contribution also being reduced in comparison with the well.

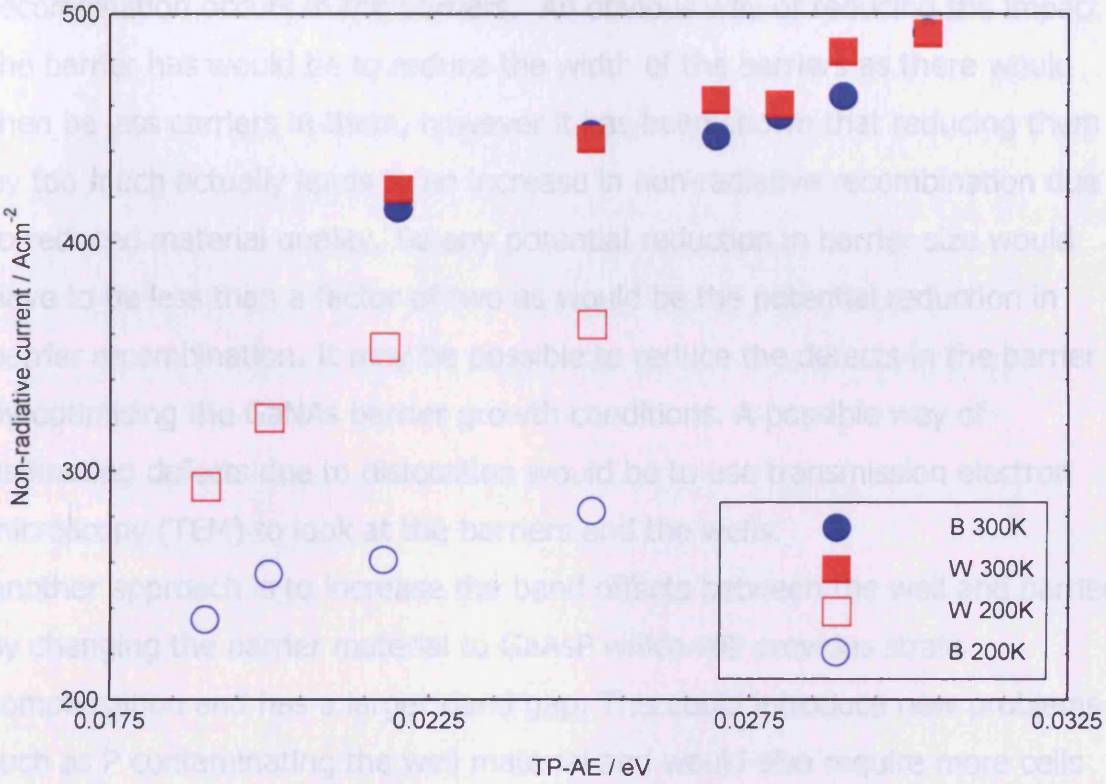

Figure 42. Shows the non-radiative current from one well (W) and one barrier (B) at a given TP-AE at 200K. Also shown are the 300K results.

The data from Figure 41 are included in Figure 42 to allow ease of comparison. It is apparent that the total non-radiative current for a given TP-AE has reduced with the reduction in temperature. The comparison also shows that the contribution that the barrier makes relative to the well has gone down and this is consistent with reduced population in the well and particularly the barrier at lower temperatures, which is all as expected.

5.6 Chapter Conclusions

In this chapter I have shown that the contribution that one barrier makes to the total non-radiative current at 300K is equal to that of a well. For example at a value of TP-AE of 0.025eV the non-radiative recombination in one well is 445Acm^{-2} and in one barrier is 447Acm^{-2}. This highlights how important careful barrier design is when trying to make an efficient device (implications of the quality of the barrier material will be discussed in the next chapter), as this means that in a single well device two thirds of the non-radiative recombination occurs in the barriers. An obvious way of reducing the impact the barrier has would be to reduce the width of the barriers as there would then be less carriers in them, however it has been shown that reducing them by too much actually leads to an increase in non-radiative recombination due to reduced material quality. So any potential reduction in barrier size would have to be less than a factor of two as would be the potential reduction in barrier recombination. It may be possible to reduce the defects in the barrier by optimising the GaNAs barrier growth conditions. A possible way of estimating defects due to dislocation would be to use transmission electron microscopy (TEM) to look at the barriers and the wells.

Another approach is to increase the band offsets between the well and barrier by changing the barrier material to GaAsP which still provides strain compensation and has a larger band gap. This could introduce new problems such as P contaminating the well material and would also require more cells on the MBE reactor. The significant barrier recombination even at 200K (at a TP-AE of 0.022 non-radiative current density is 261Acm-2 in a barrier and 354Acm^{-2} in a well) suggests that the increase in band gap needed to significantly reduce recombination in the barriers is larger than would be possible by slightly altering the nitrogen concentration in the barrier.

Using Figure 39 the ultimate performance of this material has been found. If all the non-radiative recombination could be removed using a combination of changes in growth and layer design, then for a laser of length 1 mm, with uncoated facets, and an optical loss of 17 cm^{-1} (α_i = 5 cm^{-1}), the radiative threshold current density is 35 Acm^{-2} for a single well device. This compares well with 1.3µm InAs quantum dot material where the saturated gain is also relatively low (O' Driscoll et al, 2009).

5.7 References

- Bank. S.R, Bae. H, Goddard. L.L, Yuen. H.B, Wistey. M.A, Kudrawiec. R, Harris. J.S, "Recent Progress on 1.55 μm Dilute-Nitride Lasers" IEEE Journal of Quantum Electronics, 43, 9, (2007)
- Coldren. L.A and Corzine. S.W, Diode Lasers and Photonics Integrated Circuits, Wiley Series in Microwave and Optical engineering, Vol 1, Kai Chang, 1995
- Kudrawiec. R, Yuen. H.B, Motyka. M, Gladysiewicz. M, Misiewicz. J, Bank. S.R, Bae. H.P, Wistey. M.A, and Harris. J.S, "Contactless electroreflectance of GaInNAsSb–GaAs single quantum wells with indium content of 8%–32%". J. Appl. Phys, 101, 013504 (2007)
- O' Driscoll. I, Smowton. P.M, Blood. P, IEEE J Quantum Electron, 45, 4, pp 380-387 (2009)
- Weyers. M, Sato. M and Ando. H, Appl. Phys. Vol. 31 pp 853-855 (1992)

6. Simulation

6.1 Reason for doing simulation

In chapter 5 I showed that the barriers make a very large contribution to the non-radiative current. The source of this non-radiative recombination is not clear, it could be Auger or Shockley-Reed-Hall. By simulating the carrier transport and recombination in the structures it will be possible to identify which of these is the main source.

6.2 Software used

The simulation software used is called Sim Windows (Ref Sim Windows).
It is a one dimensional Schrodinger, Poisson, continuity equation solver that uses Fermi statistics. This has previously been used to model vertical cavity surface emitting lasers (Winston and Hayes, 1998) and InGaN LED structures (Thomson et al, 2006). The software produces graphs of Shockley-Reed-Hall, Auger and radiative recombination and current flow as a function of distance through the device, for a given applied voltage.

6.3 Using the software

Simwindows uses a library of material parameters but these parameters were not available by default for GaInNAsSb or GaNAs, I therefore collected values from literature. Table 7 shows the material parameters used for GaInNAsSb and GaNAs.
The variable changed in the program is applied bias, this was increased until the injection level in the model matched the injection level in the experiments. Simwindows does not take into account the effect of band gap renormalisation so it is necessary to work out how large the band gap renormalisation is and to then take account of it when using the software, I found the effect of this by using the difference between where the absorption spectra and where the gain spectra plateau, shown in Figure 43.

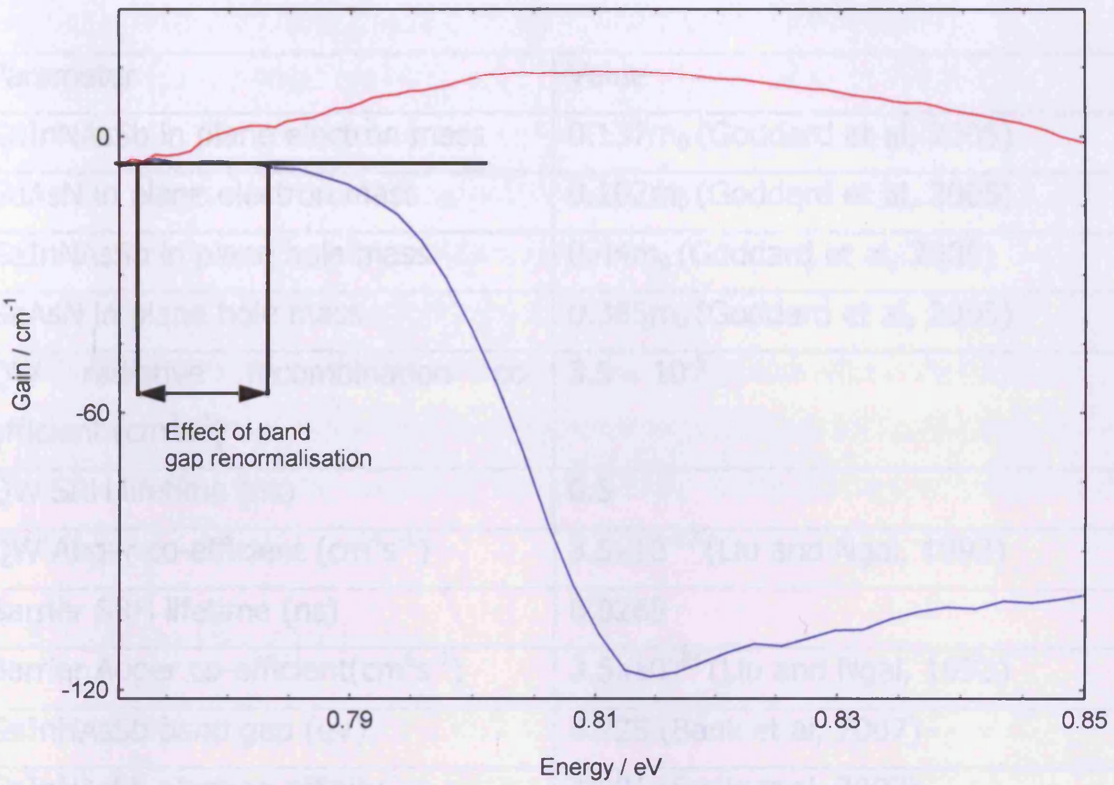

Figure 43. Experimental plot of net modal gain (Red line) and absorption (Blue line) against energy showing the effect of band gap renormalisation.

Once the simulation is at the correct quasi-Fermi level the recombination due to Auger, Shockley-Reed-Hall (SRH) and Radiative recombination throughout the structure can be plotted.

6.4 Input Parameters

Table 7, shows the input parameters that were used in the simulations.

Parameter	Value
GaInNAsSb in plane electron mass	$0.137m_0$ (Goddard et al, 2005)
GaAsN in plane electron mass	$0.102m_0$ (Goddard et al, 2005)
GaInNAsSb in plane hole mass	$0.44m_0$ (Goddard et al, 2005)
GaAsN in plane hole mass	$0.385m_0$ (Goddard et al, 2005)
QW radiative recombination co-efficient (cm^2s^{-1})	3.5×10^{-5}
QW SRH lifetime (ns)	0.5
QW Auger co-efficient (cm^4s^{-1})	3.5×10^{-17} (Liu and Ngai, 1993)
Barrier SRH lifetime (ns)	0.0265
Barrier Auger co-efficient(cm^6s^{-1})	3.5×10^{-29} (Liu and Ngai, 1993)
GaInNAsSb band gap (eV)	0.725 (Bank et al, 2007)
GaInNAsSb electron affinity	4.391 (Bank et al, 2007)
GaAsN band gap (eV)	0.95 (Bank et al, 2007)
GaAsN affinity	4.22 (Bank et al, 2007)

Table 7. The input parameters used in the Simwindows simulations

There are very few or in some cases no papers which detail the parameters needed to put into the Simwindows material library. I picked the majority of papers that I did use because they were for material that was grown by the Stanford group so should also be correct for the samples I've used. In the case of the Auger co-efficient a material that emits at the same wavelength was picked as none could be found for GaInNAsSb. This means that the Auger co-efficient could be in error, the effect that this could have is discussed and dealt with later in the chapter, the value of Auger co-efficient was kept the same in the well and the barrier due to the similarities in the material (in the barrier it is in terms of recombination per unit volume whereas in the well it is recombination per unit area). The effect of errors in this assumption are discussed and dealt with later in this chapter.

Having found values from literature it left three variables to be inputted. From chapter 5 the non-radiative current in a well and barrier and the radiative current at a given TP-AE are known experimentally. The radiative recombination constant was adjusted until at a fixed value of TP-AE the radiative recombination in the simulation matched the experimental result. This then leaves just the SRH recombination times to be inputted, these were adjusted until the total non-radiative current in a well and a barrier in the simulation matched with experimental values at the same value of TP-AE as was used to find the radiative co-efficient. As shown in Table 7 the SRH lifetime in the well is 0.5ns and in the barrier is 0.0265ns, this difference is attributed to the greater expected defect density in the barriers in comparison to the well.

6.5 Testing the simulation

Having matched the radiative and non-radiative currents at one value of TP-AE I then checked that the simulation results matched the experimental results over the whole range of values of TP-AE. The simulated and experimental results of the radiative current are shown in Figure 44.

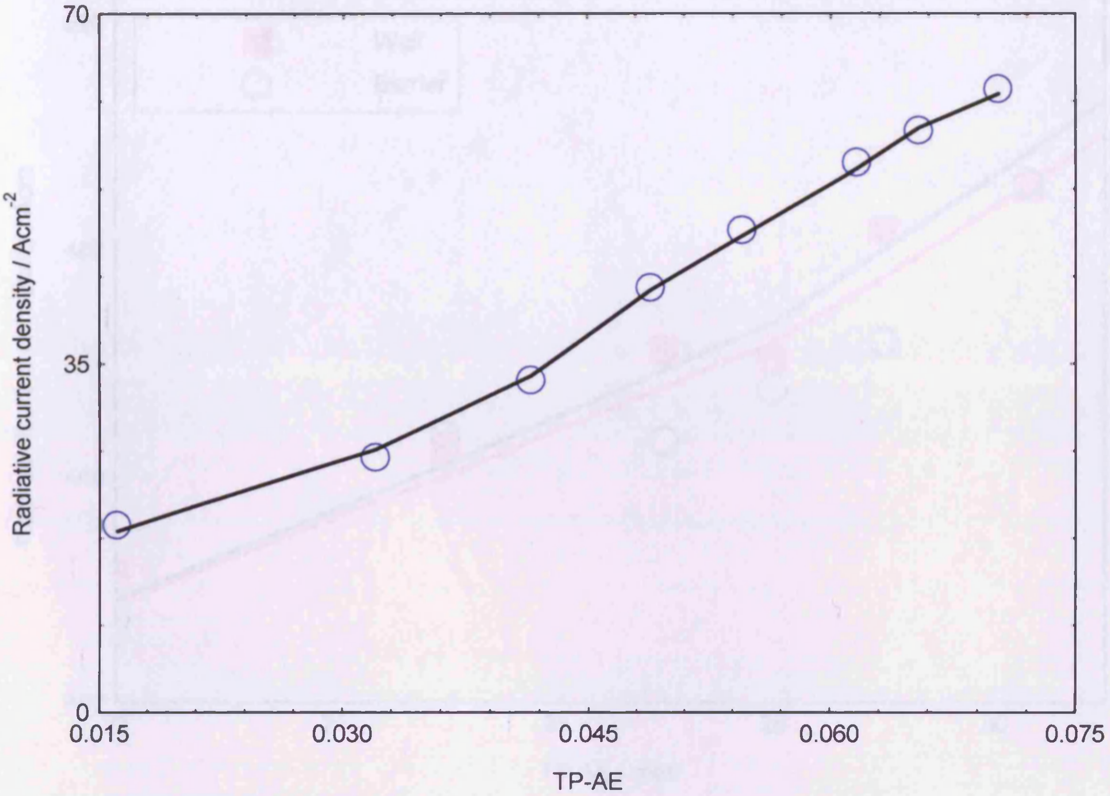

Figure 44. Shows radiative current as a function of TP-AE for the GaInNAsSb/GaNAs samples. Blue circles show the experimental results and the black line is the simulated results.

Figure 44, shows that the simulated values of radiative current match the experimental ones over the whole range of TP-AE. Showing the simulation is matching experiment over the whole range of carrier population.

Having matched the non-radiative current in a well and a barrier at a fixed value of TP-AE, I can now compare the simulated results for a well and a barrier over the whole range of values of TP-AE that were found experimentally in chapter 5. This is shown in Figure 45.

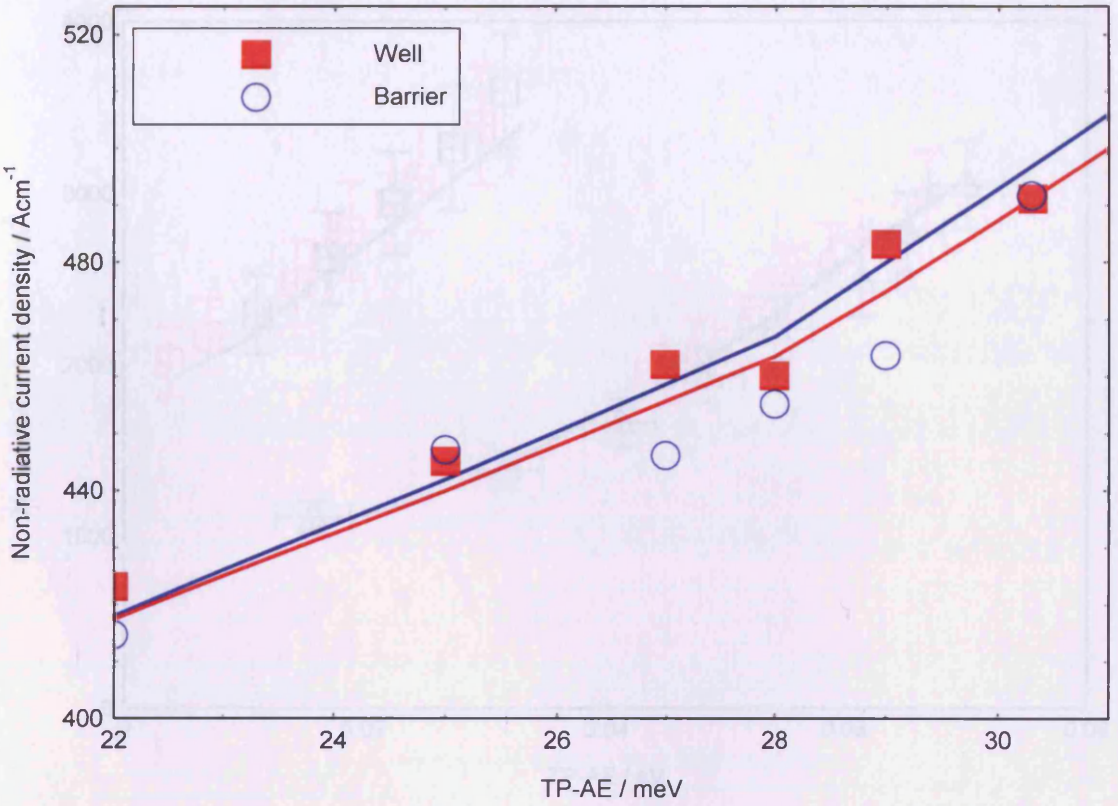

Figure 45. Non radiative current density in one well (red squares) and one barrier (blue circles) found experimentally over a range of values of TP-AE. The lines represent simulated values of non-radiative current density for one well (red line) and one barrier (blue line)

Figure 45 shows that the non-radiative current in one well and one barrier predicted by the simulation matches over the whole range of TP-AE where there is experimental data.

The total non-radiative current for both the one well samples and the three well samples is known over a large range of values of TP-AE, the simulated total non-radiative current and the experimental non-radiative current are compared in Figure 46.

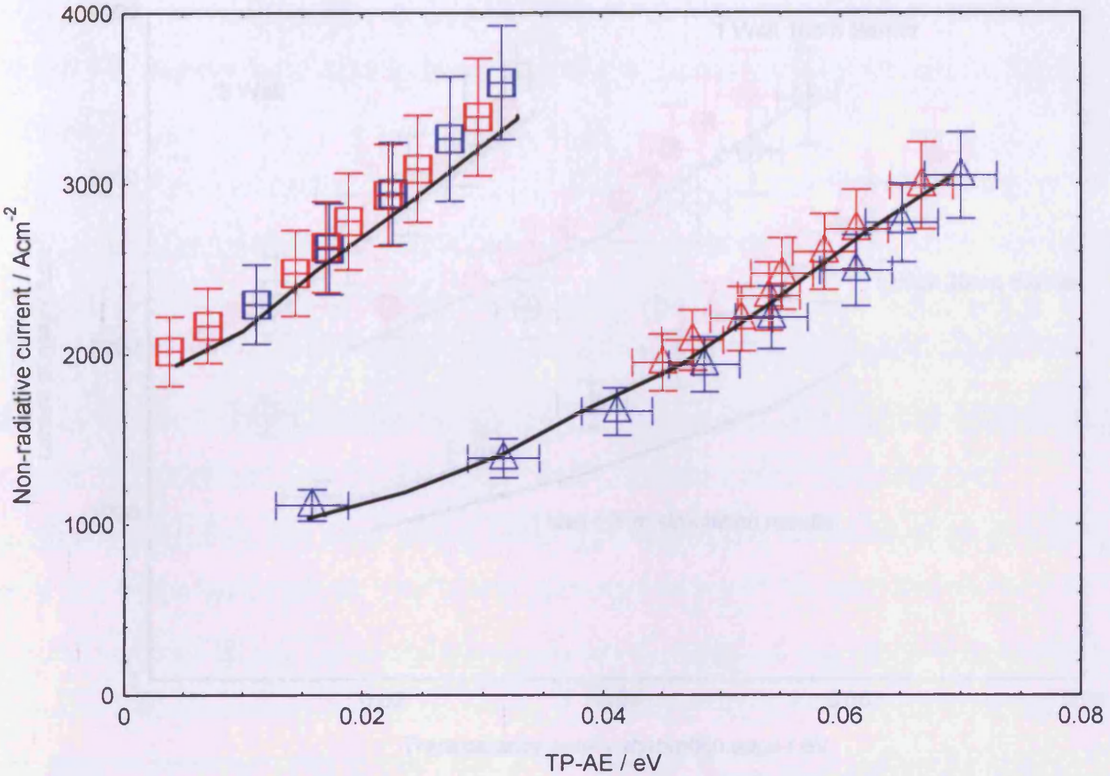

Figure 46. Shows the non-radiative current density as a function of TP-AE, for the 3 well samples (squares) and the one well samples (triangles). The solid lines are the results of the simulation.

The simulated lines in Figure 46 show good agreement for both the one and three well structures over the entire range that has been tested experimentally, so the input parameters used are good approximation of the real life values. Figure 46 shows that the same material parameters can be used to describe both the three well structure and the 20nm single well structure so they are of comparable material quality as was assumed in chapter 5. If the same material parameters are used to try and fit the 10nm single well structures the fit does not work as shown in Figure 47.

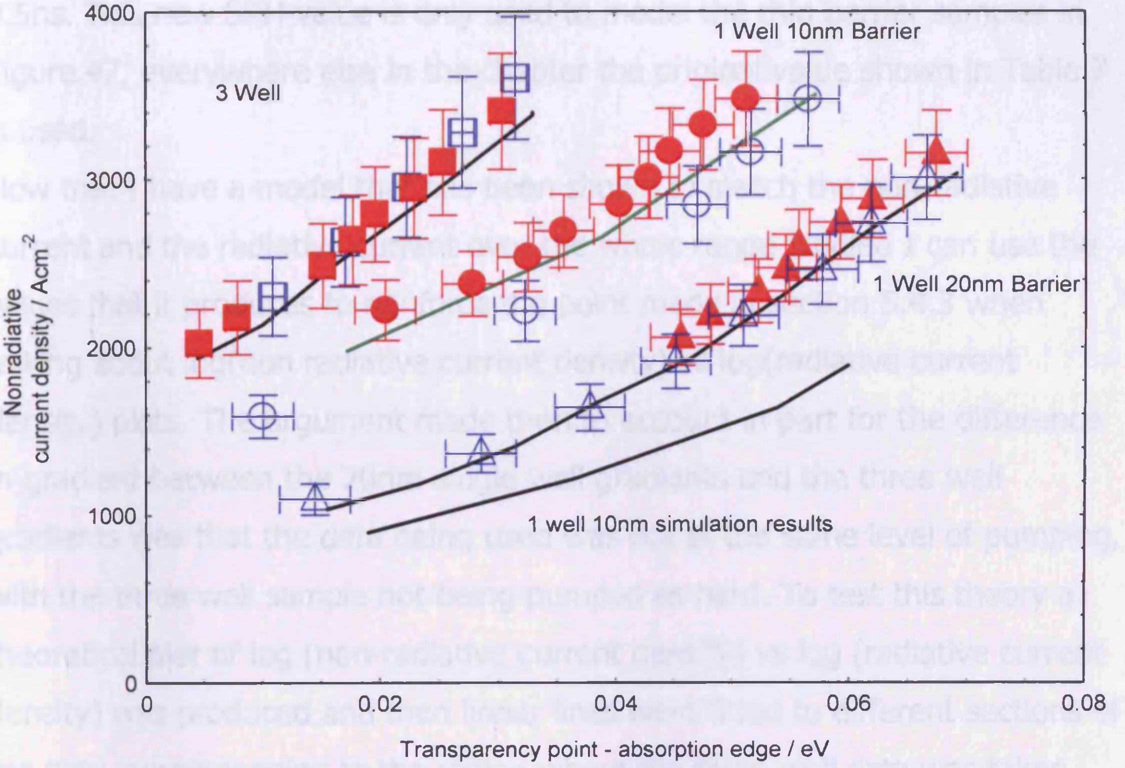

Figure 47. Shows the non-radiative current density as a function of TP-AE, for the 3 well samples (squares), the one well 20nm samples (triangles) and the one well 10nm samples (circles). The solid black lines are the results of the simulation using the original values. The solid green line is the result of the modified simulation

Figure 47 shows that when in chapter 5 the 10nm barrier samples were thought to not be of comparable material quality compared to the other two structure designs it was the correct assumption. The lowest black line shows where these samples would fall were they the same.

In order to produce the solid green line that fits the 10nm single well data shown in Figure 47 the input parameters had to be changed; seeing as the reason for the material degradation is thought to be extra defects being introduced due to insufficient strain compensation, if these extra defects are assumed to appear mainly in the well itself (an assumption supported by the log(non-radiative current) vs log(radiative current) plot in chapter 5) then the only material parameter that needs to be altered is the Shockley-Reed-Hall lifetime in the well. The change in SRH lifetime needed to match up with the experimental results was to make it 4 times faster, 0.125ns compared to

0.5ns. This new SRH value is only used to model the thin barrier samples in Figure 47, everywhere else in the chapter the original value shown in Table 7 is used.

Now that I have a model that has been shown to match the non-radiative current and the radiative current over the whole range studied I can use the values that it produces to reinforce the point made in section 5.4.3 when talking about log(non radiative current density) vs log(radiative current density) plots. The argument made then to account in part for the difference in gradient between the 20nm single well gradients and the three well gradients was that the data being used was not at the same level of pumping, with the three well sample not being pumped as hard. To test this theory a theoretical plot of log (non-radiative current density) vs log (radiative current density) was produced and then linear lines were fitted to different sections of the data, corresponding to the region where the three well data was taken and to where the single well data was taken. This is shown in Figure 48

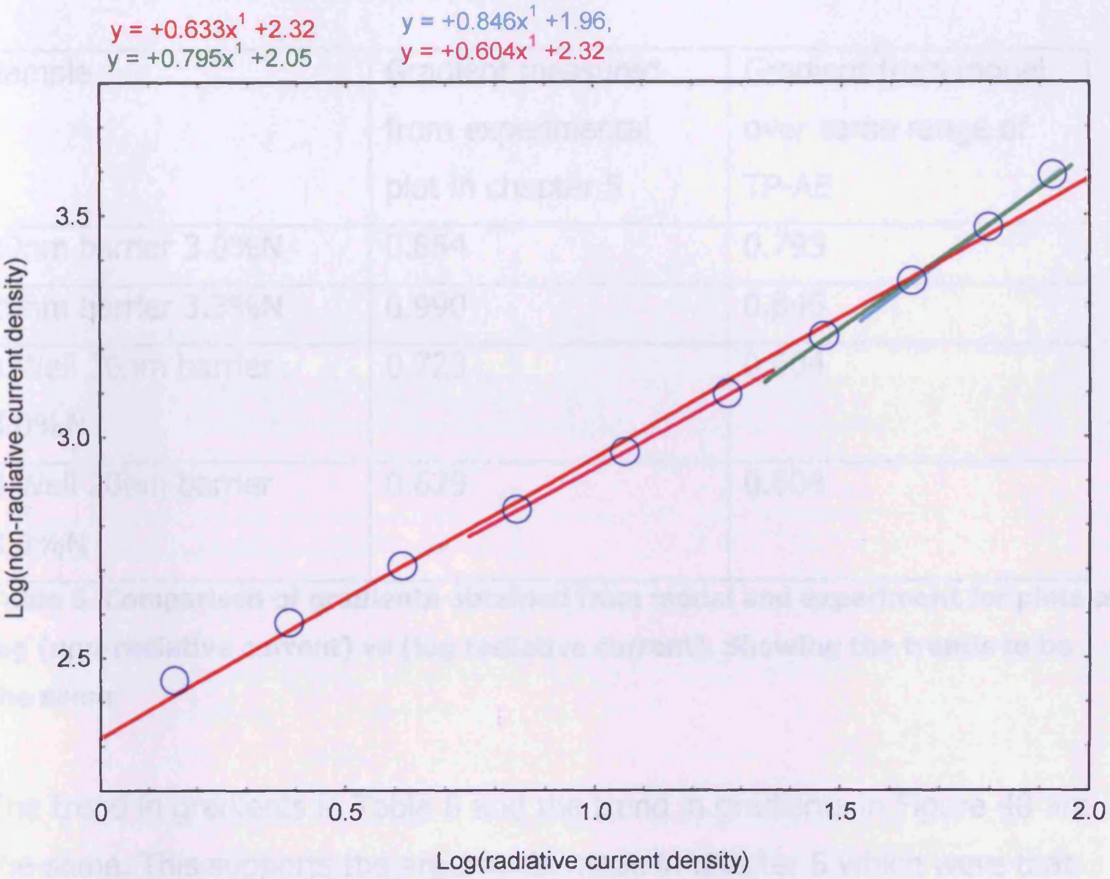

Figure 48. Theoretical plot of the model of log(non-radiative current density) vs log(radiative current density). Red line is fitted to all the data, the pink line is fitted to the region that the 3 well experimental data exists and the blue and green lines for the regions where the 1 well 20nm data exists. The gradients are shown above the graph.

The results for the experimental plots for the 20nm one well and the three well samples are repeated in Table 8

Sample	Gradient measured from experimental plot in chapter 5	Gradient from model over same range of TP-AE
20nm barrier 3.0%N	0.854	0.795
20nm barrier 3.3%N	0.990	0.846
3 Well 20nm barrier 3.0%N	0.723	0.604
3 Well 20nm barrier 3.3%N	0.629	0.604

Table 8. Comparison of gradients obtained from model and experiment for plots of log (non-radiative current) vs (log radiative current). Showing the trends to be the same.

The trend in gradients in Table 8 and the trend in gradients in Figure 48 are the same. This supports the arguments made in chapter 5 which were that the differences in gradients between the one and three well sample was due to at least in part the data being taken over different injection levels.

6.5 Simulation Results

In this section I will discuss how I took the results I used from the simulation. The first graph used shows the positions of the quasi-Fermi levels in the structure which was used to find the quasi-Fermi level separation and can be seen in Figure 49.

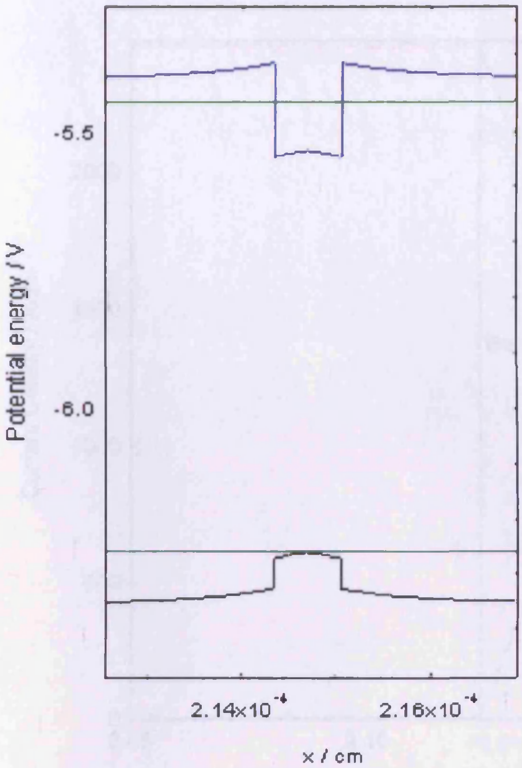

Figure 49. Band diagram showing the quasi-Fermi levels (green) in both the conduction (blue) and valence (black) band as a function of distance through the structure

Figure 50 shows where in the structure current flow occurs according to the model, I used this to compare the amount of current in the barrier and the well. Marked on Figure 50 are the GaNAs barrier regions and between these is the well.

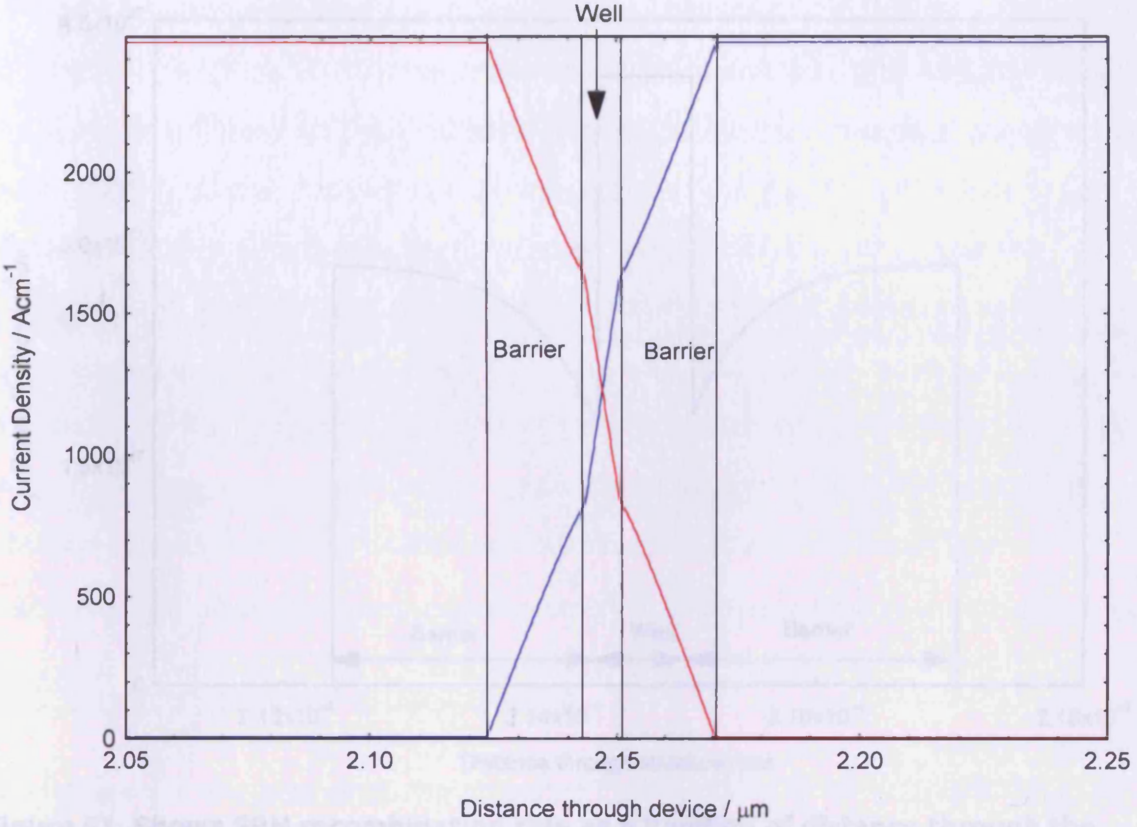

Figure 50. Graph showing current flow as a function of distance through the device, the red line represents holes, blue electrons. The total current remains constant, a change in the y-axis value indicates recombination is taking place.

The software also produces graphs of Shockley-Reed-Hall (SRH) recombination, Auger Recombination and Radiative Recombination as a function of distance through the described structure. These are then used to work out the current density associated with each process in both the well and barrier regions. A SRH recombination graph is shown in Figure 51 as an example, marked on this are the GaNAs barrier regions and the GaInNAsSb well.

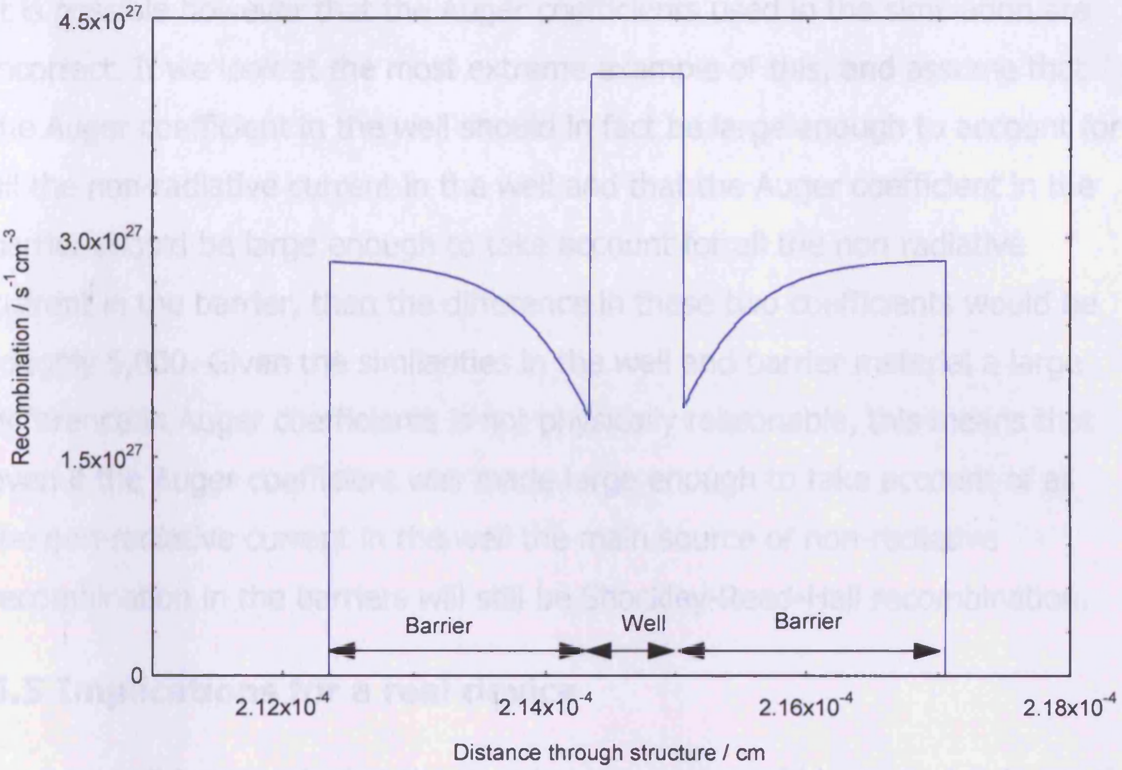

Figure 51. Shows SRH recombination rate as a function of distance through the structure (x) produced by the model.

I ran the model at a quasi-Fermi level separation that corresponds to a transparency point minus absorption edge of 0.025 eV, the results of this are shown in Table 9

	In a well	In a barrier
Auger recombination	106 Acm^{-2}	0.02Acm^{-2}
SRH recombination	336 Acm^{-2}	442Acm^{-2}
Radiative recombination	24.9Acm^{-2}	0.08Acm^{-2}

Table 9. Results of simulation done at a transparency point minus absorption edge of 0.025 eV.

Using the values from Table 9 the total Auger current in a single well device would be 106Acm^{-2} and the SRH would be 1220Acm^{-2}, suggesting that SRH is overall the main non-radiative process, the small simulated Auger current in the barrier arises from the low carrier density.

It is possible however that the Auger coefficients used in the simulation are incorrect. If we look at the most extreme example of this, and assume that the Auger coefficient in the well should in fact be large enough to account for all the non-radiative current in the well and that the Auger coefficient in the barrier should be large enough to take account for all the non radiative current in the barrier, then the difference in these two coefficients would be roughly 5,000. Given the similarities in the well and barrier material a large difference in Auger coefficients is not physically reasonable, this means that even if the Auger coefficient was made large enough to take account of all the non-radiative current in the well the main source of non-radiative recombination in the barriers will still be Shockley-Reed-Hall recombination.

6.5 Implications for a real device

In chapter 5 I showed what the threshold current would be in a real device if it were possible to remove all the non-radiative current. However Auger recombination is likely to be difficult to reduce, using the simulation results it is possible to work out what the non-radiative current density would be if all the Shockley-Reed-Hall recombination could be eliminated but the Auger remained. For the same 1 mm long laser with uncoated facets with an optical loss of 17 cm^{-1} (α_i = 5 cm^{-1}) as was used in chapter 5, the threshold current density is 320Acm^{-2} compared to the previous value of 35Acm^{-2}. This shows that there is room for improvement with this material just by reducing Shockley-Reed-Hall recombination.

6.6 Conclusion

In this chapter I have described a model that has made it possible to evaluate how big a contribution each of the non-radiative recombination processes make to the total non-radiative current both in a device as a whole and in the barriers and well(s) individually. I have shown, using the input parameters that are described in Table 7, that when the entire experimental range of values of TP-AE are simulated the model gives values for the total non-radiative current in good agreement with the experimental values. Using these parameters I have shown that the Auger contributes around a third of the non-radiative current in the well and roughly none in the barrier, with SRH accounting for the rest. There is uncertainty in the value of Auger co-efficient used. However if a "worst case" value is used where by it is adjusted to account for all the well recombination, the barrier recombination is still negligible unless the barrier Auger co-efficient is 5000 larger than the new "worst case" well scenario. So it is safe to say that Auger recombination in the barrier is negligible. The results in this chapter show that it should be possible to improve the performance of these devices significantly by reducing the level of SRH recombination, this could be achieved by optimising growth conditions and layer design paying particular attention to the barriers.

6.7 References

- Bank. S.R, Bae. H, Goddard. L.L, Yuen. H.B, Wistey. M.A, Kudrawiec. R, James S. Harris IEEE Journal of Quantum Electronics, 43, 9, (2007)
- Goddard. L.L, Bank. S.R, Wistey. M.A, Yuen. H.B, Rao. Z and Harries. J.S. Jr, J. Appl. Phys. 97, 083101 (2005)
- Liu. H.F and Ngai. W.F. IEEE J. Quantum Electron. 29, No.6, June 1993
- Sim Windows,http://www.ocs.colorado.edu/SimWindows/simwin.html
- Thomson. J.D, Pope. I.A, Smowton. P.M, Blood. P , Lynch. R.J, Hill. G, Wang. T and Parbrook. P, J. Appl. Phys. 99, 024507, (2006)
- Winston. D.W and Hayes. R.E, IEEE J. Quantum Electron. 34, 707 (1998)

7. Comparison with 1.3μm GaInNAs and InGaAs

7.1 Introduction

In the previous chapters I have detailed experiments that have allowed the main source of non-radiative recombination in 1.55μm GaInNAsSb lasers to be found. This has shown the potential for this material system subject to improvements in material quality. It is now important to see if GaInNAsSb has the same potential to ultimately be a useful gain material. In this chapter I will compare the fundamental gain characteristics of these lasers with low threshold InGaAs(N) lasers emitting at 1.2-1.3μm, thus showing whether GaInNAsSb has the potential to be a useful material system if the non-radiative recombination could be removed/reduced. The 1.2μm InGaAs(N) will also be compared to 1μm InGaAs. I will show the limitations with the widely used G_0 parameter from the equation $G=G_0 ln(J/J_{tr})$ when comparing different material systems. In addition I will show a new method of comparing materials using experimental data comparing the product of the fundamental properties of the matrix element, density of states and the overlap integral. These properties are not always easy or possible to calculate, particularly for new material systems and more complex material systems, so it is useful to be able to find the product of these properties experimentally as they can be used to work out which material will give the most gain for a given level of inversion. The ultimate saturated gain is also worked out.

7.2 Structure details

The GaInNAsSb structures that will be used in this chapter have been previously described at the start of chapter 5 the 3.3% one and three well samples will be used. The 1.2-1.3μm InGaAs(N) samples were grown at the University of Madison Wisconsin by MOVPE and details of growth are given in (Tansu et al, 2003). The measurements on these samples were taken by David Palmer in Cardiff University, details can be found in his PhD thesis. A schematic diagram of these InGaAsN structures can be found in Figure 52.

There are three of these structures, one with no Nitrogen in the well, one with 0.5% and one with 0.8%.

It is important to note that all the samples in this chapter have the same Indium and Gallium contents, being 40% and 60% respectively, unless stated otherwise.

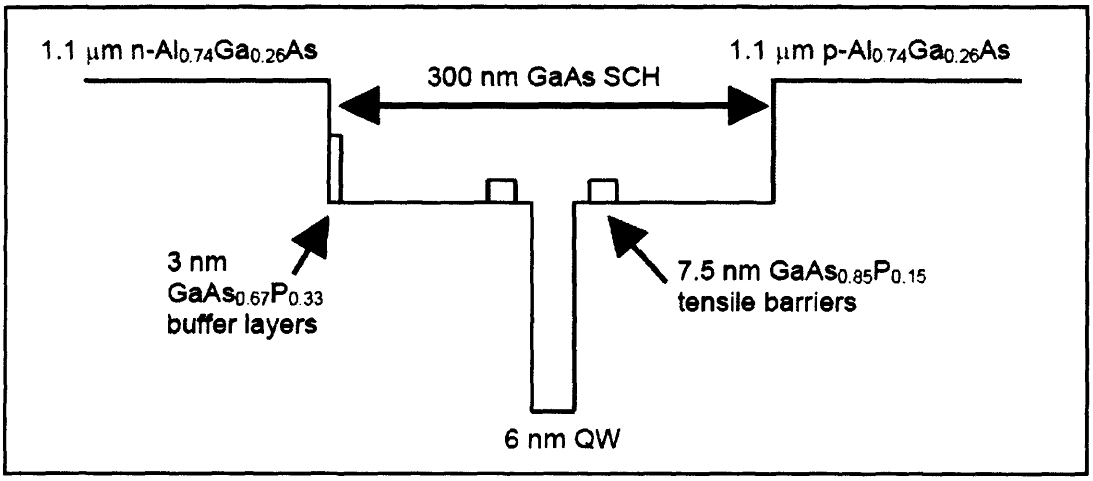

Figure 52. Schematic diagram of the 1.2-1.3μm InGaAs(N) structures.

Table 10 details the samples that are used in this chapter.

Material Type	Nitrogen Content	Wavelength
InGaAs(N)	0%	≈1.2μm
InGaAs(N)	0.5%	≈1.3μm
InGaAs(N)	0.8%	≈1.3μm
GaInNAsSb	3.3%	≈1.55μm

Table 10. Samples used in this chapter

7.3 Results

7.3.1 Measured Gain Plots

The first comparison I made is the modal gain as a function of radiative current obtained by integrating the spontaneous emission. To fairly compare gain characteristics it is important that there is only recombination from one sub-band. In the case of the 0.8% Nitrogen sample this was not the case, by inspection the spontaneous emission contributions from a second state were seen. At higher currents these become dominant, thus this sample wasn't used in the comparisons. A plot of spontaneous emission rate spectra for the 0.8% sample can be seen in Figure 53

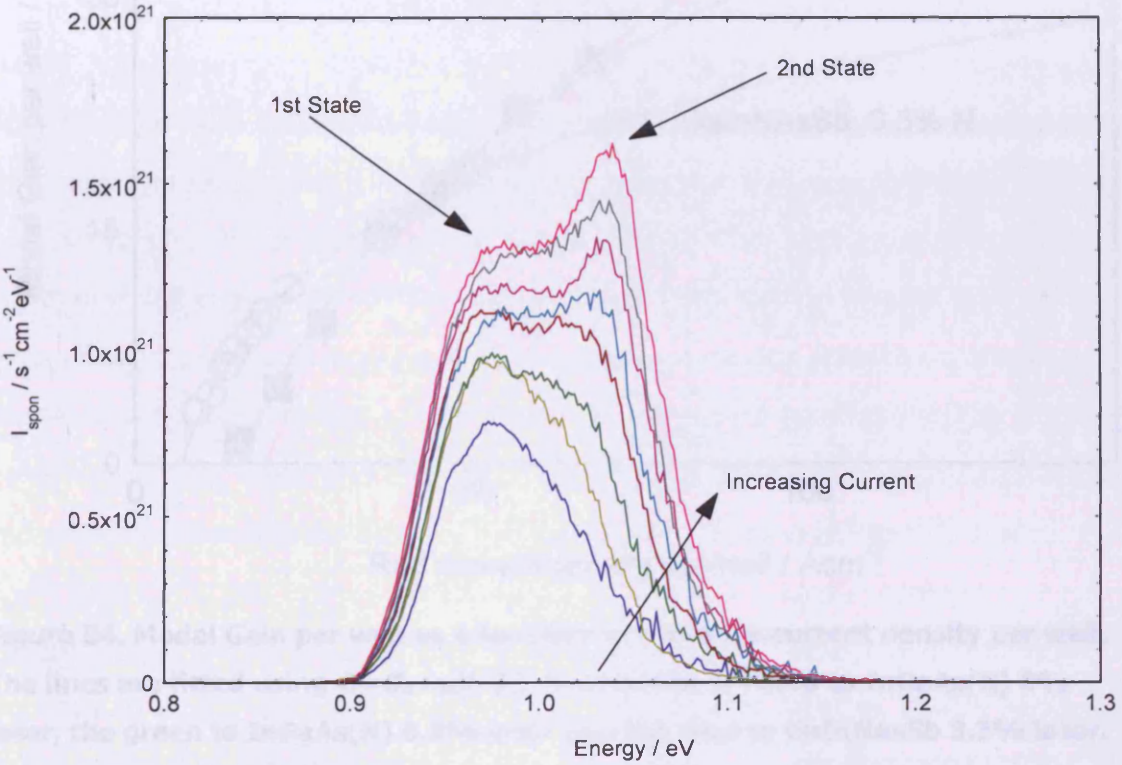

Figure 53. Spontaneous emission for the 0.8% InGaAs(N), showing the emergence of a second state.

All the other samples only showed recombination from one sub-band over the whole current range. Figure 54 shows the modal gain per well as a function of the radiative current per well. The data has been fitted by the equation $G=G_0 \ln(J/J_t)$, (Coldren and Corzine, 1995), where G_0 is the tangential modal gain parameter (the point at which the tangent to the gain curve will pass through the origin), J_t is the transparency current (the current at which the modal gain is equal to 0cm^{-1}). The one and three well GaInNAsSb 3.3%N have been treated as one data set for the purposes of the fitting, as was described in chapter 5.

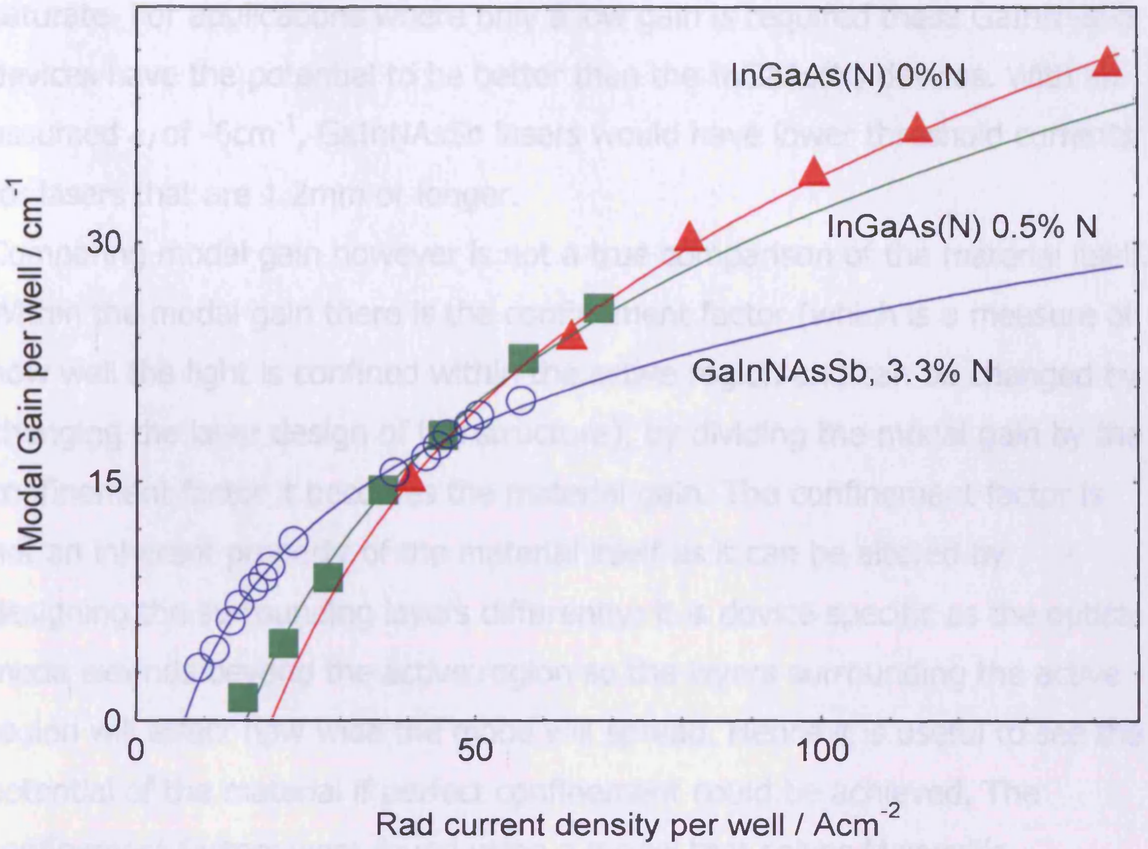

Figure 54. Modal Gain per well as a function of radiative current density per well. The lines are fitted using $G=G_0\ln(J/J_t)$. The red line is fitted to InGaAs(N) 0% laser, the green to InGaAs(N) 0.5% laser and the blue to GaInNAsSb 3.3% laser.

The values of G_0 and J_t for all the samples shown in Figure 54 are shown in Table 11 below.

Sample	G_0 / cm^{-1}	J_t / Acm^{-2}
InGaAs(N), 0%N	21.1	19.8
InGaAs(N), 0.5%	17.5	16.1
GaInNAsSb, 3.3%N	9.5	7.1

Table 11. Comparison of G_0 and J_t for all the samples

Figure 54 shows that the inclusion of more Nitrogen reduces the amount of modal gain compared to radiative current and also reduces the transparency current. This is the same trend as was shown in chapter 5 when comparing the 3.0%N samples to the 3.3%N (figure 39, 5.4.4). It also suggests that the modal gain saturation value is reduced, however the fit used will never saturate. For applications where only a low gain is required these GaInNAsSb devices have the potential to be better than the InGaAs(N) devices. With an assumed α_i of -6cm^{-1}, GaInNAsSb lasers would have lower threshold currents for lasers that are 1.2mm or longer.

Comparing modal gain however is not a true comparison of the material itself. Within the modal gain there is the confinement factor (which is a measure of how well the light is confined within the active region and can be changed by changing the layer design of the structure), by dividing the modal gain by the confinement factor it becomes the material gain. The confinement factor is not an inherent property of the material itself as it can be altered by designing the surrounding layers differently; it is device specific as the optical mode extends beyond the active region so the layers surrounding the active region will effect how wide the mode will spread. Hence it is useful to see the potential of the material if perfect confinement could be achieved. The confinement factors were found using a model that solves Maxwell's equations using only the real part of the refractive indices. Contained within the confinement factor is a dependence on well width (Blood, 2000), so to make a fair comparison it is necessary to work out the confinement factors for the same effective well width and then use these when comparing the material gain. The scaled material gain is shown in Figure 55.

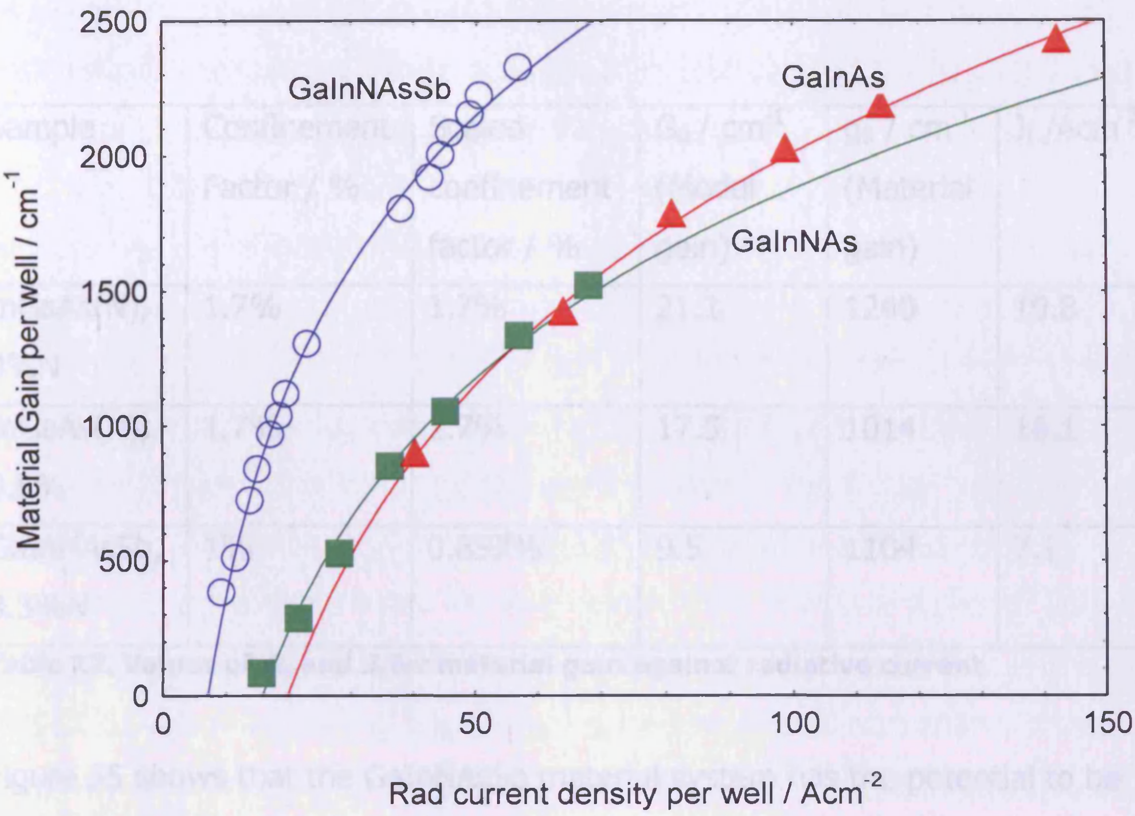

Figure 55. Material gain as a function of radiative current density per well scaled to the same well width (6nm).

The data in Figure 55 was fitted with the formula $g=g_0\ ln(J/J_t)$, the values of g_0 and J_t can be found in Table 12 along with the confinement factors, scaled confinement factors and the G_0 values from Table 11

Sample	Confinement Factor / %	Scaled confinement factor / %	G_0 / cm^{-1} (Modal gain)	g_0 / cm^{-1} (Material gain)	J_t /Acm^{-2}
InGaAs(N), 0%N	1.7%	1.7%	21.1	1240	19.8
InGaAs(N), 0.5%	1.7%	1.7%	17.5	1014	16.1
GaInNAsSb, 3.3%N	1%	0.857%	9.5	1104	7.1

Table 12. Values of G_0 and J_t for material gain against radiative current

Figure 55 shows that the GaInNAsSb material system has the potential to be better than InGaAs(N) for a wider range of values of gain than the modal gain plot showed. The fit used will never actually saturate, although it is a good fit for the data over a limited range of population inversion, so it is not possible to say which sample will have the highest saturated or maximum gain. This result also shows that simply by designing the GaInNAsSb structures to have better confinement would drastically improve laser performance, this however is not a trivial task as the longer wavelength of the GaInNAsSb devices means that the confinement is naturally lower when placed in a similar waveguide.
An interesting observation from looking at Table 12 and Figure 55 is that the values of g_0 taken in isolation would lead to the assumption that the GaInNAsSb material is not much better than the InGaAs(N) 0.5% material and is worse than the InGaAs(N) 0%. However the data shows that the GaInNAsSb is better than the InGaAs(N) over a large range of gain, so it is important not to just to compare g_0 values but to plot the curves out, this is because the values of G_0 and g_0 depend on J_t.
Using data taken from (Tsvid et al, 2008) it is possible to compare the InGaAs(N) 0%N results described in this chapter to a less strained InGaAs(N) 0%N device that emits at 0.98µm as apposed to 1.2µm. In doing this the

weakness in using only g_0 values to compare structures will be further highlighted. The 0.98µm device only has 20% Indium. Tsvid et al(2008) gives values for g_0 for both the structures for material gain: 1750cm^{-1} for the 1.2µm laser and 1229cm^{-1} for the 0.98µm laser. However this has not taken into account the effect that difference in well size has on the confinement factor as mentioned previously, the well in the 0.98µm laser is 8.5nm compared to 6nm in the 1.2µm laser. When the material gain for the 1.2µm laser has been calculated using a confinement factor for a well width of 8.5nm the g_0 value becomes 1235cm^{-1}, showing that the performance of the 1.2µm laser is on a par with the 0.98µm laser, it follows that the performance of the other structures used in this chapter are also comparable. However as noted above, comparing just the g_0 values can be misleading. Using the values of g_0 and J_t provided a graph of each of the original curves is plotted, also shown is the 1.2µm curve with the scaled confinement factor. These can be seen in Figure 56

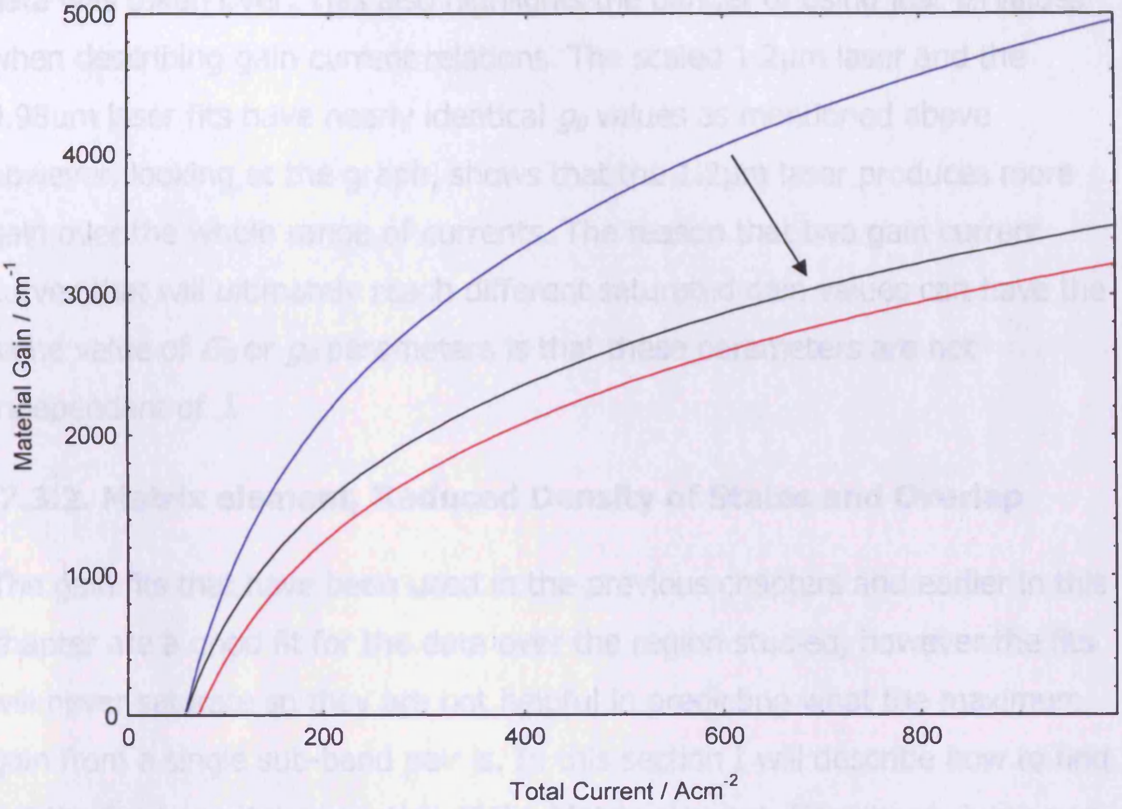

Figure 56. Gain current graphs for InGaAs devices produced using g_0 and J_{tr} values taken from literature and equation $g=g_0*ln(J/J_{tr})$. The blue is the 1.2μm device, the red is the less strained 0.98μm device and the black is the 1.2μm device with the scaled confinement factor (as shown in Table 13).

The g_0 values and confinement factors used to produce Figure 56 are shown in

Parameter	0.98μm InGaAs	1.2μm InGaAs
Confinement Factor / %	1.18	1.7
g_0 / cm^{-1}	1229	1750
Scaled Confinement Factor / %	1.18	2.41
Scaled g_0 / cm^{-1}	1229	1235

Table 13. Shows the values of g_0 and confinement factor used in Figure 56

Figure 56 shows that in actuality the scaled 1.2μm device (Black line) gives more gain over the whole current range than the 0.98μm laser (Red line). The range of currents shown in Figure 56 is the same range that the experimental data was taken over. This also highlights the danger of using just g_0 values when describing gain current relations. The scaled 1.2µm laser and the 0.98µm laser fits have nearly identical g_0 values as mentioned above however, looking at the graph, shows that the 1.2µm laser produces more gain over the whole range of currents. The reason that two gain current curves that will ultimately reach different saturated gain values can have the same value of G_0 or g_0 parameters is that these parameters are not independent of J.

7.3.2. Matrix element, Reduced Density of States and Overlap

The gain fits that have been used in the previous chapters and earlier in this chapter are a good fit for the data over the region studied, however the fits will never saturate so they are not helpful in predicting what the maximum gain from a single sub-band pair is. In this section I will describe how to find out the fundamental properties of the Matrix element, Density of states and the Overlap integral. These properties are not always easy or possible to calculate, particularly for new material systems and more complex material systems, so it is useful to be able to find the product of these properties experimentally as they can be used to work out which material will give the most gain for a given level of inversion. I will then describe a method for predicting the maximum gain which does not rely on fitting data. It can also be used to reduce and possibly remove the effect of the material having different band gaps.

7.3.2.1 Factors that describe the gain vs current relationship

This method requires the factors that affect the gain current relationship to be described. To do this the equation for spontaneous recombination, Equation 44 (Blood et al, 2003), is needed. The derivation of this equation was also dealt with in chapter 2.

$$I^{P}{}_{spon}(h\upsilon) = \left(\frac{1}{3}\right)\frac{16\pi n}{c^{3}h^{2}\varepsilon_{0}}(h\upsilon)\left(\frac{e}{2m_{0}}\right)^{2}\left|M^{p}\right|^{2} \times \left\{\int F^{\bullet}{}_{v}(z)F_{c}(z)dz\right\}^{2}\rho_{red}(h\upsilon)\{f_{1}(1-f_{2})\}$$

Equation 44

Equation 44 is the spontaneous recombination rate per unit energy interval per unit area in the polarisation *p*. F_c and F_v are the envelope functions of the confined states in the conduction and valence sub-bands, ρ_{red} is the reduced density of states per unit area and M^p is the momentum matrix element for transitions of polarisation *p*, *(hv)* is the photon energy, f_1 and f_2 are the occupation probabilities of an electron in the conduction and valence band respectively.

The other equation needed is the equation for modal gain, Equation 45 (Blood, 2000). Again the derivation of this equation was also dealt with in chapter 2.

$$G(hv) = \left[\frac{4\pi\hbar}{nc\varepsilon_{0}(h\nu)}\left(\frac{e}{2m_{0}}\right)^{2}\left|M^{p}\right|^{2}\left\{\int F_{v}^{\bullet}(z)F_{c}(z)dz\right\}^{2}\frac{\rho_{red}(h\upsilon)}{L_{z}}(f_{1}-f_{2})\right]\left[\frac{A_{Well}{}^{2}L_{z}}{\int A^{2}(z)dz}\right]$$

Equation 45

The first square bracket in Equation 45 is the material gain (*g*), the second square bracket is the optical confinement factor. Because the gain collected is always from one polarisation and is the same polarisation as the spontaneous emission the matrix elements are the same in Equation 44 and Equation 45. L_z is the width of the well.

7.3.2.1 Method

Normally the inversion of the system and hence the values of f_1 and f_2 are unknown, however at the transparency point we know that the system is half inverted which makes both f_1 and f_2 a half (for a pair of states corresponding to the transparency energy). The transparency point can be found from the gain curve and is the point at which the gain is equal to the internal loss as discussed in previous chapters, an example is shown in Figure 57 as a reminder.

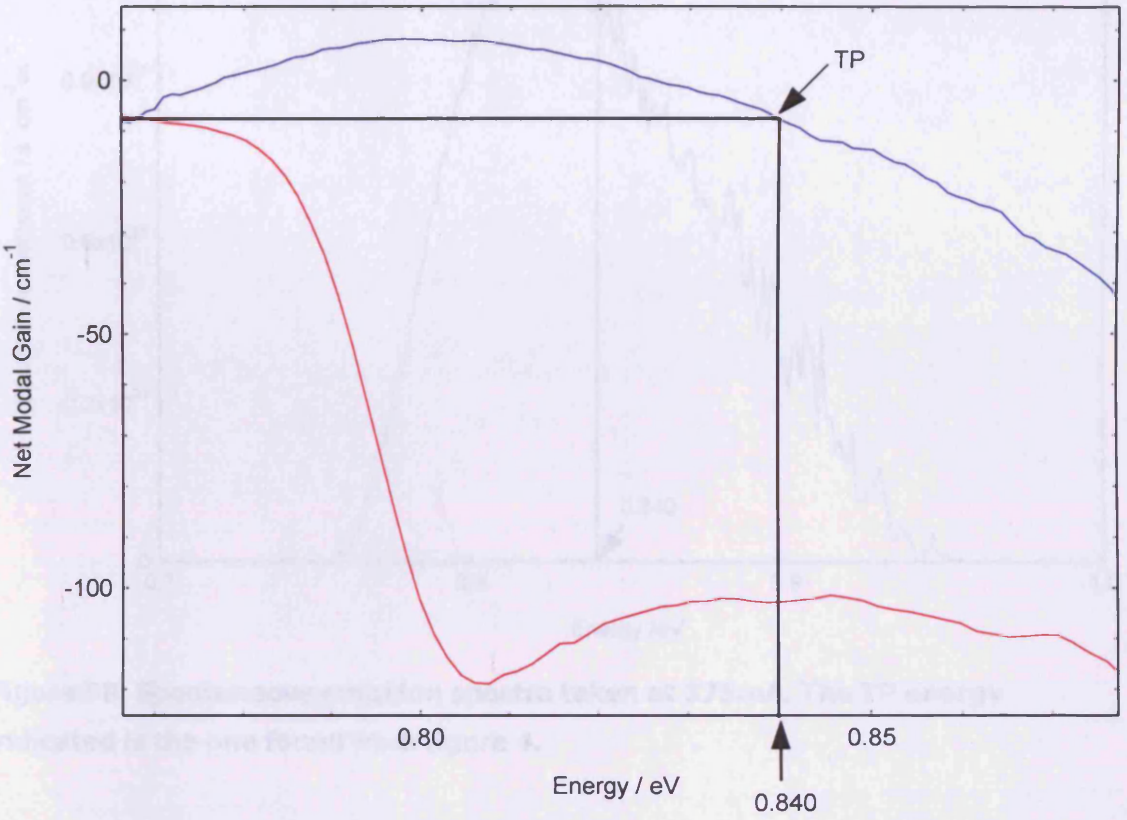

Figure 57. Net modal gain (Blue) and loss spectra (Red), TP indicates the transparency point and this gives the transparency energy. Gain is taken at 375mA

Having found the transparency energy it is then possible to find the value of the spontaneous emission at the transparency energy using the spontaneous emission plots produced using the multi-section technique, again as described in previous chapters. An example corresponding to the same sample and current as shown in Figure 57 with the transparency energy found from Figure 57 marked on is shown in Figure 58.

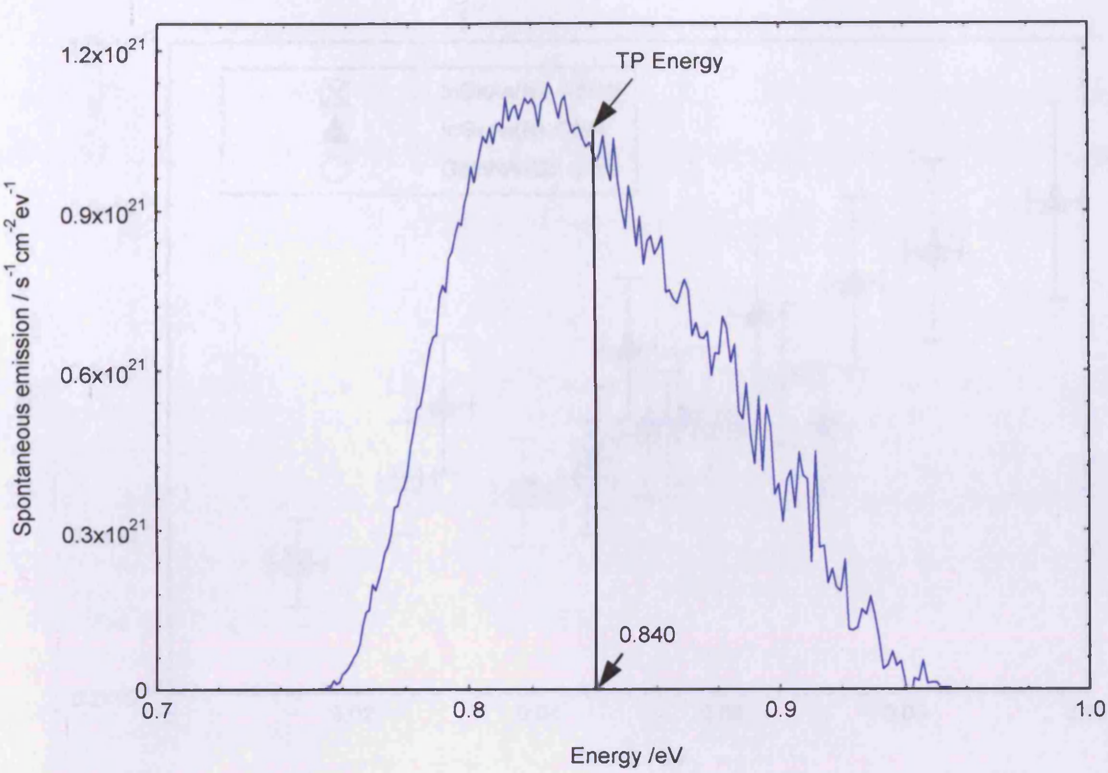

Figure 58. Spontaneous emission spectra taken at 375mA. The TP energy indicated is the one found from figure 4.

Substituting this value of spontaneous emission for I_{spon} and putting the transparency energy (0.84eV) in for the *(hv)* term, the only unknowns in Equation 44 are

$$\left|M^p\right|^2 \times \left\{\int F^{*}{}_{v}(z)F_c(z)dz\right\}^2 \rho_{red}(0.84)$$

a graph of this as a function of transparency point minus absorption edge for the InGaAs(N) 0%, 0.5% and the GaInNAsSb 3.3% is shown in Figure 59.

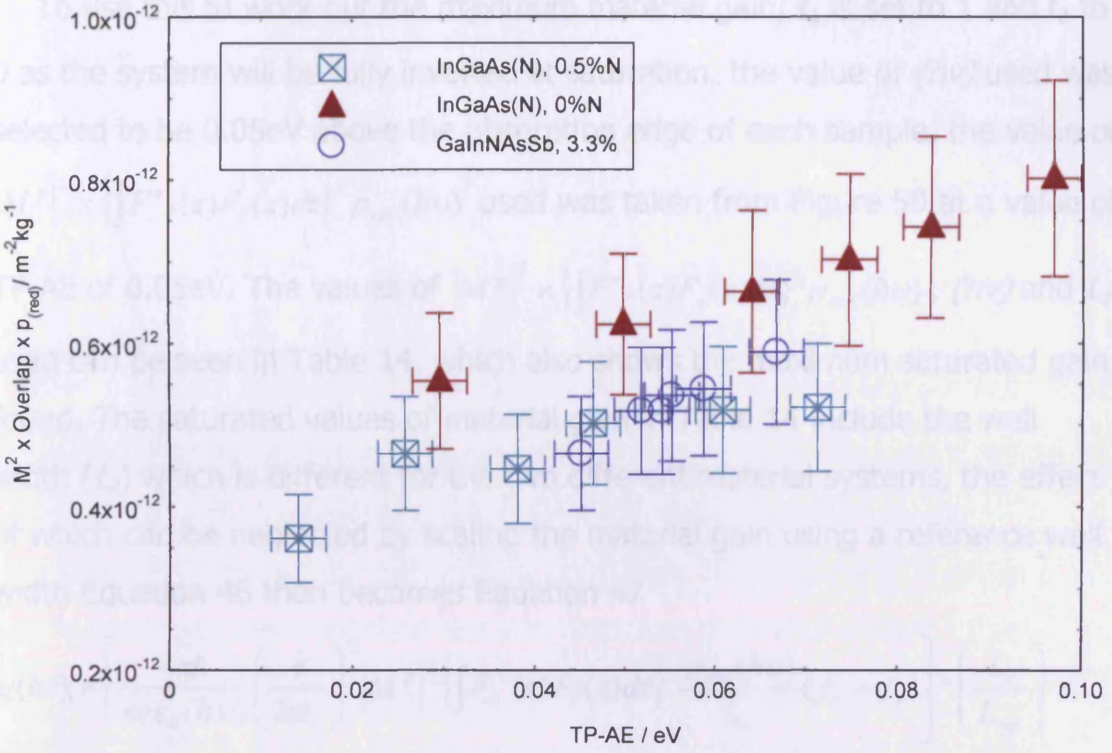

Figure 59. The matrix element squared multiplied by overlap multiplied by the reduced density of states, as a function of transparency point minus absorption edge

Figure 59 was produced by repeating the procedure shown in Figure 57 and Figure 58 for the full range of currents for each of the 3 samples.

If we assume that the density of states is flat and that the overlap integral does not change with photon energy, then Figure 59 implies that the Matrix element is increasing with increased carrier density (a larger TP-AE corresponds to a larger carrier density); this could be due to Coulomb enhancement. For these materials the density of states would be expected to not be flat with increasing photon energy.

Maximum material gain can be worked out using Equation 46 which is the first square bracket term of Equation 45.

$$g(h\nu) = \left[\frac{4\pi\hbar}{nc\varepsilon_0 (h\nu)} \left(\frac{e}{2m_0} \right)^2 \left| M^p \right|^2 \left\{ \int F_v^{\bullet}(z) F_c(z) dz \right\}^2 \frac{\rho_{red}(h\upsilon)}{L_z} (f_c - f_v) \right]$$

Equation 46

To use this to work out the maximum material gain; f_1 is set to 1 and f_2 to 0 as the system will be fully inverted at saturation, the value of *(hv)* used was selected to be 0.05eV above the absorption edge of each sample, the value of $|M^p|^2 \times \{\int F^{\bullet}{}_v(z)F_c(z)dz\}^2 \rho_{red}(h\upsilon)$ used was taken from Figure 59 at a value of TP-AE of 0.05eV. The values of $|M^p|^2 \times \{\int F^{\bullet}{}_v(z)F_c(z)dz\}^2 \rho_{red}(h\upsilon)$, *(hv)* and L_z used can be seen in Table 14, which also shows the maximum saturated gain found. The saturated values of material gain in Table 14 include the well width (L_z) which is different for the two different material systems, the effect of which can be neglected by scaling the material gain using a reference well width Equation 46 then becomes Equation 47

$$g(h\nu) = \left[\frac{4\pi\hbar}{nc\varepsilon_0(h\nu)}\left(\frac{e}{2m_0}\right)^2 |M^p|^2 \left\{\int F_v^{\bullet}(z)F_c(z)dz\right\}^2 \frac{\rho_{red}(h\upsilon)}{L_z}(f_c - f_v)\right] * \left(\frac{L_z}{L_{ref}}\right)$$

Equation 47

The value of L_{ref} was set to be 6nm, so the saturated material gain value will only change for the GaInNAsSb 3.3% sample. This value of saturated gain for the 3.3% sample with an effective well width of 6nm is also shown in Table 14.

Sample	$\lvert M^p\rvert^2 \times \{\int F^{\bullet}{}_v(z)F_c(z)dz\}^2 \rho_{red}(h\upsilon)$ At 0.05eV, $m^{-2}kg^{-1}$	Saturated Material Gain / cm^{-1}	Well Width /nm	Photon Energy/ eV
InGaAs(N), 0%	6.23×10^{-13}	7595	6	1.04
InGaAs(N), 0.5%	5.02×10^{-13}	6447	6	0.96
GaInNAsSb, 3.3%	5.17×10^{-13}	6345	7	0.84
GaInNAsSb, 3.3%	5.17×10^{-13}	7402	6	0.84

Table 14. Showing the worked out quantities for the different samples.

The saturated gain values that are shown in Table 14 are roughly independent of the band gap of the material. This is because the matrix element can be described by Equation 48 (Coldren and Corzine, 1995)

$$|M|^2 = \left(\frac{m_0}{m^*} - 1\right)\frac{(E_g + \Delta)}{2\left(E_g + \frac{2}{3}\Delta\right)} m_0 E_g$$

Equation 48

If we assume that *Δ* is small in comparison to the energy gap of the material (E_g) then the $(E_g + \Delta)$ and the $(E_g + 2/3\Delta)$ terms will cancel leaving a dependence of the matrix element on band gap. In Equation 47 there is a *(hv)* term which when working out the saturated gain was chosen to be a fixed value above the band edge, (the band edge is a measure of the lowest energy transition in the quantum well). As long as the value of the band edge used is only a small amount of energy above the material band gap then the difference between the band edge and the band gap is negligible. This then means that in Equation 47 the energy gap in the matrix element and the energy gap in the *(hv)* will cancel with each other leaving the gain (*g*) independent of the energy gap. Equation 48 is presented here only as part of the argument that the worked out saturated gain is roughly independent of band gap size, it is not used to work out a value of matrix element, the entire term $\{|M^p|^2 \times \{\int F^*{}_v(z) F_c(z) dz\}^2 \rho_{red}(h\upsilon)\}$ is found experimentally.

7.4 Conclusions

In this chapter I have shown that the GaInNAsSb devices have the potential to produce as much gain for a given radiative current as 1.2-1.3μm InGaAs(N) devices over a wide range of values for gain, provided that the confinement can be increased sufficiently. I have shown that the introduction of nitrogen (N) (from 0% to 0.5%) leads to a lower saturated gain. However with the introduction of antimony (Sb), it is possible to increase the nitrogen content without the saturated gain suffering to such a great extent (this is because the antimony has increased the value of $\left|M^{p}\right|^{2} \times \left\{\int F^{\bullet}{}_{v}(z)F_{c}(z)dz\right\}^{2} \rho_{red}(h\upsilon)$). The inclusion of the 0.5% of nitrogen in the InGaAs(N) sample will have increased the reduced density of states as the electron mass increases with increased nitrogen as does the heavy hole mass, so the fact that it has a lower value of $\left|M^{p}\right|^{2} \times \left\{\int F^{\bullet}{}_{v}(z)F_{c}(z)dz\right\}^{2} \rho_{red}(h\upsilon)$ implies that nitrogen is reducing the matrix element and or the overlap integral. The inclusion of even more nitrogen therefore would be assumed to lower this quantity further. However the GaInNAsSb sample, which contains considerably more nitrogen, actually has a higher value. This therefore indicates that the antimony increases either the matrix element and/or the overlap, (the antimony will slightly lower the reduced density of states as it reduces the in plane heavy hole mass). Increasing the nitrogen content has the effect of reducing the band gap which in turn will reduce the matrix element. However when working out the saturated gain the effect of a different band gap is removed because the band gap is contained within the *(hv)* term, as the values were worked out at a value of photon energy that is 0.05eV above the effective band edge. This then is a way of comparing samples that is independent of the band gap and shows that the addition of nitrogen from 0% to 0.5%N has reduced this saturated gain value. However on going from 0% to 3.3%N and adding some Sb this quantity has not been reduced.

7.5 References

- Blood. P. JQE, vol. 36, NO. 3, March 2000
- Blood. P, Lewis. G.M, Smowton. P.M, Summers. H, Thomson. J and Lutti. J. JSQE, Vol. 9, No. 5, 2003
- Coldren. L.A and Corzine. S.W, Diode Lasers and Photonics Integrated Circuits, Wiley Series in Microwave and Optical engineering, Vol 1, Kai Chang, 1995
- Tansu. N, Yeh. J.Y, Mawst. L.J, Appl Phys Letts, 82 (2003) 4038
- Tsvid. G, Kirch. J, Mawst. L.J, Kanskar. J, Ca. Ji, Arif. R.A, Tansu. N, Smowton. P.M, and Blood. P. JQE, Vol. 44, No. 8, 2008

8. Summary of Achievements and Future Work

This work undertaken in this thesis can be split into three sections covering four chapters. In the first section (Chapter 4) the effect of different levels of modulation doping was investigated. In the second section the location of non-radiative current are both located in the device and then the balance of contribution of the possible different non-radiative processes is found (Chapters 5 and 6). The final section investigates the effect of increased nitrogen content and the inclusion of antimony on gain current characteristics. I propose a new method to compare the sum of the matrix element, density of states and overlap integral and then find the effects of increasing nitrogen and introducing antimony on this. A method of working out the saturated gain from one sub-band is also described. (Chapter 6 primarily but also Chapter 5). The achievements and conclusions from each section are given below.

8.1 Effect of Doping on GaInNAsSb Active Regions

- The inclusion of n-type modulation doping does not have a net affect on the gain current relationship, nor does it alter the amount of non-radiative current present.
- The inclusion of p-type modulation doping again does not have a net affect on the gain current relationship however it does increase the non-radiative current present. This increase is attributed to the introduction of extra defects by the p-type doping process to both the well and barrier
- The rate of increase in non-radiative recombination for the differently doped samples is the same with increasing carrier density, this implies that Auger is not the main source of non-radiative recombination
- Plotting log(non-radiative recombination) against log(radiative recombination) for the differently doped samples has indicated that there is non-radiative recombination in the barrier

8.2 Location and Source of Non-Radiative Current in the GaInNAsSb/GaNAs material system

- The amount of non-radiative current that occurs in one GaNAs barrier is the same as occurs in one GaInNAsSb well, highlighting the importance of careful barrier design
- Barrier recombination remains significant even at 200K
- The non-radiative current in the GaNAs barrier is down to Shockley-Reed-Hall (defect) recombination, which shows that an increase in material quality (therefore reducing defects) of the GaNAs barriers could lead to significant reductions in the total non-radiative current
- Reducing the size of the GaNAs barriers is shown to reduce the material quality and so is shown to not be a viable method of reducing total barrier emission. This reduction in material quality is shown to be due to increased defects in the well (by inspection of the log(non-radiative current) vs log(radiative current) plot. This is because the strain in the well is not sufficiently compensated by the barriers.
- The increase in defects in the well, due to thinner barriers, results in the Shockley-Reed-Hall lifetime in the well being a factor of 4 faster

8.3 Comparison of Gain-Current characteristics etc

- Increasing nitrogen content from 3.0% to 3.3%, whilst keeping the antimony constant, reduces the amount of gain achieved for a constant value of radiative current. It also reduces the transparency current.
- Increasing nitrogen content from 0% to 0.5%, with no antimony present, also reduces the amount of gain achieved for a constant value of radiative current and it reduces the transparency current.
- The weakness in using solely the G_0 parameter from the $G=G_0 ln(J/J_{tr})$ formula to compare materials is shown. This is due to the gain dependence on J_{tr}, which itself is strongly affected by the bandgap of the material.

- A method of experimentally determining the sum of; the matrix element, density of states and overlap integral as a function of carrier density is shown.
- A method for working out the saturation value of gain from one state experimentally is shown. This value is roughly independent of bandgap.
- Increasing the nitrogen content from 0% to 0.5% is shown to decrease both the sum of the matrix element, density of states and overlap integral and the saturated gain value.
- Increasing the nitrogen content from 0.5% to 3.3% and introducing antimony is shown to have roughly no net affect on the matrix element, density of states and overlap integral but increases the saturated gain.
- Increasing the nitrogen from 0% to 3.3% and including antimony is shown to reduce the matrix element, density of states and overlap integral but to have no net affect on the saturated gain
- The ultimate performance which is measured here by gain radiative current plots show that the current 1.55µm GaInNAsSb/GaNAs devices have the potential to be better than high performance 1.3µm InGaAs(N) over a wide range of gain values (from looking at modal gain) and that the GaInNAsSb/GaNAs material itself has the potential to be better over an even larger range of gain values (looking at material gain).
- All the above shows that GaInNAsSb/GaNAs is a material that warrants further investigation and improvements being made, and that GaInNAsSb as an active region shows great promise

8.4 Overall conclusion

The work presented in this thesis has shown that the ultimate performance of GaInNAsSb as an active region emitting at 1.55µm is comparable if not better than 1.2-1.3µm InGaAsN. Therefore more work should be done on improving this material if it is to reach it's full potential to produce low threshold lasers and that could be used in optical fibre communications. The location and sources of non-radiative current have also been established and have shown that the current GaInNAsSb/GaNAs system has the potential to have far lower total non-radiative current if barrier material quality can be improved, because a large amount of non-radiative recombination is shown to be happening in the barriers.

8.5 Future Work

Recent work has demonstrated relatively low threshold VCSELs on this material system (Sarmiento, 2009). So improving this material will yield even better devices that will be commercially viable. This thesis points towards two avenues of investigation and improvement for GaInNAsSb devices emitting at 1.55μm. Firstly the optimisation of growth conditions of GaNAs barriers leading to improved material quality will yield devices with lower threshold currents by reducing total non-radiative recombination. The other direction to go in and the one that I would be most interested in seeing the results of is to change the GaNAs barriers to GaAsP barriers. GaAsP has a larger bandgap than GaNAs which will greatly reduce the number of carriers in the barrier for a given quasi-Fermi level separation. It will also still provide strain compensation so will not lead to a reduction in material quality. The difficulties in using GaAsP are; firstly that the flow of a new element will need to be controlled during growth and P contamination of the quantum well, however these problems are likely to be problems that can be ironed out.

8.4 References

- (Sarmiento, 2009), Electronics Letters, Vol. 45, No. 19, 2009

9. Appendix

9.1 Conferences

- Ferguson. J.W, Smowton. P.M, Blood. P, Gupta. J.A, Aers. G.C, "Recombination in GaInNAsSb Quantum Well Lasers". SIOE 31st March-2nd April, 2008, Cardiff, UK
- Ferguson. J.W, Smowton. P.M, Blood. P, Gupta. J.A, Aers. G.C, "Recombination in GaInNAsSb Quantum Well Lasers" CLEO 2008 May 04-09th, San Jose, USA
- Ferguson. J.W, Smowton. P.M, Blood. P, Gupta. J.A, Aers. G.C, "Carrier Leakage in GaInNAsSb Quantum Well Lasers", COST288 meeting, 18-23rd May, Calabria, Italy.
- Ferguson. J.W, Smowton. P.M, George. A.A, Sandall. I.C, Gupta. J.A, Aers G.C, Wang. S.M, Larsson. A, "Experimental Analysis of GaAs Based 1.3-1.6μm Laser Materials", QEP Photon 08, 26-29th August, Edinburgh, UK
- Ferguson. J.W, Smowton. P.M, Blood. P, Bae. H, Sarmiento. T, Harris. J.S, " Origin of Non-Radiative Recombination in GaInNAsSb/GaNAs Quantum Well Lasers" SIOE 2009, April, Cardiff, UK
- Ferguson. J.W, Smowton. P.M, Blood. P, Bae. H, Sarmiento. T, Harris. J.S, "Origin of Non Radiative recombination in GaInNAsSb/GaNAs Quantum Well Lasers", CLEO 2009, May 4-9th, Baltimore, USA
- Ferguson. J.W, Smowton. P.M, Blood. P, Bae. H, Sarmiento. T, Harris. J.S, "Origin of Non Radiative recombination in GaInNAsSb/GaNAs Quantum Well Lasers", COST MP0805 meeting, 23rd May, 2009, Essex, UK

9.2 Publications

- Ferguson. J.W, Smowton. P.M, Blood. P, Bae. H, Sarmiento. T, Harris. J.S, "Nonradiative recombination in 1.56 μm GaInNAsSb/GaNAs quantum-well lasers", Applied Physics Letters, 95, 231104 (2009); doi:10.1063/1.3271182